University of Windsor
Scholarship at UWindsor

Electronic Theses and Dissertations | Theses, Dissertations, and Major Papers

2015

Investigation on DI CNG Technologies and Related Development for the Mixture Formation

Biagio Logaldo
University of Windsor

Follow this and additional works at: https://scholar.uwindsor.ca/etd

Part of the Engineering Commons

Recommended Citation

Logaldo, Biagio, "Investigation on DI CNG Technologies and Related Development for the Mixture Formation" (2015). *Electronic Theses and Dissertations*. 5699.
https://scholar.uwindsor.ca/etd/5699

This online database contains the full-text of PhD dissertations and Masters' theses of University of Windsor students from 1954 forward. These documents are made available for personal study and research purposes only, in accordance with the Canadian Copyright Act and the Creative Commons license—CC BY-NC-ND (Attribution, Non-Commercial, No Derivative Works). Under this license, works must always be attributed to the copyright holder (original author), cannot be used for any commercial purposes, and may not be altered. Any other use would require the permission of the copyright holder. Students may inquire about withdrawing their dissertation and/or thesis from this database. For additional inquiries, please contact the repository administrator via email (scholarship@uwindsor.ca) or by telephone at 519-253-3000ext. 3208.

Investigation on DI CNG Technologies and Related Development for the Mixture Formation

By

Biagio Logaldo

A Thesis
Submitted to the Faculty of Graduate Studies
through the Department of Mechanical, Automotive & Materials Engineering
in Partial Fulfillment of the Requirements for
the Degree of Master of Applied Science
at the University of Windsor

Windsor, Ontario, Canada

2015

© 2015 Biagio Logaldo

Investigation on DI CNG Technologies and Related Development for the Mixture Formation

By

Biagio Logaldo

APPROVED BY:

_____

R. Barron
Department of Mathematics and Statistics

_____

G. Rankin
Department of Mechanical, Automotive & Materials Engineering

_____

A. Sobiesiak, Advisor
Department of Mechanical, Automotive & Materials Engineering

July 30, 2015

DECLARATION OF ORIGINALITY

I hereby certify that I am the sole author of this thesis and that no part of this thesis has been published or submitted for publication.

I certify that, to the best of my knowledge, my thesis does not infringe upon anyone's copyright nor violate any proprietary rights and that any ideas, techniques, quotations, or any other material from the work of other people included in my thesis, published or otherwise, are fully acknowledged in accordance with the standard referencing practices. Furthermore, to the extent that I have included copyrighted material that surpasses the bounds of fair dealing within the meaning of the Canada Copyright Act, I certify that I have obtained a written permission from the copyright owner(s) to include such material(s) in my thesis and have included copies of such copyright clearances to my appendix.

I declare that this is a true copy of my thesis, including any final revisions, as approved by my thesis committee and the Graduate Studies office, and that this thesis has not been submitted for a higher degree to any other University or Institution.

ABSTRACT

The increasingly stringent requirement to reduce fuel consumption and emissions is pushing carmakers to investigate new and more challenging alternatives. In this rushing scenario, the Direct Injection of Compressed Natural Gas has emerged as a high potential strategy to improve SI engine performance.

Since the direct injection of natural gas is an emerging technology, the research of the optimal setup, looking at the injection parameters and at the design of the combustion chamber, is still a relevant issue.

This thesis has the goal of realizing and validating a model of a DI CNG injector. After this first step, the mentioned model is used to evaluate the effect that some of the most important parameters have on the mixture formation.

DEDICATION

To my father,

Who always supported me, even when he thought I was making the craziest choice.

To my mother,

Who always encouraged me, even if sometimes she was more worried than I was about my exams.

ACKNOWLEDGEMENTS

Finally, this is the conclusion of a long year. Even though living in Canada now seems the most natural thing in the world, when I arrived in Windsor last August it was my first time on a new continent. I am really satisfied about this experience for all the new things I learned here.

This experience has been so special thanks to the people and the institutions who worked to make it possible. For this reason, I would like to thank all of them.

Great thanks are for Politecnico di Torino, Fiat and the coordinators of this program in Italy, Doctor Giovanni Belingardi and Edoardo Rabino, who organized it.

I would like also to thank the North American counterpart, which is represented by the University of Windsor, the Automotive Research and Development Centre and FCA US LLC. In particular, within these institutions, I would like to express my gratitude to Doctor Andrzej Sobiesiak, Mohammed Malik, Asim Iqbal and Ishika Towfic for their valuable technical support.

A special mention is for Jonnalagedda Srikanth. He is the person who helped me in the development of my model. All the things I learned about Converge and Ensight are thanks to him.

I also express my gratitude to my advisors in Politecnico di Torino: Mirko Baratta and Ezio Spessa. They have always been ready to give me precious suggestions to overcome any difficulty.

I further want to thank the Centro Ricerche Fiat and the people who helped me from there: Andrea Domenico Gerini, Massimo Ferrera and Francesco Perna. They always provided me with all the information I needed with a noteworthy efficiency.

The greatest thanks are for my parents, my brother and my sister who always encouraged and supported me during this long year even if they were on the other side of the world.

I am really grateful to my girlfriend Ilaria for her patience over this long year. I know it has been very difficult for her.

Finally, I want to thank all my friends. The Canadian ones, Luka and Stefan, for all the time we spent together at ARDC, and the Italian ones, Sergio, Ivan, Fabio and Francesco who shared with me this special experience and because they always prepared for me good food without onion.

TABLE OF CONTENTS

DECLARATION OF ORIGINALITY iii

ABSTRACT iv

DEDICATION v

ACKNOWLEDGEMENTS vi

LIST OF TABLES xi

LIST OF FIGURES xii

LIST OF ABBREVIATIONS/SYMBOLS xvii

NOMENCLATURE xix

1. INTRODUCTION 1

1.1. Objectives 3

1.2. Thesis organization 4

2. LITERATURE REVIEW 6

2.1. CNG and Argon properties 6

2.2. Fluid dynamics concepts 8

2.2.1. Nozzles 8

2.2.2. Coandă effect 11

2.2.3. Turbulence in internal combustion engines 14

2.3. Injection parameters 17

2.3.1. Rail and chamber pressure effects 17

2.3.2. Effect of the injection timing 21

2.3.3. Mixture formation 23

2.4. Injector selection design concept 26

2.4.1. Actuator selection 26

2.4.2. Valve type selection 27

2.5. Numerical model 28

2.5.1. Discretization and numerical schemes 28
2.5.2. Meshing 30
2.5.3. Boundary conditions 34
2.5.4. Turbulence modelling 35
2.6. X-Ray radiography 35

3. METHODOLOGIES AND PROCEDURES 38
3.1. Model setup 38
3.1.1. Cases for the model validation 38
3.1.2. Mixture formation 39
3.2. Computational matrix 41
3.2.1. Geometry 41
3.2.2. Pintle lift profile 43
3.2.3. Boundary conditions 44
3.2.4. Mesh definition 45
3.2.5. Turbulence model 51
3.2.6. Schmidt number 52
3.3. Data post-processing 52
3.3.1. Comparison between simulation results and experimental data 52
3.3.2. Evaluation of the mixture quality 55

4. RESULTS ON MODEL VALIDATION 57
4.1. Structure of the jet 57
4.2. Steady state results 58
4.2.1. Model validation 60
4.2.2. Other results 68
4.3. Transient results 78
4.3.1. Model validation 78
4.3.2. Other results 80

5. RESULTS ON MIXTURE FORMATION 82
5.1. Turbulence effect on the mixture formation 84
5.2. Off-center injector and turbulence effect on the mixture formation 86

6. CONCLUSIONS AND RECOMMENDATIONS 96

REFERENCES.....99

VITA AUCTORIS 103

LIST OF TABLES

- Table 2.1: CNG composition [5]. 6
- Table 2.2: Combustion and general properties of CNG [5] [6] [7]. 7
- Table 2.3: Main argon properties [8]. 8
- Table 2.4: Main characteristics of the considered computational grid [6]. 33
- Table 3.1: Conditions in which the experiments and the simulations were performed. 38
- Table 3.2: Conditions in which other simulations were performed. 39
- Table 3.3: Studied cases to evaluate the mixture formation. 40
- Table 3.4: Effect of the base cell size on the total number of cells, on smallest cell size, on the number of cells along the pintle opening, on the maximum Mach number and on the time to simulate 1 ms. 45
- Table 3.5: Embedding level, number of cells, smallest cell size and time to simulate 1 ms for three embedding distributions: Level 4, Level 5 and a combination of them. 49
- Table 3.6: Intervals used to evaluate the mixture quality. 56

LIST OF FIGURES

- Figure 1.1: Fuel consumption and CO2 emission regulations scenario between 1978 and 2023 [1] 1
- Figure 1.2: Efficiency with respect to engine RPM for three configurations (CNG DI, CNG PFI, Gasoline DI) of a small three cylinders engine [4] 2
- Figure 2.1: Converging nozzle [9] 9
- Figure 2.2: Converging-diverging nozzle [9] 10
- Figure 2.3: Coandă effect; on the left streamline curvature, on the right restricted entrainment [10] 12
- Figure 2.4: Example of a direct injection engine with lateral mounted injector [11] 13
- Figure 2.5: Coandă effect on a diesel jet [12] 13
- Figure 2.6: Swirl, normal tumble and sideways tumble in a combustion chamber [13] 14
- Figure 2.7: Average turbulence intensity with respect to crank angle in a combustion chamber with two different pistons [13] 15
- Figure 2.8: Turbulence length scale with respect to crank angle in a combustion chamber with two different pistons [13] 16
- Figure 2.9: Spray tip penetration with respect to time after the start of the injection for three rail pressures [8] 17
- Figure 2.10: Pressure with respect to crank angle for motoring cycle and rail pressure 19
- Figure 2.11: Chamber pressure effects on the jet characteristics [16] 20
- Figure 2.12: Percentage of CNG used from the tank with respect to the pressure at the tank output [4] 21
- Figure 2.13: Effect of the injection timing on the torque for an engine running at 1000 RPM and 1500 RPM [4] 22
- Figure 2.14: Liquid spray atomization [17] 23
- Figure 2.15: Percentage of flammable mixture with respect to the penetration depth for different chamber conditions [18] 24
- Figure 2.16: Mixture formation for an early injection timing (end of injection 207 CA deg BTDC) [19] 24
- Figure 2.17: Effect of the start of the injection (SOI) on the local reactive air fuel ratio (λ) and on the percentage of flammable mixture (f_m) at 30 CA deg BTDC [6] 25
- Figure 2.18: Inward opening and outward opening valve scheme for a DI injector [4] 27
- Figure 2.19: 1D representation of a grid scheme for finite volume methods [23] 29
- Figure 2.20: Cell size distribution [6] 32
- Figure 2.21 Influence of the grid resolution on the Mach number in the supersonic under-expanded region close to the injector exit [6] 32

- Figure 2.22: Influence of the grid resolution on the computed Mach number. Data collected along the mean jet path [6].....33
- Figure 2.23: X-ray radiography apparatus scheme [27] 36
- Figure 3.1: CAD model of the injector tip (fully open).....41
- Figure 3.2: On the left, the geometry of the model without impingement. On the right, the geometry of the model with a wall in front of the injector.....42
- Figure 3.3: Chamber geometry used for the mixture formation. On the left with a central injector. On the right with a off-center injector 42
- Figure 3.4: Normalized pintle lift profile.....43
- Figure 3.5: Partial section of the pressurized chamber upstream of the nozzle 45
- Figure 3.6: Normalized mass flow rate during the pintle opening and at steady state with a base cell size of 0.9 mm and 1 mm.....46
- Figure 3.7: Embedding levels comparison. From left to right: level 4, level 5 and combination of them 47
- Figure 3.8: Argon mass fraction with three embedding levels. From left to right: level 4, level 5 and combination of them 47
- Figure 3.9: Mach number with three embedding levels. From left to right: level 4, level 5 and combination of them.....48
- Figure 3.10: Normalized mass flow rate with respect to time for the experimental results and three embedding distributions: Level 4, Level 5 and a combination of them 48
- Figure 3.11: Normalized tip penetration with respect to time for the experimental results and three embedding distributions: Level 4, Level 5 and a combination of them 49
- Figure 3.12: Cells distribution using the adaptive mesh refinement 50
- Figure 3.13: Comparison between the results obtained with RNG $\boldsymbol{k}$-$\boldsymbol{\varepsilon}$ (on the left) and with standard $\boldsymbol{k}$-$\boldsymbol{\varepsilon}$ (on the right) 51
- Figure 3.14: Control volume, grid plane and grid line used to compute the projected density and the path length.....54
- Figure 3.15: Scheme of a jet and of the integration grid line 55
- Figure 4.1: Mass fraction of argon in the middle plane of the chamber.....57
- Figure 4.2: Position of the lines used to plot the path length, open chamber ...58
- Figure 4.3: Position of the lines used to plot the path length, closed chamber.59
- Figure 4.4: Normalized path length for the open case. Simulation and experimental results, 0.8 mm far from the injector, rail pressure 10 bar, chamber pressure 1 bar 60
- Figure 4.5: Normalized path length for the open case. Simulation and experimental results, 3 mm far from the injector, rail pressure 10 bar, chamber pressure 1 bar 61
- Figure 4.6: Normalized path length for the open case. Simulation and experimental results, 8 mm far from the injector, rail pressure 10 bar, chamber pressure 1 bar 61
- Figure 4.7: Normalized path length for the open case. Simulation and experimental results, 14 mm far from the injector, rail pressure 10 bar, chamber pressure 1 bar 62

- Figure 4.8: Normalized path length for the open case. Simulation and experimental results, 28 mm far from the injector, rail pressure 10 bar, chamber pressure 1 bar 62
- Figure 4.9: Schematic right view of the gas jet in a plane 0.8 mm far from the injector 63
- Figure 4.10: Normalized path length for the open case. On the left: simulation results. On the right: results of the experiments 64
- Figure 4.11: Normalized path length for the closed case. Simulation and experimental results, 0.8 mm far from the injector, rail pressure 10 bar, chamber pressure 1 bar 65
- Figure 4.12: Normalized path length for the closed case. Simulation and experimental results, 3.5 mm far from the injector, rail pressure 10 bar, chamber pressure 1 bar 65
- Figure 4.13: Normalized path length for the closed case. Simulation and experimental results, 8 mm far from the injector, rail pressure 10 bar, chamber pressure 1 bar 66
- Figure 4.14: Normalized path length for the closed case. Simulation and experimental results, 14 mm far from the injector, rail pressure 10 bar, chamber pressure 1 bar 66
- Figure 4.15: Normalized path length for the closed case. Simulation and experimental results, 19 mm far from the injector, rail pressure 10 bar, chamber pressure 1 bar 67
- Figure 4.16: Normalized path length for the closed case. On the left: simulation results. On the right: results of the experiments 68
- Figure 4.17: Normalized path length for the open case. 0.8 mm far from the injector, chamber pressure 1 bar, rail pressure 10 bar and 15 bar 69
- Figure 4.18: Normalized path length for the open case. 3 mm far from the injector, chamber pressure 1 bar, rail pressure 10 bar and 15 bar 69
- Figure 4.19: Normalized path length for the open case. 8 mm far from the injector, chamber pressure 1 bar, rail pressure 10 bar and 15 bar 70
- Figure 4.20: Normalized path length for the open case. 14 mm far from the injector, chamber pressure 1 bar, rail pressure 10 bar and 15 bar 70
- Figure 4.21: Normalized path length for the open case. 28 mm far from the injector, chamber pressure 1 bar, rail pressure 10 bar and 15 bar 71
- Figure 4.22: Normalized path length for the open case. 0.8 mm far from the injector, rail pressure 10 bar, chamber pressure 1 bar and 2 bar 72
- Figure 4.23: Normalized path length for the open case. 3 mm far from the injector, rail pressure 10 bar, chamber pressure 1 bar and 2 bar 72
- Figure 4.24: Normalized path length for the open case. 8 mm far from the injector, rail pressure 10 bar, chamber pressure 1 bar and 2 bar 73
- Figure 4.25: Normalized path length for the open case. 14 mm far from the injector, rail pressure 10 bar, chamber pressure 1 bar and 2 bar 73
- Figure 4.26: Normalized path length for the open case. 28 mm far from the injector, rail pressure 10 bar, chamber pressure 1 bar and 2 bar 74

- Figure 4.27: Normalized path length for the closed case. 0.8 mm far from the injector, chamber pressure 1 bar, rail pressure 10 bar and 15 bar 75
- Figure 4.28: Normalized path length for the closed case. 3.5 mm far from the injector, chamber pressure 1 bar, rail pressure 10 bar and 15 bar 75
- Figure 4.29: Normalized path length for the closed case. 8 mm far from the injector, chamber pressure 1 bar, rail pressure 10 bar and 15 bar 76
- Figure 4.30: Normalized path length for the closed case. 14 mm far from the injector, chamber pressure 1 bar, rail pressure 10 bar and 15 bar 76
- Figure 4.31: Normalized path length for the closed case. 19 mm far from the injector, chamber pressure 1 bar, rail pressure 10 bar and 15 bar 77
- Figure 4.32: Normalized tip penetration obtained in the simulation and in the experiments 78
- Figure 4.33: Normalized mass flow rate obtained in the simulation and in the experiments 79
- Figure 4.34: Normalized tip penetration with respect to time. Three open cases: rail pressure 10 bar, rail pressure 15 bar and chamber pressure 2 bar 80
- Figure 4.35: Normalized mass flow rate with respect to time. Three open cases: rail pressure 10 bar, rail pressure 15 bar and chamber pressure 2 bar 81
- Figure 5.1: Normalized mass flow rate with respect to time using methane and argon with a rail pressure of 10 bar and a chamber pressure of 1 bar. With methane, the complete injection is shown, also considering the closing period 82
- Figure 5.2: Normalized penetration with respect to time using methane and argon with a rail pressure of 10 bar and a chamber pressure of 1 bar 83
- Figure 5.3: Normalized penetration with respect to time using methane with a rail pressure of 10 bar and a chamber pressure of 1 bar. The result of the simulation is compared with two cases found in literature, [8] [18] 83
- Figure 5.4: Volume in flammable condition with respect to time AEOI. Central injector with a calm chamber and two turbulent chambers 84
- Figure 5.5: Volume in lean flammable and rich flammable conditions with respect to time AEOI. Central injector with a calm chamber and two turbulent chambers 85
- Figure 5.6: Volume in stoichiometric condition with respect to time AEOI. Central injector with a calm chamber and two turbulent chambers..... 86
- Figure 5.7: Methane mass fraction distribution during its injection with an off-center injector..... 87
- Figure 5.8: Methane mass fraction distribution during its injection with a side injector 87
- Figure 5.9: Volume in flammable condition with respect to time AEOI. Off-center injector with a calm chamber and two turbulent chambers..... 88
- Figure 5.10: Volume in stoichiometric condition with respect to time AEOI. Off-center injector with a calm chamber and two turbulent chambers..... 88
- Figure 5.11: Velocity distribution and vector arrows of the flow in the chamber. On top: two cases in which the chamber is turbulent at the beginning

of the process. Below: two cases in which the chamber is calm. On the left: time instant 2 ms AEOI. On the right: time instant 6 ms AEOI 89
- Figure 5.12: Volume in lean flammable, rich flammable and overall flammable conditions with respect to time AEOI. Central and off-center injector cases with a calm chamber 90
- Figure 5.13: Volume in stoichiometric condition with respect to time AEOI. Central and off-center injector cases with a calm chamber 91
- Figure 5.14: Volume in lean flammable, rich flammable and overall flammable conditions with respect to time AEOI. Central and off-center injector cases with the initial turbulent kinetic energy of the chamber equal to 73.5 m2/s2 .. 92
- Figure 5.15: Volume in stoichiometric condition with respect to time AEOI. Central and off-center injector cases with the initial turbulent kinetic energy of the chamber equal to 73.5 m2/s2 92
- Figure 5.16: Volume in lean flammable, rich flammable and overall flammable conditions with respect to time AEOI. Central and off-center injector cases with the initial turbulent kinetic energy of the chamber equal to 216 m2/s2 ... 93
- Figure 5.17: Volume in stoichiometric condition with respect to time AEOI. Central and off-center injector cases with the initial turbulent kinetic energy of the chamber equal to 216 m2/s2 94

LIST OF ABBREVIATIONS/SYMBOLS

°C	Degree Celsius
2D	Two dimensional
3D	Three dimensional
AEOI	After the end of the injection
AFR	Air fuel ratio
AMR	Adaptive mesh refinement
Ar	Argon
ARDC	Automotive Research and Development Centre
ASM	Algebraic stress model
bar	Bar pressure
BDC	Bottom dead center
BTDC	Before top dead center
bmep	Braking mean effective pressure
CA	Crank angle
CAD	Computer aided drafting
CFD	Computational fluid dynamics
CH_4	Methane
CNG	Compressed natural gas
CO_2	Carbon dioxide
CPR	Critical pressure ratio
CRF	Centro Ricerche Fiat
deg	Angle degree
DI	Direct injection
EGR	Exhaust gas recirculation
EPA	Environmental Protection Agency
EU	European Union
FCA	Fiat Chrysler Automobiles
FDM	Finite difference method
FEM	Finite element method
FVM	Finite volume method
g	Gram
h	Hour
Hz	Hertz
IVC	Intake valve closure
J	Joule
K	Kelvin
keV	Kilo electron volt
kg	Kilogram
l	Liter
LHV	Lower heating value
m	Meter

MJ	Mega Joule
min	Minute
mpg	Miles per gallon
ms	Millisecond
N_2	Nitrogen
NHTSA	National Highway Traffic Safety and Administration
PDE	Partial differential equation
PFI	Port fuel injection
RANS	Reynolds-averaged Navier-Stokes
RON	Research octane number
RPM	Revolutions per minute
TDC	Top dead center
s	Second
SI	Spark ignition
SOI	Start of injection

NOMENCLATURE

Symbols

a	Speed of sound
A_t	Throat area
c	Flow velocity
C_d	Discharge coefficient
C_μ	Turbulence length scale constant
D	Mass diffusivity
f_m	Flammable mixture
k	Kinetic energy
L_ε	Turbulence length scale
$\dot{m}$	Mass flow rate
m_{air}	Mass of air
M	Mach number
M_{Ar}	Argon molecular weight
M_{N2}	Nitrogen molecular weight
P	Absolute pressure
P_0	Stagnation pressure
P_1	Upstream absolute pressure
P_c	Critical pressure
P_d	Projected density
P_l	Path length
$P_{chamber}$	Absolute chamber pressure
P_{rail}	Rail pressure
R	Specific gas constant
S_c	Schmidt number
u'	Turbulence intensity
ν	Kinematic viscosity
v_1	Upstream specific volume
V_{Ar}	Argon molecular volume
V_{N2}	Nitrogen molecular volume
$V_{chamber}$	Chamber volume
y_{Ar}	Argon mass fraction
y_{CH4}	Methane mass fraction
y_{CNG}	CNG mass fraction

Greek symbols

γ	Heat capacity ratio
ε	Turbulence dissipation rate
λ	Reactive air to fuel ratio

μ	Dynamic viscosity
ρ	Density
ρ_0	Stagnation density
ρ_{air}	Air density
φ	Equivalence ratio

1. INTRODUCTION

Nowadays, the emission of carbon dioxide (CO2) is one of the most relevant issues for the environment. The strong effect that it has on the global warming and the catastrophic consequences it can produce are forcing our society to actuate increasingly stringent regulations to control its emission. In the last few years, a small tendency to reduce it has been observed. This is not going to be enough, for this reason a very strong effort is requested to the entire society. A large percentage of these emissions is caused by transportation and in particular by cars. For this reason, in the automotive field the regulations are even more stringent. Figure 1.1 shows the regulations scenario between 1978 and 2023 for what concerns fuel consumption and CO2 emission in the United States according to the Environmental Protection Agency (EPA) and the National Highway Traffic Safety and Administration (NHTSA) [1]. The plot clearly shows that a very strong reduction is requested both for cars and trucks.

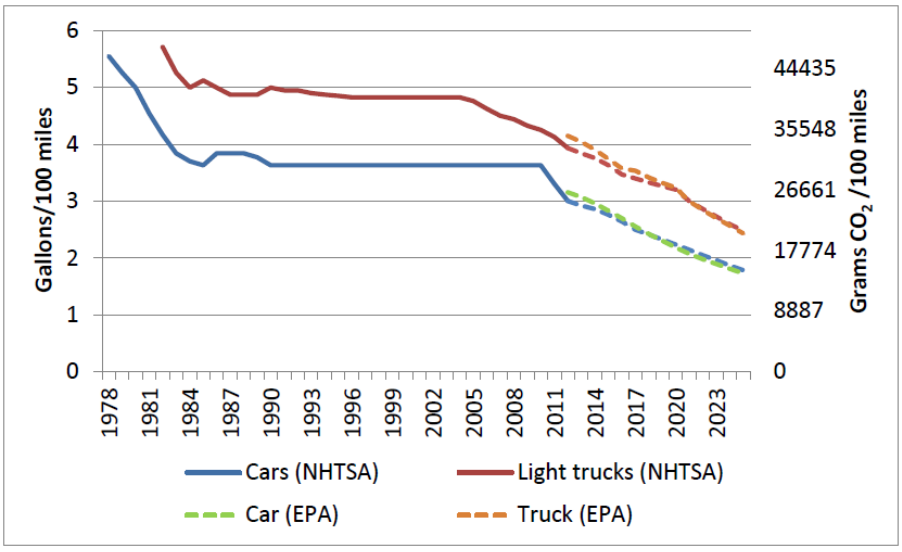

Figure 1.1: Fuel consumption and CO2 emission regulations scenario between 1978 and 2023 [1]

Carmakers are working extremely hard to reach the target and, since this is so demanding, the optimization and research of new solutions are fundamental in all parts of

the vehicle. One of the most important components of a car, concerning the emission of CO2, is the engine. A lot of research has been done especially looking at the most common fuels like gasoline and diesel. However, this is not enough, so the utilization of alternative fuels and technologies is of particular interest. Compressed natural gas seems to be a high potential fuel to reduce emissions and increase the efficiency.
Indeed, by using Compressed Natural Gas in port fuel injection spark ignition engines, it is possible to reduce the emission of CO2 up to 20% relative to gasoline engines [2]. Furthermore, CNG has a higher research octane number. This aspect allows to increase the compression ratio and, as a consequence, to increase the thermal efficiency and the output power of the engine.

Looking at the logical next step of this strategy, the direct injection of CNG can offer a further increase of the efficiency and a reduction of the emissions [3].

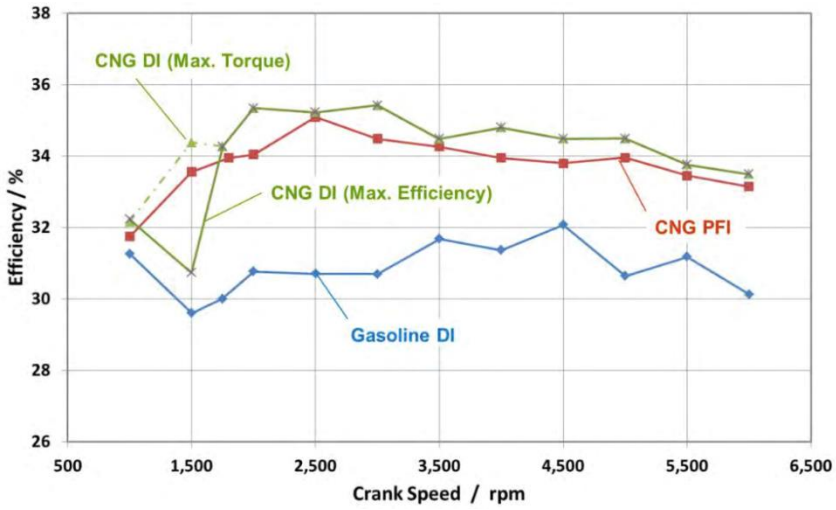

Figure 1.2: Efficiency with respect to engine RPM for three configurations (CNG DI, CNG PFI, Gasoline DI) of a small three cylinders engine [4]

Figure 1.2 shows a comparison between a CNG PFI and CNG DI relative to a Gasoline DI. These experimental results were obtained with a small three cylinder engine [4]. The advantage in terms of efficiency using a CNG DI is shown clearly by the plot. On the other hand, although it is not shown in this plot, one of the main drawbacks of using CNG is related to the output torque that can be obtained, which is generally lower than

achieved using gasoline. Due to its larger volume, the gaseous fuel substitutes part of the air entering the chamber, reducing in this way the quantity of fuel that can be burnt as well.

This issue can be solved quite easily using a turbo. However, even with its help, at low engine speed the power available for the compressor could be not enough in order to compensate the loss in volumetric efficiency.

Direct injection can help to deal with the problem previously mentioned related to the usage of the turbo. At low RPM with a DI engine it is possible to inject all the fuel when the intake valves are closed, in such a way not to reduce the volumetric efficiency. Eventually, it is possible to obtain the same torque of gasoline engines.

Direct injection of CNG is quite a new technology. Few studies have been done in the past and for this reason the research of the optimal strategies is still a relevant issue. This technology is not so diffused because of the difficulties related to the creation of a good mixture in a short time. As it will be discussed later, this happens mainly because the fuel is gaseous and so turbulence does not have a big effect on the mixture formation. For this reason, the goal of this thesis is to realize a 3D CFD model for the simulation of a direct injection of CNG and to evaluate the effect of some parameters on the mixture formation.

1.1. Objectives

This project has the goal of developing and validating a model of a DI CNG injector to evaluate the quality of the air fuel mixture. This is done by injecting CNG into a constant volume chamber with different configurations. The project can be mainly divided into two main parts:

- The first part of the work is focused on the development of a 3D CFD model using the software Converge^{TM}. Two different cases are used for validation: the first one with an open chamber, the second one with a wall positioned in front of the injector in order to study the impact of the flow against a barrier. The results are validated against some experimental data provided by FCA. The mentioned data were obtained using X-ray radiography.

- The second part is focused on the analysis of the mixture formation. Six cases, resulting from a combination of different parameters, are analyzed. The aforementioned parameters are basically two: the position of the injector and the presence of a turbulent flow in the chamber. In particular, the injector is placed at the center of a wall or in an off-center position. In order to evaluate the effect of turbulent air in the chamber, the case with calm air is compared with two other cases in which an initial turbulent kinetic energy is imposed. The equivalence ratio at each point of the domain is evaluated in order to compare the obtained results and see how the mixture quality changes. The objective is to find the combination of parameters that can give the highest percentage of stoichiometric mixture in the shortest time. Moreover, since the time to form a flammable mixture in a DI CNG engine is generally short, especially if the engine works in stratified conditions, the flammable limits are also taken into account.

1.2. Thesis organization

- **Chapter 2:** this chapter presents all the literature review performed in the first phase of the project. It treats in detail all the most important aspects of the direct injection of natural gas and the numerical aspects related to the model development, in order to give the reader a better understanding of the topic.

- **Chapter 3:** this chapter describes the cases analyzed, the steps required for the model setup with a quick comparison of the possible solutions and, finally, how the data are post-processed.

- **Chapter 4:** this chapter shows the results obtained in the first part of the project. The data are compared with the experimental ones to validate the model. First the path length for steady state conditions is analyzed and then the same is done for the penetration and the mass flow rate. Moreover, the effect of rail and chamber pressure on the jet is analyzed looking at the same parameters.

- **Chapter 5:** this chapter presents the results obtained in the second part of the project. This has the goal of studying the influence of some parameters on the mixture formation. At the beginning, a central injector is used with a constant volume chamber and the effect of the turbulence in the chamber (imposed as initial condition) is analyzed. Then, the same is done with an off-center injector. At the end the two injectors are compared.

- **Chapter 6:** this last chapter describes the conclusions of the project and the recommendations for future work.

2. LITERATURE REVIEW

Before starting the development of the 3D CFD model, it is fundamental to acquire a deep knowledge of the theoretical aspects related to the described objectives. The literature review has the goal of studying and discovering the main issues that can be encountered in this research work.

2.1. CNG and Argon properties

As mentioned before, the first goal of this work is the realization of a 3D CFD model for the injection of CNG. However, its validation is done using argon, instead of CNG. For this reason, it is worth noting what the properties of these two gases.

CNG is composed mainly by methane; however, many other gases are present in its composition. The entire list defined by Union Gas is shown in the Table 2.1 .

Component	Typical Analysis (mole %)	Range (mole %)
Methane	95.0	87.0 - 97.0
Ethane	3.2	1.5 - 7.0
Propane	0.2	0.1 - 1.5
iso - Butane	0.03	0.01 - 0.3
normal - Butane	0.03	0.01 - 0.3
iso - Pentane	0.01	trace - 0.04
normal - Pentane	0.01	trace - 0.04
Hexanes plus	0.01	trace - 0.06
Nitrogen	1.0	0.2 - 5.5
Carbon Dioxide	0.5	0.1 - 1.0
Oxygen	0.02	0.01 - 0.1
Hydrogen	trace	trace - 0.02

Table 2.1: CNG composition [5]

In consideration of the final goal of this project, which is the engine application, the combustion properties are of importance. These are shown in Table 2.2. Moreover, some general properties of CNG are reported in the last rows.

Property	Typical value
Lower Heating Value (LHV)	47.141 MJ/Kg
Research Octane Number (RON)	130
Ignition Point	866 K
Flammability Limits	4% - 16% (volume % in air) 2.38% - 8.88% (mass % in air)
Theoretical Flame Temperature (stoichiometric air/fuel ratio)	2233 K
Maximum Flame Velocity	0.3 m/s
Relative density (specific gravity)	0.58
Mass density (ambient conditions)	0.688 kg/m^3
Mass density (293 K, 20 MPa)	167.941 kg/m^3
Molar mass	16.8036 kg/kmol

Table 2.2: Combustion and general properties of CNG [5] [6] [7]

Analyzing these values some important comments can be made. First, CNG has a higher LHV than gasoline (gasoline LHV is generally close to 43.239 MJ/kg [7]). However, the energy per unit volume of the gaseous fuel is much lower if compared with the one of gasoline, even with a tank at 20 MPa. This means that the tank volume in the vehicle, to store the same amount of energy, must be about four times bigger using CNG.

Looking at its research octane number (RON), CNG has a higher value than gasoline. This is a very important characteristic of CNG because it allows increasing the volumetric compression ratio and, as consequence, also the thermal efficiency becomes higher.

Another important property is the laminar flame speed. With CNG this is a bit slower than to gasoline. This is a negative effect because the combustion needs more time to be completed. In this way also the thermal efficiency is penalized.

The main argon properties are shown in Table 2.3. The molar mass is of relevance because, since it is higher than the one of CNG, this gas is more proper for X-ray radiography. This aspect will be explained more fully later.

Property	Typical value
Group number	18
Molar mass	39.948 kg/kmol
Density	1.633 kg/m^3
Heat capacity ratio	1.66
State at 293 K	gas

Table 2.3: Main argon properties [8]

2.2. Fluid dynamics concepts

2.2.1. Nozzles

Since this project is focused on the behavior of the injector, looking in detail at the shape of the jet, it is important to understand how nozzles work.

A nozzle is a duct of varying cross-sectional area in which the velocity of a compressible fluid increases and pressure decreases. Thus in a nozzle, the fluid enters duct with small velocity and high pressure and leaves it with high velocity and small pressure. In this way, the enthalpy of the flow drops, and the heat drop in expansion is spent in increasing the velocity of fluid. On the contrary, a duct is called diffuser if the fluid is decelerated, causing a rise in pressure along the direction of flow.

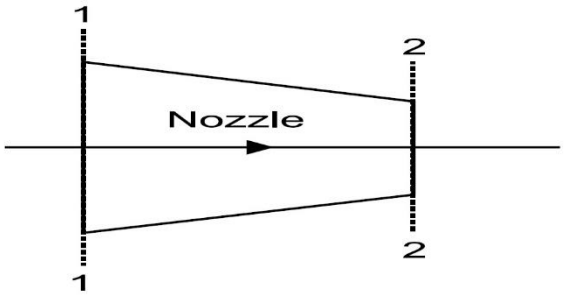

Figure 2.1: Converging nozzle [9]

Looking at the flow properties, some definition must be listed:

- M<1 flow is called subsonic flow.
- M=1 flow is called sonic flow.
- M>1 flow is called supersonic flow.

Here M is the Mach number defined as the ratio of the fluid velocity to the speed of sound, as shown in equation (2.1). The speed of sound is defined as in equation (2.2).

$$M = \frac{C}{a} \tag{2.1}$$

$$a = \sqrt{\gamma RT} \tag{2.2}$$

Where γ is the heat capacity ratio, R is the specific gas constant and T is the temperature. The flow is choked when it reaches the speed of sound in the throat of the nozzle. This happens when the pressure drop between downstream and upstream is lower than the critical pressure ratio. This ratio is defined as:

$$\frac{P_c}{P_0} = \left(\frac{2}{\gamma + 1}\right)^{\frac{\gamma}{\gamma - 1}} \tag{2.3}$$

In air, since the heat capacity ratio (γ) is equal to 1.4, the critical pressure ratio is 0.528. With argon, γ is 1.66 so the critical pressure ratio is 0.488.

When the flow is choked, the maximum discharge coefficient, or mass flow rate, is reached. It is defined in equation (2.4).

$$\frac{\dot{m}}{A_t} = \sqrt{\gamma \frac{P_0}{v_0} \left(\frac{2}{\gamma + 1}\right)^{\frac{(\gamma+1)}{(\gamma-1)}}} \tag{2.4}$$

A_t is the throat area, P_0 and v_0 are the total pressure and the total specific volume upstream from the nozzle, respectively. A nozzle operating with maximum mass flow rate condition is called a choked flow nozzle [9]. At the critical pressure ratio the velocity at exit is equal to the speed of sound. If the back pressure is reduced below critical pressure then the mass flow remains at maximum value and exit pressure remains as critical pressure. The fluid leaving the nozzle at critical pressure expands violently down to the reduced back pressure value. In this case the nozzle is called an under-expanded converging nozzle.

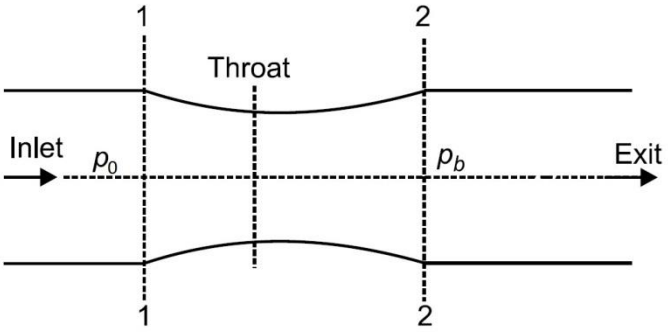

Figure 2.2: Converging-diverging nozzle [9]

In the case of a convergent-divergent nozzle, shown in the Figure 2.2, the situation is a bit more complicated. These kinds of nozzles are generally used for accelerating the flow up to supersonic velocity. In this case, when the pressure ratio is lower than the critical one, the behavior of the flow in the converging region is the same of a normal converging nozzle and the maximum mass flow rate is obtained. However, the fluid passing through the throat continues to expand and accelerate in the diverging portion of nozzle. Flow velocity beyond the throat is supersonic in the diverging portion of nozzle. At the section downstream of the throat, if the back pressure is not low enough, discontinuity in the flow can occur due to abrupt irreversible increase in pressure accompanied by deceleration from supersonic to subsonic velocity. This discontinuity in flow is called a shock and generally, the plane of discontinuity is normal to the direction of flow so it

may also be called a normal shock. If the downstream pressure is further decreased, the normal shock moves toward the exit of the nozzle. For a particular back pressure value, the isentropic expansion occurs throughout nozzle and no shock is found in the flow. If the back pressure is even lower than the ideal case, it causes breaking of flow at downstream of nozzle exit. An abrupt expansion of irreversible type occurs at nozzle exit, creating a shock [9].

Analyzing the problem of the injection from a fluid dynamics point of view, it is very close to the widely studied case of an under-expanded compressible flow exiting from an orifice. The rail pressure under normal engine operation is close to 10 bar (or higher), whereas the pressure in the combustion chamber during the injection is usually between approximately 0.5 and 3 bar, thus causing the flow to become choked. Looking at discussions in the literature, injectors generally behave like under-expanded converging-diverging nozzles. Moreover, also a shock wave can be present at the exit [6].

2.2.2. Coandă effect

The Coandă effect is the tendency of a fluid jet to be attracted to a nearby surface. The principle was named after Romanian aerodynamics pioneer Henri Coandă, who was the first to recognize the practical application of the phenomenon in aircraft development in 1910.

This effect is famous for its application with aircrafts and the generation of a lift effect on wings. In the automotive field, this effect is studied for aerodynamic reasons with high performance cars. However, this principle can be also applied to the flow exiting the injector and expanding in the chamber.

The Coandă effect describes the tendency of a jet to follow the contours of an adjacent boundary even when this boundary curves away from the initial jet axis. This effect either arises due to the pressure gradient perpendicular to a curved streamline, or differential entrainment and the development of a partial vacuum.

In the first case it may be shown using the Euler equation (or the Bernoulli Equation in an incompressible fluid) that a curved streamtube experiences a net force towards the center

of curvature (Figure 2.3, left). Since no component of the viscous force acts perpendicular to a streamtube, this implies that $P_1 > P_2$. This pressure gradient causes the jet to be deflected from its initial axis, and accounts for the so-called Coandă effect.
Alternatively, if a jet is discharged in the vicinity of a solid boundary (Figure 2.3, right), the entrainment of fluid into the jet will be restricted on one side (A). This creates a partial vacuum so that $P_a < P_b$, and consequently the jet attaches to the flow boundary.

Figure 2.3: Coandă effect; on the left streamline curvature, on the right restricted entrainment [10]

In engine application all the flows, both air and fuel, are moving at high speed in a small chamber, so very close to the walls of the cylinder. In particular, looking at the topic of this thesis, more attention is paid to the fuel flow coming out from the injector. In the case of a central injector, since the flow is quite far from the lateral walls of the cylinder, the Coandă effect is not present. With an injector mounted in lateral position, as the one shown in Figure 2.4, the head is very close to the fuel jet and so the Coandă effect can be present. With this type of geometry, it is likely to happen that the jet will be attracted and guided by the wall above.

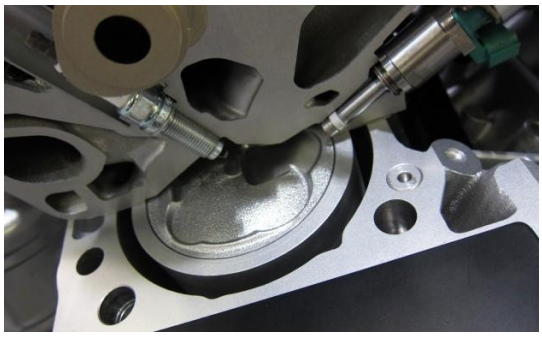

Figure 2.4: Example of a direct injection engine with lateral mounted injector [11]

Some research on this effect has been done especially for Diesel engines. In this case the fuel is liquid but, since it is broken in droplets and vaporized very soon, the behavior of gas fuel is not much different. Figure 2.5 shows the Coandă effect on a diesel jet. In the top left figure the free jet is shown, in the other figures a wall is placed at different distances from the injector.

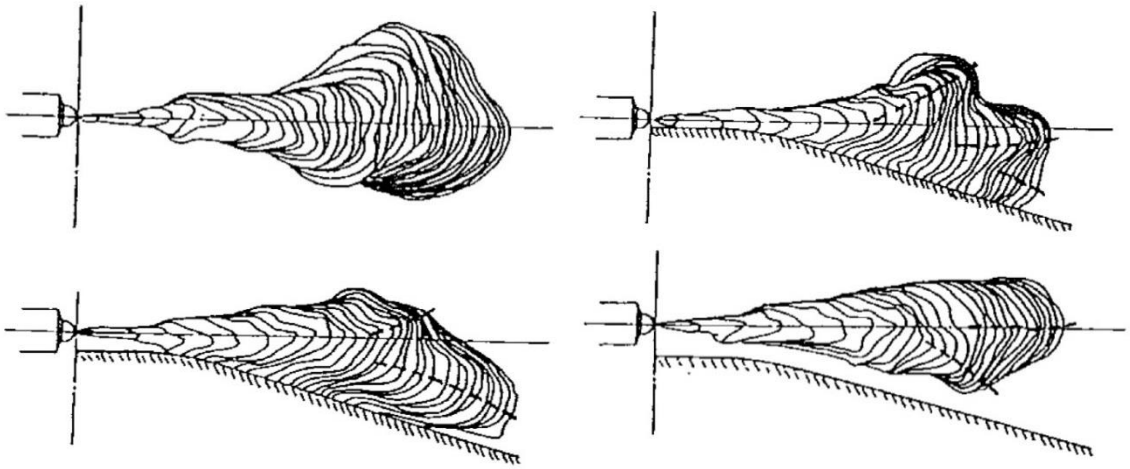

Figure 2.5: Coandă effect on a diesel jet [12]

The Coandă effect is clearly visible on the jet shape. The wall is attracting the flow even if the fuel is not touching the wall; this case is shown in the bottom right figure.

2.2.3. Turbulence in internal combustion engines

In the chamber of an internal combustion engine, the flow is turbulent during the entire cycle. In particular, swirl and tumble flows are always generated during intake and compression stroke. Swirl refers to a rotational flow within the cylinder about its axis and is used to promote rapid combustion. Tumble is a rotational motion about a circumferential axis near the edge of the clearance volume in the piston crown or in the cylinder head. It is caused by squishing of the in-cylinder volume as the piston reaches TDC.

Both swirl and tumble flows are commonly characterized by a dimensionless parameter used to quantify rotational and angular motion inside the cylinder. These values are calculated by the effective angular speed of in-cylinder air motion divided by the engine rotational speed [13].

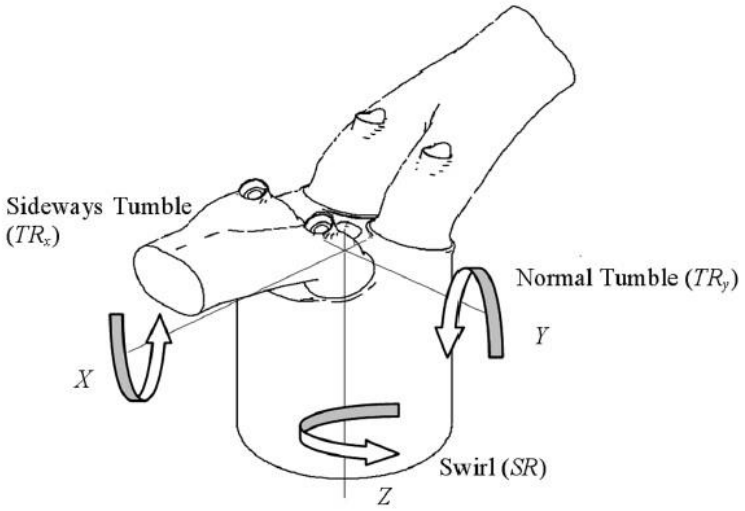

Figure 2.6: Swirl, normal tumble and sideways tumble in a combustion chamber [13]

The in-cylinder air motion, before fuel injection, is very important to create a proper air-fuel mixture. It affects the complete combustion in the engine cylinder and, finally, the engine performance. From the viewpoint of the fundamental turbulence physics, the two major parameters required to describe the turbulent flow characteristics are the turbulent kinetic energy (k) and its dissipation rate (ε).

The turbulent kinetic energy is related to the turbulence intensity, which is a measure of the characteristic speed of the turbulent flow over a distance characteristic. On the other hand, the turbulent dissipation rate is associated to the turbulence length scale, which is a quantitative measure of the distance characteristics of the flow structure. Moreover, the turbulent kinetic energy, during intake and compression stroke, can be obtained from the turbulence intensity of the k-ε model, defined in equation (2.5). With this equation, the intensity is assumed to be constant in all the directions, so isotropic.

$$u' = \sqrt{\frac{2k}{3}} \tag{2.5}$$

Some studies have been done to evaluate how the turbulence intensity evolves in a chamber. In particular, in a previous research the effect of two different pistons on the turbulence inside the chamber has been studied [13]. The results obtained are shown in Figure 2.7. These plots were obtained with a 3D CFD simulation.

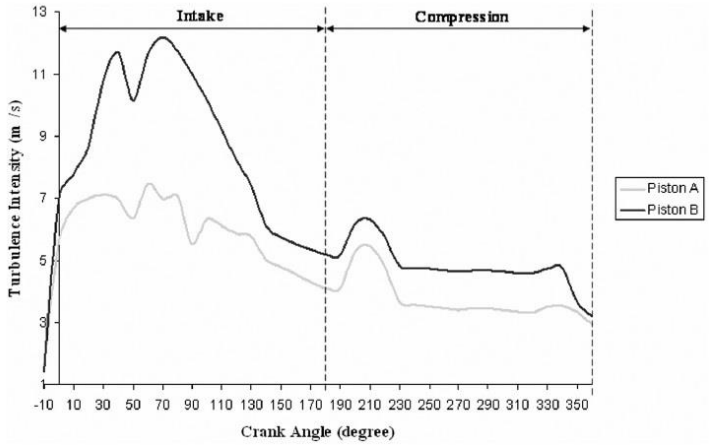

Figure 2.7: Average turbulence intensity with respect to crank angle in a combustion chamber with two different pistons [13]

This study gives an idea of how the turbulence behaves during the intake and the compression stroke. A typical maximum value for the intensity, during the intake, is between 7 m/s and 13 m/s. In some research study, the evaluation has also been done for the turbulent length scale. The results are shown in Figure 2.8.

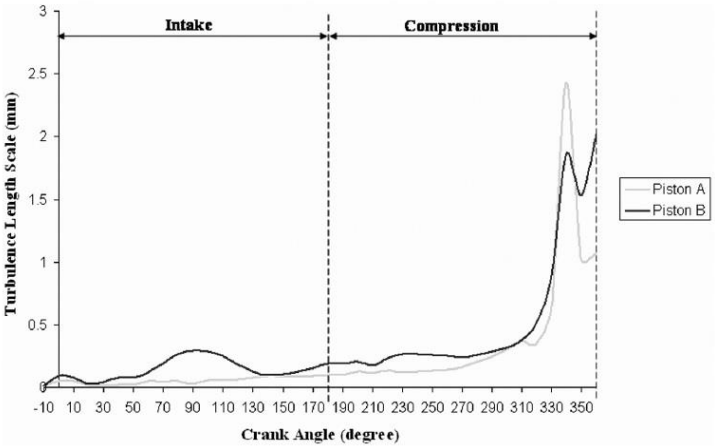

Figure 2.8: Turbulence length scale with respect to crank angle in a combustion chamber with two different pistons [13]

Starting from the turbulence length scale L_ε, it is possible to evaluate the dissipation rate with equation (2.6) [13].

$$\varepsilon = c_\mu^{3/4} \frac{k^{1/2}}{L_\varepsilon} \tag{2.6}$$

Where C_μ is a constant equal to 0.09.

As can be seen from the diagrams shown, the intensity is higher during the intake stroke. The cause is related to the velocity of the entering air. The highest intensity is generated when the piston speed is maximum.

During the compression, there is not a source of turbulence and for this reason its intensity is decreasing. As a consequence of this condition, the length scale increases.

2.3. Injection parameters

2.3.1. Rail and chamber pressure effects

The fuel rail pressure and the chamber pressure have considerably effects on the behavior of the spray, especially on the tip penetration and on the mass flow rate. To have a complete understanding of this work, an analysis of this aspect is fundamental.

First of all, the effect of rail pressure is studied taking into account what is present in literature for gaseous injections.

Figure 2.9 shows the effect of rail pressure on the tip penetration. In the cases considered rail pressure is equal to 1 MPa, 3 MPa and 5 MPa. The pressure in the chamber is fixed and equal to 0.1 MPa. As can be noticed, the penetration is higher when the pressure is higher but this effect is smaller if the pressure increases too much.

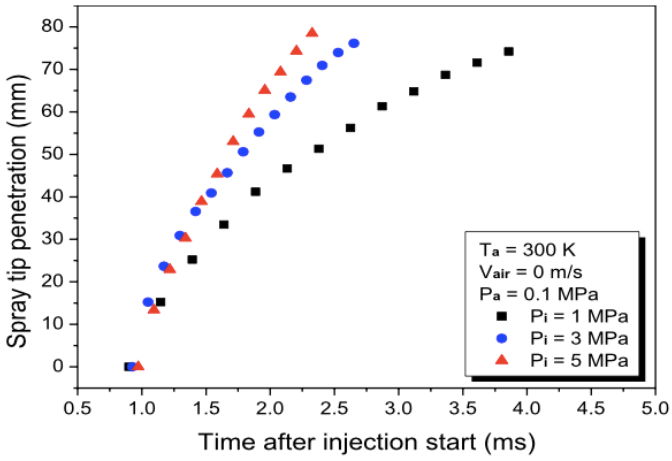

Figure 2.9: Spray tip penetration with respect to time after the start of the injection for three rail pressures [8]

Looking at the mass flow rate, the final value is strictly related to both the upstream and downstream pressures of the injector. Then, considering a compressible flow, if the pressure ratio is lower than the critical one, the mass flow rate can be computed with

equation (2.8). Equation (2.7) shows the definition of critical pressure ratio. The value is obtained considering a heat capacity ratio equal to 1.667 [14].

$$CPR = \frac{p_{chamber}}{p_{rail}} = \left(\frac{2}{\gamma + 1}\right)^{\frac{\gamma}{\gamma - 1}} = 0.4871 \tag{2.7}$$

$$\dot{m} = C_d A \sqrt{\gamma \rho_0 P_0 \left(\frac{2}{\gamma + 1}\right)^{\frac{\gamma+1}{\gamma-1}}} \tag{2.8}$$

It is important to specify that p_{rail} indicates the total pressure of the rail, so the pressure that the gas has when its velocity is zero.

Since the mass flow rate is strictly related to the pressure, it is clear that the rail pressure used for a port fuel injector (generally lower than 8 bar) is not enough.

This is mainly due to two reasons. First of all, with a lower rail pressure the penetration is lower, as shown before in Figure 2.9. It penalizes the mixture formation, as it will be shown later.

Second, in direct injection engines, the mass flow rate must be higher with respect to port fuel injection. The reason is related to the injection timing. With direct injection, the injection can happen during the intake and at the beginning of the compression stroke. For this reason, since the time to complete the injection is shorter, the mass flow rate must be high enough to guarantee the necessary amount of fuel. Moreover, as it will be shown later, in some cases it is necessary to inject the fuel after the intake valves closure and this is going to limit even more the time available.

The rail pressure, according to the characteristic of the injection system, is in the range between 10 bar and 15 bar [15]. According to the information reported by FCA, the chamber pressure during the injection must be between 1 bar and 2 bar. In these conditions, the flow is choked. Looking at engine applications, since the injection can happen at the beginning of the compression stroke, the pressure inside the chamber can be much higher.

Figure 2.10 shows the in cylinder pressure for a motoring cycle. Both the expansion and the compression are considered isentropic. This result is obtained by the author considering a volumetric compression ratio equal to 13. This value, for the compression ratio, is very high for a gasoline engine but it is quite normal for a CNG engine.

Moreover, the computed in-cylinder pressure is compared to a rail pressure of 15 bar. This comparison is useful to evaluate the pressure ratio with respect to the crank angle but also to know the interval in which the fuel can be injected. It must be remembered that the rail pressure must be always higher than the pressure inside the chamber, otherwise the injection cannot happen.

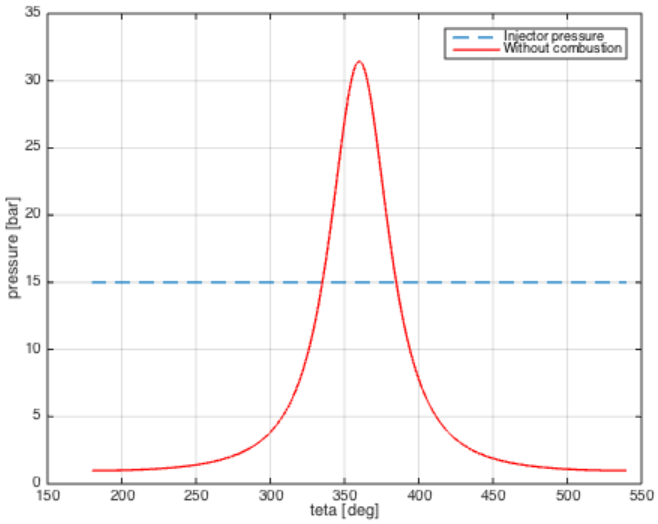

Figure 2.10: Pressure with respect to crank angle for motoring cycle and rail pressure

The chamber pressure has also an effect on the penetration and on the shape of the jet. This can be observed in Figure 2.11.

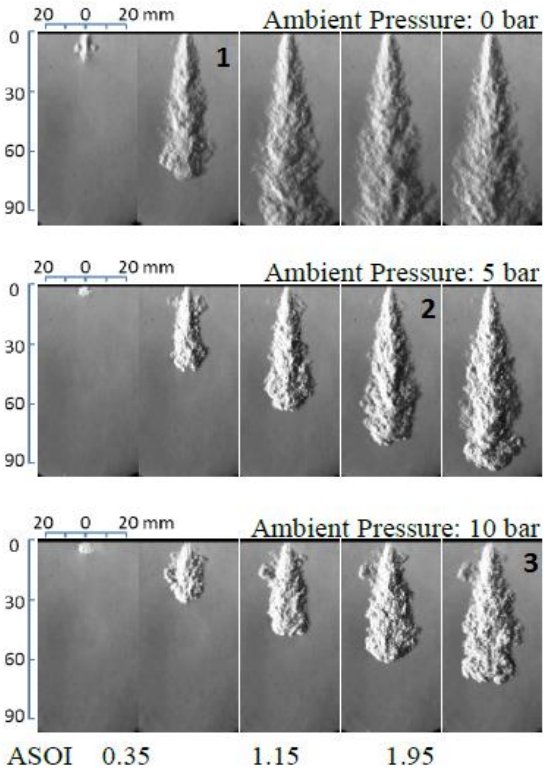

Figure 2.11: Chamber pressure effects on the jet characteristics [16]

The images show a transient CNG free jet under different ambient pressure ranging from 0.0 to 10 bar with the injection pressure of 85 bar. Series of photographs were captured in time order from the beginning of injection signal. Based on the qualitative observation of these images, the penetration decreases apparently and the time reaching the front wall was delayed as the chamber pressure increases [16]. Moreover, comparing the images 1, 2 and 3 that are showing three time instants with a similar penetration length, it can be seen that also the width increases if the chamber pressure increases.

The rail pressure has another important effect that must be taken into account. This can be seen in Figure 2.12.

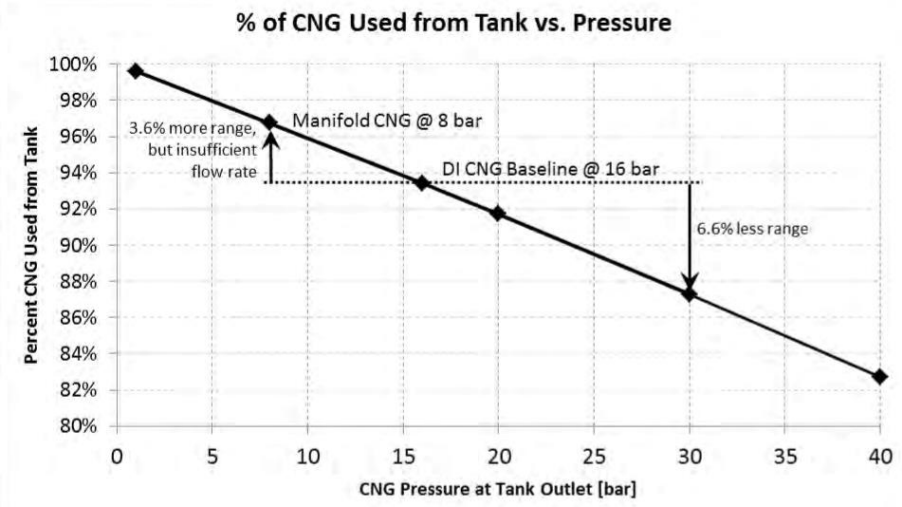

Figure 2.12: Percentage of CNG used from the tank with respect to the pressure at the tank output [4]

This figure shows that an increase of the rail pressure has a negative effect on the percentage of fuel that can be exploited in the tank. If the rail pressure is equal to 8 bar, with a tank charged at 200 bar, about 96% of fuel can be used. If the rail pressure is 16 bar, the percentage of fuel that can be exploited is less than 94%.

2.3.2. Effect of the injection timing

The injection timing is another aspect that influences the behavior of an engine and that must be analyzed. The timing is a strong parameter because it influences the quality of the mixture. Moreover, it can also affect the braking mean effective pressure (bmep) and, as a consequence of this, the output power.

The precise effect of the injection timing on the output torque can be seen in Figure 2.13. The relative output torque is shown for different injection timings, between 360 and 120 CA deg BTDC. In the plot, also the intake valve closure (IVC) is shown, it happens about 160 CA deg BTDC. In particular, when the injection starts before the IVC, the output torque is lower. The reason is related to the reduction of the volumetric efficiency. As explained before, the gaseous fuel substitutes a large part of the air entering the cylinder because its density is low. In a gasoline engine, this is not the case because the fuel is

liquid and so, since part of it evaporates during the injection, the overall temperature decreases and the density increases. If the density of air is higher, the mass is bigger.

At high engine speed, if the injection starts after the IVC, the time available is not enough to inject the request amount of fuel. For this reason, the injection must start before the IVC. In these conditions, the boosting power of the turbine and of the compressor is enough to increase the output torque. An output torque similar to the one of a gasoline engine can be obtained.

If the load is max, also at low engine speed it could be necessary to start the injection before the IVC. In this case, a delayed ignition can avoid a reduction of the output torque. When the ignition is delayed the amount of energy of the exhaust gases is higher and so, thanks to the turbine and the compressor, the engine can be boosted more. However, this solution reduces the efficiency.

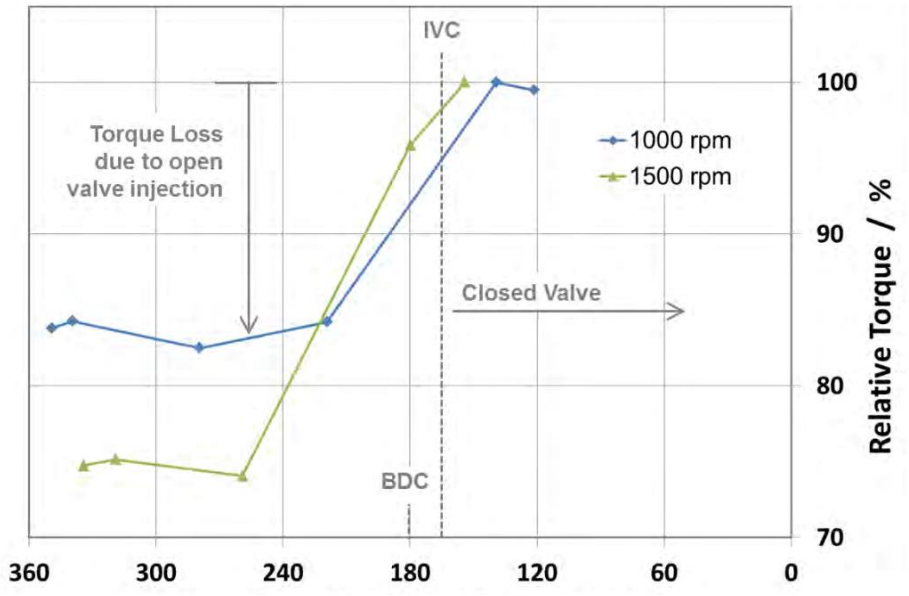

Figure 2.13: Effect of the injection timing on the torque for an engine running at 1000 RPM and 1500 RPM [4]

Despite the positive effect on the output torque, the late injection has a negative effect on the mixture formation. This aspect will be discussed in the next section.

2.3.3. Mixture formation

As explained in the objectives, one of the first goals of this work is the study of the mixture formation. Since CNG is gaseous, its behavior is much different with respect to gasoline or diesel. For several reasons, the last two offer the possibility to create a better mixture in less time.

First of all, the liquid jet is broken in droplets quite soon downstream from the injector. This aspect allows the air to enter in the gaps formed between droplets. Second, the evaporation of the droplets helps further the mixing of the fuel with air. Finally, with a liquid injection the mixture formation can be improved a lot thanks to the turbulence of the air.

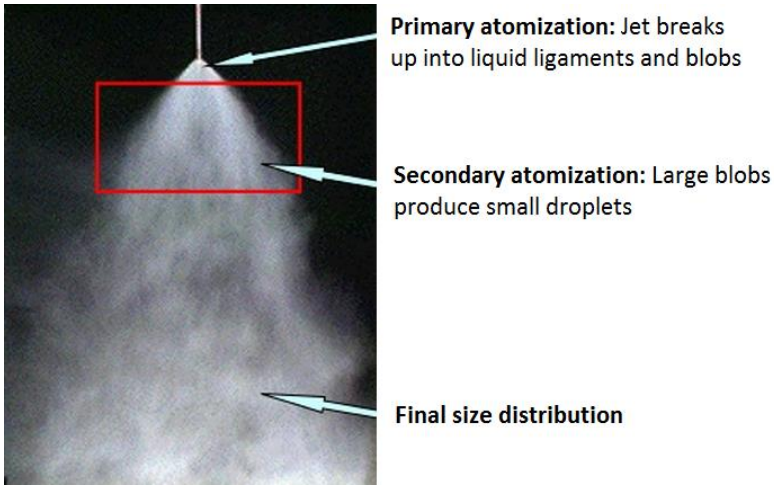

Figure 2.14: Liquid spray atomization [17]

Looking at the injection of CNG, the situation is much different. Previous studies show that the gaseous fuel forms a solid jet difficult to break. In a research project found in literature [18], a CNG injector was mounted on the top of a box in which two moving plates were positioned. The idea was to generate a turbulent motion of the air to improve its mixing with the fuel. Different strategies were analyzed, in some cases the fuel was injected while the plates were moving and in others as soon as the plates stopped. Moreover, different oscillations frequency and initial velocities were considered.

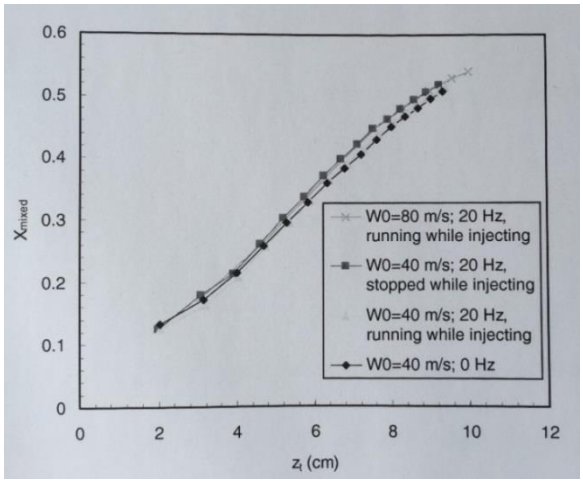

Figure 2.15: Percentage of flammable mixture with respect to the penetration depth for different chamber conditions [18]

Looking at Figure 2.15, when the plates are moving with a frequency of 20 Hz the mixing speed increases just a bit [18]. However, the results demonstrate that the turbulence of the air has a very small effect on the mixture formation.

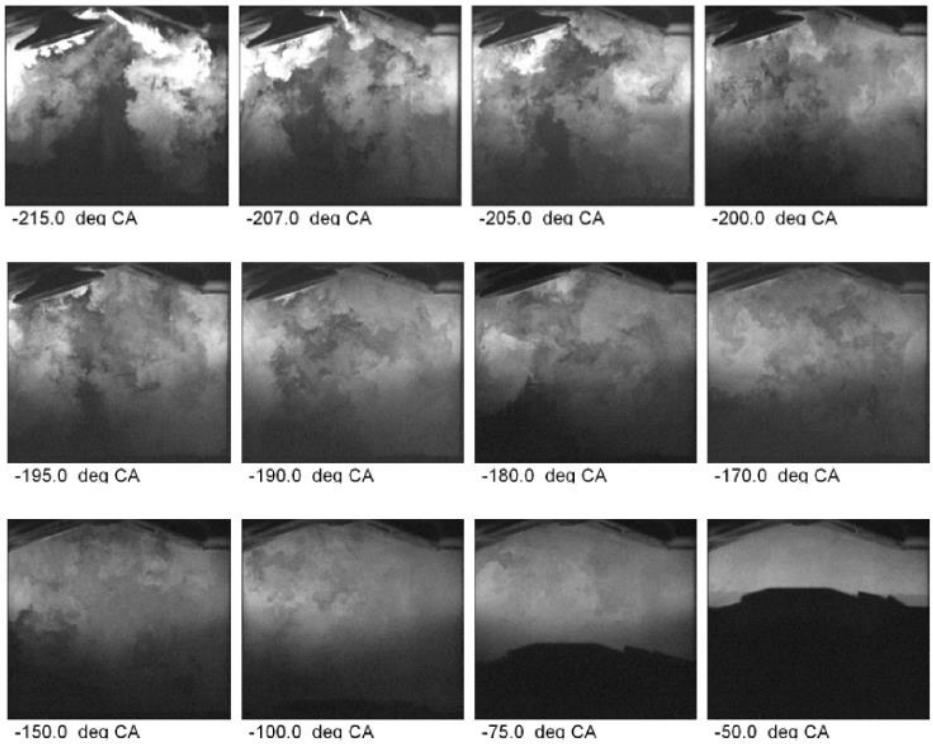

Figure 2.16: Mixture formation for an early injection timing (end of injection 207 CA deg BTDC) [19]

In a previous research work, in which a complete engine cycle was analyzed, the fuel was well mixed with air before the ignition if the injection ends 200 CA deg BTDC or earlier (as shown in Figure 2.16 [19]). This means that the time available to create the mixture is not an issue with an early injection.

However, for what is seen in the previous section, to have a higher torque in some cases a late injection is requested. In these conditions the mixture formation becomes an issue. This can be seen in Figure 2.17. When the injection is delayed too much, the mixture quality decreases a lot. For example, if the injection starts 80 CA deg BTDC, only 13% of the mixture is flammable 30 CA deg BTDC. Moreover, in the region close to the injector, the mixture is too rich at the moment in which the ignition should occur. It must be underlined that, in the described case, the injection starts during the compression, so very late. In real applications, this could happen only at low engine speed or at low load, if the engine works with a stratified mixture.

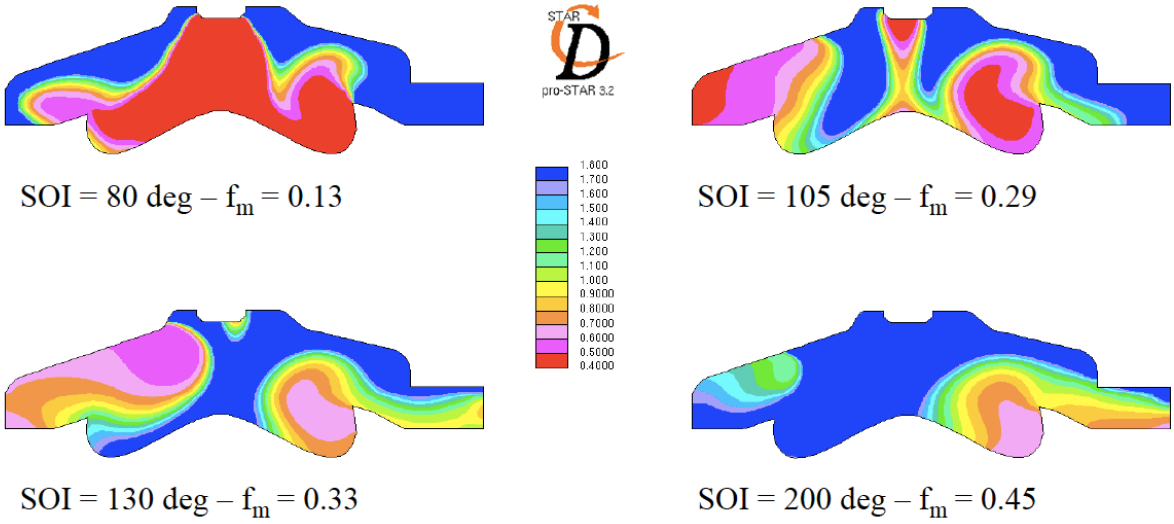

Figure 2.17: Effect of the start of the injection (SOI) on the local reactive air fuel ratio (λ) and on the percentage of flammable mixture (f_m) at 30 CA deg BTDC [6]

2.4. Injector selection design concept

In the design of an injector, to satisfy the necessary requirements, two fundamental choices must be made: the actuator type and the valve type [4]. These choices were made at the beginning of the project by FCA. However, to give to the reader a better understanding of the topic, a brief summary of this analysis is reported in the following subsections.

2.4.1. Actuator selection

The actuator choice is very important because this device moves another very important part of the injector, the pintle. In this way, the actuator has the goal of controlling the fueling time.
Nowadays, most of the injectors for direct injection use electromagnetic solenoid actuators but some of them use a piezo-electric one. For this reason, before starting the development of the model, it is worth to do an analysis of the different aspects that influenced the choice of the actuator type. The criteria used to make the choice were:

- Suitability for large pintle lift to meet the flow target (considering that the fuel is gaseous).
- Suitability for long pulse widths (because the mass flow rate is lower and so the time must be longer with respect to a liquid fuel)
- Capability of delivering a small fuel quantity.
- Complexity of the thermal compensation.
- Cost.

After an accurate analysis, it was observed that the piezo-electric actuator was better than the electromagnetic one just looking at the minimum quantity of fuel that can be injected. In all the other aspects, the electromagnetic actuator has a better behavior. For this reason, this one was chosen.

2.4.2. Valve type selection

Today, most direct injectors are inward opening and multi-hole, especially with liquid fuels. However, some do use an outward-opening valve. Figure 2.18 shows a schematic representation of an inward opening valve and of an outward opening one.

Figure 2.18: Inward opening and outward opening valve scheme for a DI injector **[4]**

The selection of the valve type for this kind of injector, a CNG DI injector, was done considering which are the typical pressure values in the rail and in the chamber. The maximum gas pressure inside the rail is close to 15 bar. The in-cylinder pressure could be as high as 100 bar, or more under high engine loads (it must be remembered that with a CNG engine the compression ratio could reach 13). With an inward-opening valve, this negative pressure differential could produce an undesired opening due to the high cylinder pressure. In contrast, an outward-opening valve is naturally sealed by the higher cylinder pressure.

Moreover, the former valve type request an elastic force to counteract the in cylinder pressure. With an outward-opening valve, since a larger pintle lift is allowed, a higher mass flow rate can be produced. Because of these considerations, an outward opening valve was selected [4].

2.5. Numerical model

2.5.1. Discretization and numerical schemes

CFD is the analysis of phenomena such fluid flow, heat transfer and combustion processes using computer-based simulations. In this project, a CFD analysis of a gaseous injection is performed using the software Converge^{TM}.

CFD has its roots in mathematics and fluid mechanics, particularly linear algebra and matrix theory are the most important tools. Many physical problems are modelled by partial differential equations (PDE), in fluid mechanics second order PDEs are of vital importance [20].

In CFD studies, the first step is identifying the mathematical equations that can describe, or produce the best approximation of the physical phenomenon.

Once the PDE to describe the phenomenon has been defined, its discretization is necessary to solve it with computer simulations. Discretization of PDEs can be performed with three methods: Finite difference method (FDM), finite volume method (FVM) and finite element method (FEM).

The software Converge^{TM} can use Finite volume method and Finite difference method to approximate PDE. Finite difference is the first method that was discovered, the first publication about this technique was done in 1910 by L. F. Richardson. Only in 1965, a Scientific American article by Harlow and Fromm clearly and publicly expresses the idea of "computer experiments" for the first time and CFD was born [21].

Finite difference method is simpler and it can reach the convergence faster. The problem is that it requires a fully structured mesh that, up now, is incompatible with curved boundaries. For this reason, finite volume method, which can be applied to an unstructured mesh, is the most used method for industrial flow applications.

With the finite volume method, the domain is discretized in control volumes. The flow properties are stored at the centroid of each control volume. The integral form of the Navier-Stocks equations, expressed in conservative form, are applied to each control volume. The volume integrals, representing conservation equations, are converted to

surface integrals using the Gauss divergence theorem, as shown in the equations (2.9) and (2.10).

$$\frac{\delta}{\delta t}\int_V u\, d\mathrm{V} + \int_V \vec{\nabla}\cdot\vec{F}\, d\mathrm{V} - \int_V S\, dV = 0 \qquad (2.9)$$

$$\frac{\delta}{\delta t}\int_\mathrm{V} u\, d\Omega + \oint_A \vec{F}\cdot\vec{n}\ d\mathrm{S} - \int_A S\, dV = 0 \qquad (2.10)$$

Where u is a generic scalar quantity (e.g. the mass), $\vec{F}$ is the flux of u through the surface A that delimits the volume V and S is the rate of production of u [22]. The flux is defined in equation (2.11).

$$\vec{F} = \rho\vec{v} \qquad (2.11)$$

Where ρ is the density and $\vec{v}$ the velocity of u.

This procedure is applied for each of the elements contained in the control volume.

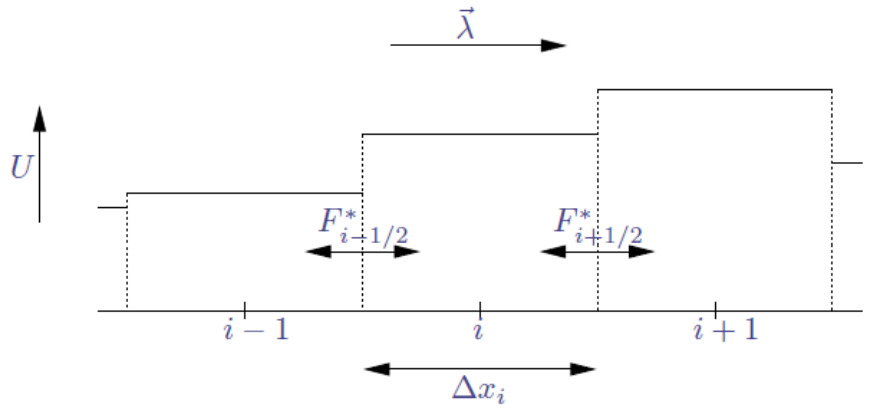

Figure 2.19: 1D representation of a grid scheme for finite volume methods [23]

In order to solve the convective and the diffusion terms, the values of the derivatives at the faces of the control volumes, shown in Figure 2.19, are necessary. In Converge™, this can be done with two methods: central space scheme and upwind scheme. The diffusion term must be central differenced and the convection term can be either central or upwind differenced. The central space scheme is second order accurate and the upwind scheme is first order accurate. Moreover, Converge™ gives the possibility of

differentiate this choice between the momentum equation and the other conservative equations. In this case, the central space scheme is suggested by the manual for both the convective and diffusive terms [24]. For what concerns the time marching, it can be set to be implicit, explicit and Crank-Nicolson. The last one is second order accurate but it is the less stable, the explicit scheme in some cases can be the most stable but, generally, the implicit one is the most stable and so it is suggested by the manual [24].

2.5.2. Meshing

For computer simulations, meshing is one of the biggest issues that must be evaluated. It influences both the accuracy of the results and the computational time. A larger number of points generate better results but the computational time increases. A compromise must be found taking into account the available computational power.

The simulation of CNG DI is a challenging task due to the high pressure ratio present between the rail and the chamber and the wide difference of the physical dimensions between the injector nozzle and the cylinder. The region around the nozzle throat is the most critical domain from the computational point of view, owing to a very high velocity (supersonic) and a very high density gradient in this region [2].

Converge^{TM} uses a hybrid mesh (structured and unstructured) to discretize the space. The overall mesh is structured but, since this mesh is not suitable for curved boundaries, when necessary, it will be unstructured (this is called Cartesian cut-cell method). The main advantage of this mesh is that it can be generated automatically by the software and therefore doesn`t require working time for the user. Moreover, surfaces or cells can be locally refined to better model the geometry or the flow.

Converge^{TM} offers the possibility of defining the basic cell size and of using other tools that can change the mesh locally. These are: grid scaling, adaptive mesh refinement (AMR) and fixed embedding.

The grid scaling option allows changing the cells size by a factor of $1/2^n$ in the entire model. This is useful for a first and coarse evaluation of the results.

The AMR allows the software to change the cell size automatically in relation to some chosen parameters. These can be: the flow velocity, the pressure gradient or the concentration gradient of some defined species.

The embedding feature allows reducing the cell size in a defined region or for a particular surface of a desired level n (this means that the base size will be multiplied by 2^{-n}). This option can be activated or deactivated at each step of the simulation.

As said before, the mesh must be chosen taking into account the available computational power to do not have simulations too long. To have a first idea of a suitable starting point for the mesh, an analysis of what is present in the literature is done. The studied research describes a model for direct injection of CNG, but the software Star-CD is used [6]. Similar cases solved with Converge™ were not found in literature.

The first step was the evaluation of the main cell size. Since the work of Baratta and Rapetto [6] used different software, the meshing method was not the same. Star-CD uses an unstructured hexahedral mesh instead of the hybrid method, used by Converge™. Despite this difference, in this application the base grid size varied between 0.5 and 1.2 mm. These values were obtained by evaluating the overall number cells of the model and the subsequent computational time. However, the maximum height of the pintle lift in [6] was 0.25 mm. This means that, to evaluate the property of the flow, the cell size had to be much smaller close to injector and even smaller inside the nozzle. Moreover, the transition between these two regions was a further critical point. For this reason six refinement levels were used to obtain a smooth transition from the high cell density zone, near the nozzle area, to the relatively coarser grids adopted for the discretization of the combustion chamber. The final result is shown in Figure 2.20.

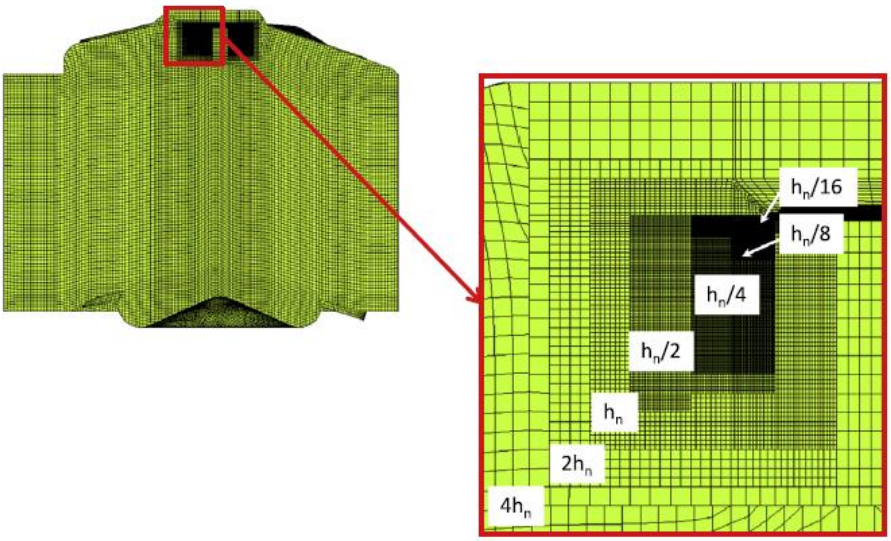

Figure 2.20: Cell size distribution [6]

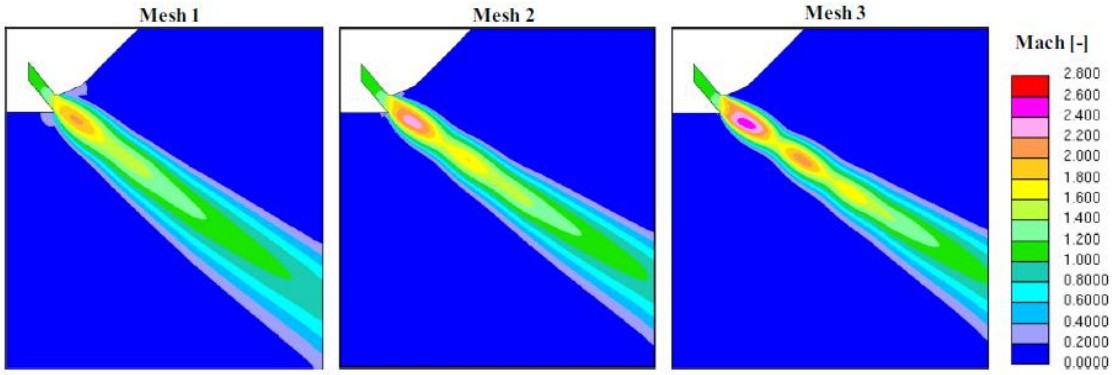

Figure 2.21 Influence of the grid resolution on the Mach number in the supersonic under-expanded region close to the injector exit [6]

In the same research [6], the evaluation of the smallest overall grid size was another critical point and for this reason different cases were analyzed. The grid resolution within the injector seat area was changed while the overall grid architecture in the combustion chamber remained the same. The influence of the grid resolution was analyzed for a part load operation point at 2000 rpm, under stratified charge. Figure 2.21 shows the effect of the grid size on the Mach number in the supersonic region near the injector exit, and their characteristics are reported in the Table 2.4. This figure corresponds to the time instant at 8 CA deg after the start of the injection, when the flow was steady.

	Mesh 1	Mesh 2	Mesh 3
Total number of cells	1,180,000	1,350,000	2,095,000
Cells across the needle lift	8	16	32

Table 2.4: Main characteristics of the considered computational grid [6]

The coarser mesh gives a poor prediction of the Mach number in the under-expanded region. The maximum value is clearly underestimated (Figure 2.22) and just one shock wave is present. The mesh 2 gives a better estimation but only the third mesh is able to show the three shock waves. Also, in the third case the maximum value of the Mach number is higher due to a lower numerical diffusion. Looking at mesh 2 and 3, the difference decreases significantly as the distance from the injector increases.

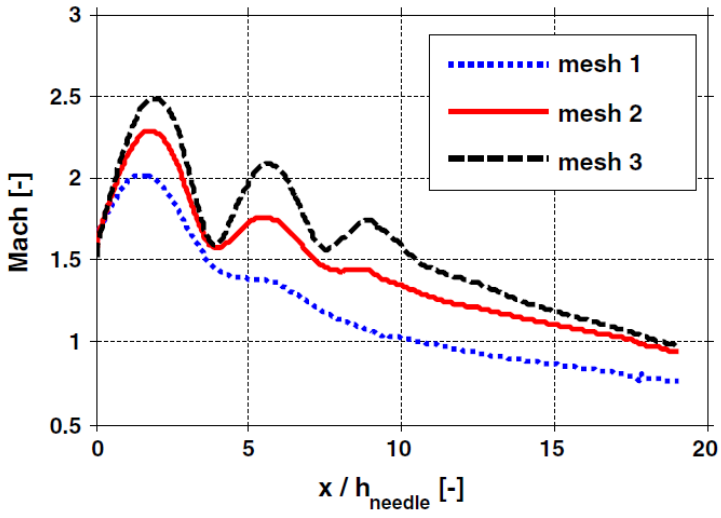

Figure 2.22: Influence of the grid resolution on the computed Mach number. Data collected along the mean jet path [6]

Finally, the results obtained by using the third and the second mesh are similar considering the jet shape, width and penetration. For this reason, the authors of this study [6] considered the second mesh as the best compromise between the computational time and the accuracy of the results [6].

2.5.3. Boundary conditions

Looking at the modelling approach of the injector, simulating the expansion that happens through the nozzle and the region just downstream of it, the idea is to find the solution that gives the most accurate results. The best approach is the one that takes into account the flow of the entire domain, including the region inside the injector. However, this approach is very complicated due to the fine mesh and the long time required to run the simulations. This procedure was used in one of the cases studied [25]. At the beginning of the simulation the pressure was imposed in the entire volume of the nozzle. However, in this way, the pressure wave inside a real injector was not reproduced. This aspect can have negative effects on the mixture formation downstream from the nozzle.

An alternative procedure could be starting the computation of the flow downstream from the Mach disk (the Mach disk is the normal shock located at the end of the supersonic zone). The initial conditions are computed considering a perfect expansion inside a converging-diverging nozzle, the mass flow rate is computed considering an isentropic expansion up to the chamber pressure. The problem is that the initial conditions are not easy to estimate [2].

Another alternative is to treat the flow as formed by droplets. This method is mainly used for liquid fuels but it can be used also with gaseous fuel. The positive aspect is that the grid resolution can be reduced but the amount of necessary input information is even higher than the other cases.

Finally, looking at the analysis performed in another studied research [2], the solution, that seems to give the best results, is the one in which the pressure at the inlet of the injector, so in a chamber upstream of it, was imposed equal to the rail pressure. In this way, the model is able to capture the wave propagation phenomena. In order to achieve this result, also the pintle lift profile is necessary.

2.5.4. Turbulence modelling

Considering the turbulence models, there are many of them and with different levels of complexity and accuracy. The most common are the RANS (Reynolds averaged – Navier Stokes) models that can be divided in: zero-equation, one-equation, two-equation and seven-equation models. The first two are relatively simple but the results may not be accurate enough for many applications. The most common are the two-equation models that again can be divided in: k-ε style models, k-ω style models and ASM model. In Converge^{TM}, between the RANS ones, three different k-ε models can be chosen: standard k-ε, RNG k-ε and rapid distortion RNG k-ε. All these three are based on two equations; one for the turbulent kinetic energy (k) and another for its dissipation (ε). The second and the third models derive from the first one. They include additional term in the ε equation for interaction between turbulence dissipation and mean shear, the effect of swirl on turbulence and some other improvements. The RNG model performance was evaluated in many applications. For example with a direct injection diesel engine it was found that considerable improvements are present with respect to the standard k-ε model in spray and combustion calculations due to the high strain rates associated with spray-generated turbulence [26]. In the next chapter, a comparison of the results obtained with the standard k-ε and RNG k-ε is done to understand which one can give better results.

2.6. X-Ray radiography

As mentioned in the objectives, the injector model, that is going to be used, is validated using to the experimental data coming from X-ray radiography. For this reason, it is worthwhile to understand how this technique works.

X-ray radiography is an imaging technique that uses electromagnetic radiation other than visible light, in particular X-rays, to view the internal structure of a non-uniformly composed and opaque object (i.e. a non-transparent or partially transparent object of varying density and composition). To create the image, a heterogeneous beam of X-rays is produced by an X-ray generator and is projected toward the object, in this case across the chamber in which the gas is injected. A certain amount of X-ray is absorbed by the

object; this is dependent on the particular density and composition of that object. The X-rays, which pass through the object, are captured behind the object by a detector (either photographic film or a digital detector). The detector can then provide a superimposed 2D representation of all the internal objects.

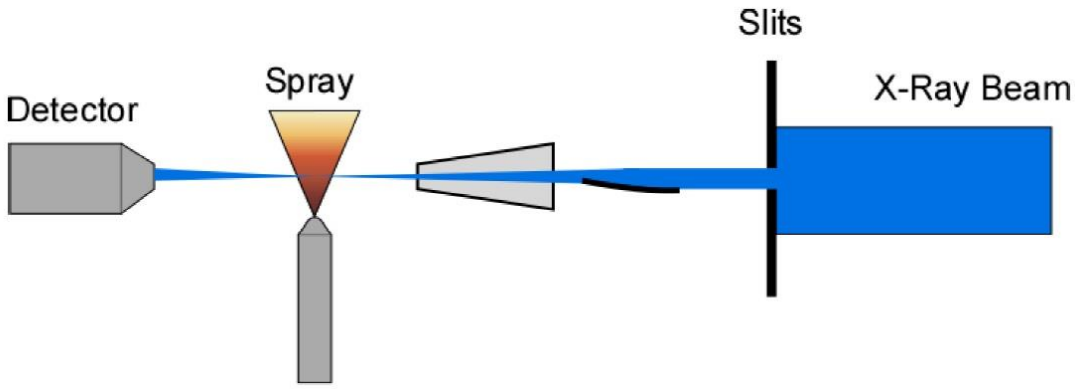

Figure 2.23: X-ray radiography apparatus scheme [27]

Most X-rays have a wavelength ranging from 0.01 to 10 nanometers, corresponding to frequencies in the range 30 petahertz to 30 exahertz (30×10^{15} Hz to 30×10^{18} Hz) and energies in the range 100 eV to 100 keV. X-ray wavelengths are shorter than those of UV rays and typically longer than those of gamma rays. X-rays with photon energies above 5–10 keV are called hard X-rays, while those with lower energy are called soft X-rays. Hard X-rays can traverse relatively thick objects without being much absorbed or scattered. For this reason, X-rays are widely used to image the inside of visually opaque objects [28].

In this application, the object that must be captured by the X-ray is a gas and for this reason, the absorption is much lower. In particular, using CNG (or methane) the absorption is lower than 0.5% and so the detector is not able to capture very well the shape of the jet. Using argon, this issue can be solved because its absorption is close to 3% [27]. The higher absorption is mainly related to the higher density; methane has a density of 0.66 Kg/m^3, argon has a density of 1.66 $kg/m^{3,}$ at ambient conditions. Moreover, the chamber is filled with nitrogen to have a constant absorption that is clearly

different with respect to argon absorption. The density of nitrogen is equal to 1.165 Kg/m^3, in ambient conditions.

Nitrogen is used, instead of air, because the presence of oxygen in air (oxygen density is equal to 1.331 Kg/m^3) can influence the absorption and alter the results.

3. METHODOLOGIES AND PROCEDURES

3.1. Model setup

As mentioned in the objectives, the first part of the project is focused on the development of a model that is able to describe the behavior of a real injector designed for the application on a DI CNG engine.

The work starts with the setup of the proper geometry and then continues with the definition of all the parameters that must be defined in a 3D CFD simulation and, more in particular, in Converge^{TM}.
The injector, used in this project, is a DI-CNG injector procured by FCA from a major Tier 1 supplier.

3.1.1. Cases for the model validation

In both the experiments and the CFD model, the described injector is mounted on the top of a constant volume chamber. This chamber has two optical accesses from two sides. In this way, thanks to the X-ray radiography described previously, it is possible to capture the argon jet that is injected in a nitrogen environment.
The experiments and the simulations are performed in two different conditions; they are described in Table 3.1. The results of the simulations are compared with the experimental data to validate the model. The data are organized in plots showing the path length at different positions in the chamber. The characteristics of this parameter are explained later in this chapter.
The penetration and the mass flow rate with respect to time are also evaluated.

Rail pressure	Chamber pressure	Injection duration	Wall impingement
10 bar	1 bar	1.2 ms	none
10 bar	1 bar	1.2 ms	19 mm

Table 3.1: Conditions in which the experiments and the simulations were performed

Moreover, other simulations are performed to evaluate the effect of some parameters on the jet shape. The cases are summarized in Table 3.2. Two rail pressures are considered: 15 bar and 10 bar. In one case, the chamber pressure is increased up to 2 bar. Moreover, in another case (also considered in Table 3.1), a wall is positioned in front of the injector to evaluate also the impingement of the jet.
The penetration and the mass flow rate with respect to time are also evaluated.

Rail Pressure	Chamber pressure	Injection duration	Wall impingement
10 bar	2 bar	1.2 ms	none
15 bar	1 bar	1.2 ms	none
15 bar	1 bar	1.2 ms	19 mm

Table 3.2: Conditions in which other simulations were performed

3.1.2. Mixture formation

After the model validation, an analysis of the mixture formation is performed. In particular, injecting the fuel in different working conditions, the effects of some parameters on the mixture formation is evaluated. Six cases are analyzed; these are listed in Table 3.3. In this part of the project, argon is substituted by methane. The reason is that CNG is mainly composed by CH4 (close to 95%) and so their characteristics are very similar.

The pressures of the rail and of the chamber are fixed. The dimension of the chamber is fixed, it is a cubic box with sides of 30 mm. In three cases the injector is positioned in the middle of a face, in the other three cases it is positioned close to one side wall to evaluate the effect of the injector position on the mixture formation.
Moreover, also the influence of the turbulence is evaluated. In real engines, a large flow motion is created during the intake. When the intake valves close and the piston starts compressing the gas, the turbulence starts dissipating. In this analysis a zero mean velocity of the flow is considered, but some values of turbulence kinetic energy are imposed at the beginning of the process. First of all, the chamber is considered full of "calm" air and so the initial turbulent kinetic energy is imposed equal to $1.0\ m^2/s^2$.

After, other two values are chosen starting from the analysis done in the literature. They are two typical values that can be found during the intake, with two different pistons geometry. The turbulence length scale is chosen again looking at what was observed in literature: it is equal to $0.2\ mm$ in both cases. The turbulence dissipation rate is computed as described in the previous chapter and it is imposed as initial condition.

Rail Pressure [bar]	Chamber pressure [bar]	Turbulent kinetic energy [m^2/s^2]	Turbulence dissipation rate [m^2/s^3]	Injector distance from the side wall [mm]
10	1	1.0	10.0	15
10	1	1.0	10.0	6
10	1	73.5	7043	15
10	1	73.5	7043	6
10	1	216	12075	15
10	1	216	12075	6

Table 3.3: Studied cases to evaluate the mixture formation

In these conditions, the idea is to obtain a stoichiometric mixture in the largest possible number of cells. For this reason, starting from the box volume a precise amount of fuel is injected in the chamber.

$$V_{chamber} = 0.000027\ m^3 \tag{3.1}$$

$$m_{Air} = \rho_{Air} V_{chamber} = 0.03124\ g \tag{3.2}$$

The mass of air present in the chamber is computed considering the air density at 300 K, it is equal to $1.157\ \mathrm{kg/m^3}$. Since the stoichiometric air fuel ratio for CNG is 17.2, 1.816 mg is injected. The injection duration is evaluated considering the mass flow rate computed by Converge^{TM} in a first trial simulation, done using methane.

3.2. Computational matrix

3.2.1. Geometry

Figure 3.1 shows the CAD geometry of the injector tip provided by FCA. This tip reproduces the real nozzle shape of the injector described before.

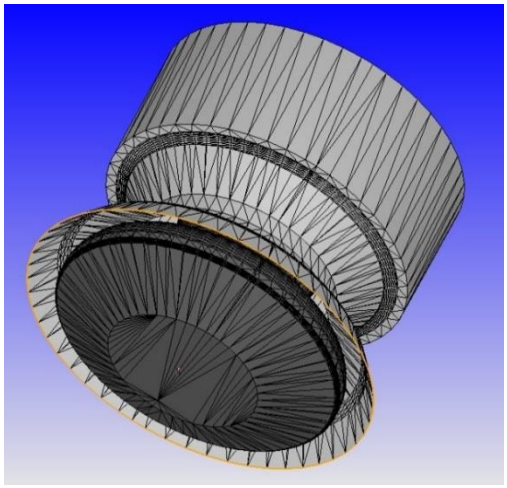

Figure 3.1: CAD model of the injector tip (fully open)

As in the experiments, the tip geometry is positioned on the top of a constant volume chamber. The chamber is realized in two different ways to meet the conditions described in Table 3.1. In one case, without wall impingement, the chamber has an outlet at its bottom. The size of this chamber is 30 mm x 30 mm x 30 mm. In the other case, the chamber is completely closed and it has a wall positioned 19 mm far from the injector. Moreover, this chamber is also wider (70mm) to avoid the impact of the spray against the lateral walls. This would affect the path length and, for this reason, the simulation is stopped before that the flow reaches the side walls. This aspect will be clear when the meaning of path length will be explained. Figure 3.2 shows the geometry of the model for the two cases.

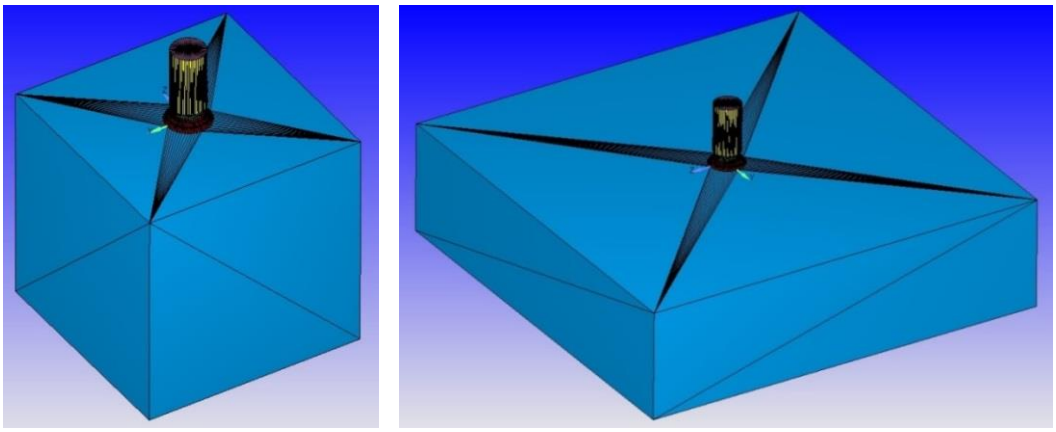

Figure 3.2: On the left, the geometry of the model without impingement. On the right, the geometry of the model with a wall in front of the injector

In the analysis of the mixture formation, only the square chamber is used and it is closed to keep all the fuel inside. Then, in three cases the injector is positioned close to one side wall, as described before. Figure 3.3 shows the geometry of the chamber with a central injector and with an off-center injector.

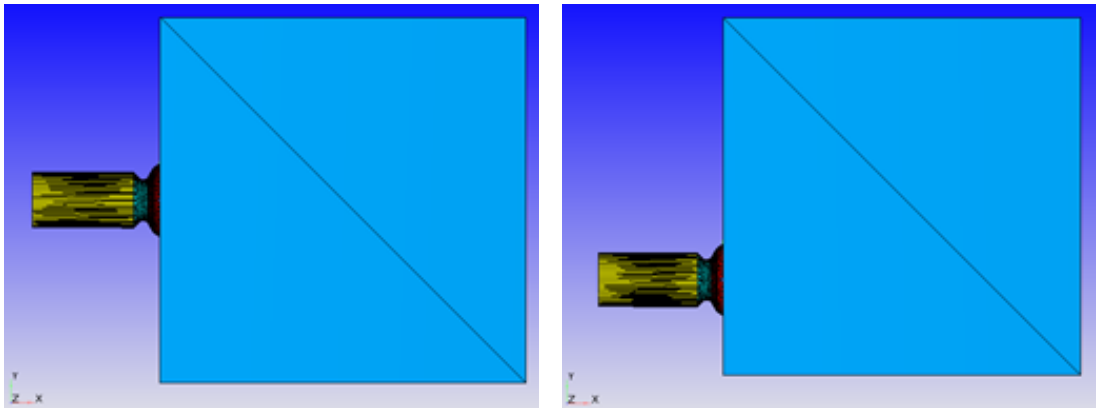

Figure 3.3: Chamber geometry used for the mixture formation. On the left with a central injector. On the right with a off-center injector

3.2.2. Pintle lift profile

From the first simulations, it was noticed that an instantaneous opening of the injector produces a faster penetration of the jet with respect to the experimental one. For this reason, to obtain more accurate results, it was decided to simulate also the pintle movement.

The real equation of the lift profile was not available and, for this reason, some simulations were performed to obtain the most accurate penetration. During these simulations it was noticed that a too gentle initial ramp of the opening retarded or eliminated the collapsing of the flow toward the center. A too strong initial ramp of the opening produced a crash of the simulation. The extremities of the profile are taken considering the measured mass flow rate. The maximum lift is measured in the geometry of the injector fully open. The normalized pintle opening equation is plotted in Figure 3.4.

All the results shown in this thesis, both for the model validation and for the study of the mixture formation, are obtained using this opening profile.

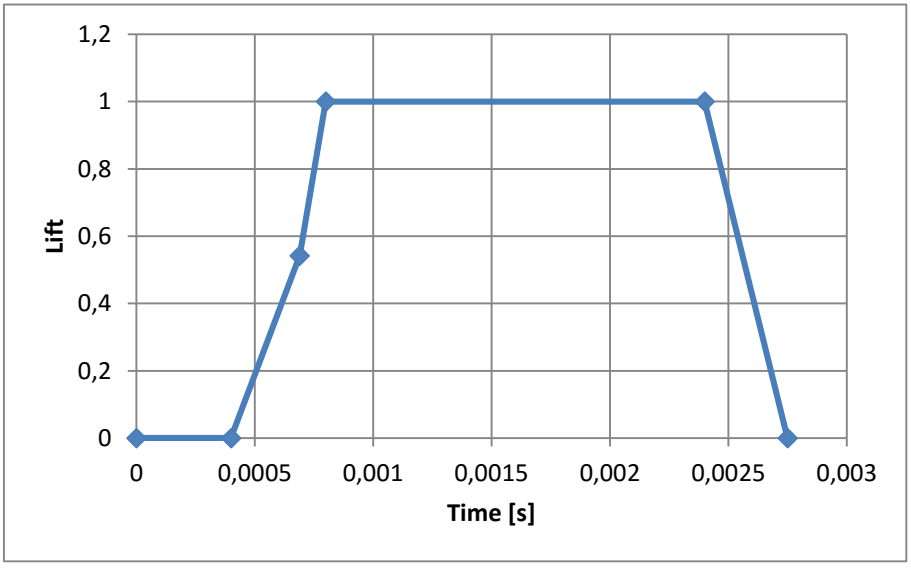

Figure 3.4: Normalized pintle lift profile

3.2.3. Boundary conditions

After the definition of the geometry, the next step is the setup of the inlet boundary condition. Two possibilities are available; the mass flow rate or the pressure could be fixed. Since the former can be measured during the experiments, the first simulations are carried out imposing it. However, this strategy was abandoned because the cell size, in the region of the injector, has to be too small to avoid the crash of the simulation. As a consequence of this, the cell number would be too high, up to 5 million with the described geometry, and the time step as small as to 10^{-9} second for stability reasons.

The second strategy, with the pressure imposed in the inlet, has been implemented in this research. For this reason, a small chamber is built upstream from the nozzle. Inside this chamber, a constant pressure is imposed and the gas (argon or methane) enters from the inlet at the same pressure. Figure 3.5 shows in yellow the external walls of the pressurized chamber and in fuchsia the inlet of the injector.

However, since the tip pressure of the real injector is not known, the boundary pressure is setup considering the measured mass flow rate. More in particular, some preliminary simulations are carried out to tune the inlet pressure. The aim of the tuning is to obtain in the simulations the same mass flow rate of the real injector in steady state conditions. In order to have a first idea of the pressure value that could be necessary, the equation (2.4) for a choked flow is used. The throat area is measured manually on the geometry. The discharge coefficient is evaluated considering the mass flow rate computed by Converge^{TM} during a first simulation.

For example, with a rail pressure of 10 bar, the inlet pressure in the model must be equal to 5.4 bar to have the same mass flow rate. When the rail pressure is equal to 15 bar, for the same reason, 8.3 bar is imposed at the inlet of the model.

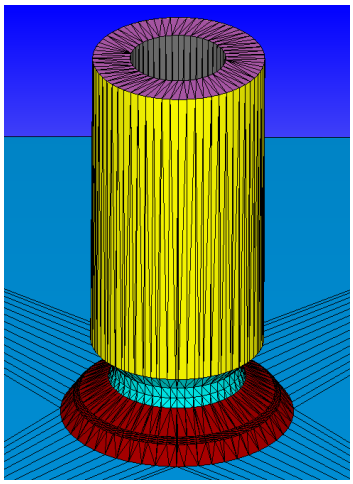

Figure 3.5: Partial section of the pressurized chamber upstream of the nozzle

Looking at the case in which the chamber is open, to avoid the impingement of the flow, a zero normal gradient for pressure and velocity is imposed at the bottom outlet. In the case in which a wall is placed in front of the injector, at this numerical boundary a zero normal gradient for the turbulent kinetic energy is imposed.

3.2.4. Mesh definition

The base mesh size is defined considering what was found in literature. For this work, two alternatives are evaluated. In one case, the base cell size is equal to 1 mm; in the other, it is equal to 0.9 mm. The main differences are summarized in Table 3.4.

Base cell size	Total number of cells	Smallest cell size	Number of cells along the pintle opening	Maximum Mach number	Time to simulate 1 ms
0.9 mm	2.2 million	0.028125 mm	11	2.425	46 hours
1 mm	1.6 million	0.03125 mm	10	2.423	33 hours

Table 3.4: Effect of the base cell size on the total number of cells, on smallest cell size, on the number of cells along the pintle opening, on the maximum Mach number and on the time to simulate 1 ms

Even if the difference in the base cell size is small, the overall number of cells changes a lot. As a consequence, the time of the simulation also changes a lot. The time indicated in the right column refers to simulations performed with 24 cores.

However, since the difference in the cells size, both considering the base and the smallest, is very small, the difference in the results is also very small.

For example, the maximum value of the Mach number is a bit higher when the cell is smaller but the difference is negligible. Looking at the mass flow rate, shown in Figure 3.6, again the difference between the two cases is very small. Finally, the base cell size of 1 mm is chosen. For the sake of clarity, these results are obtained using four embedding levels. The level 5 is used inside the injector, the level 4 is used just downstream of it, the level 3 and 2 are positioned in the chamber to capture better the shape of the jet. In this case the adaptive mesh refinement is not used. This aspect will be explained better later.

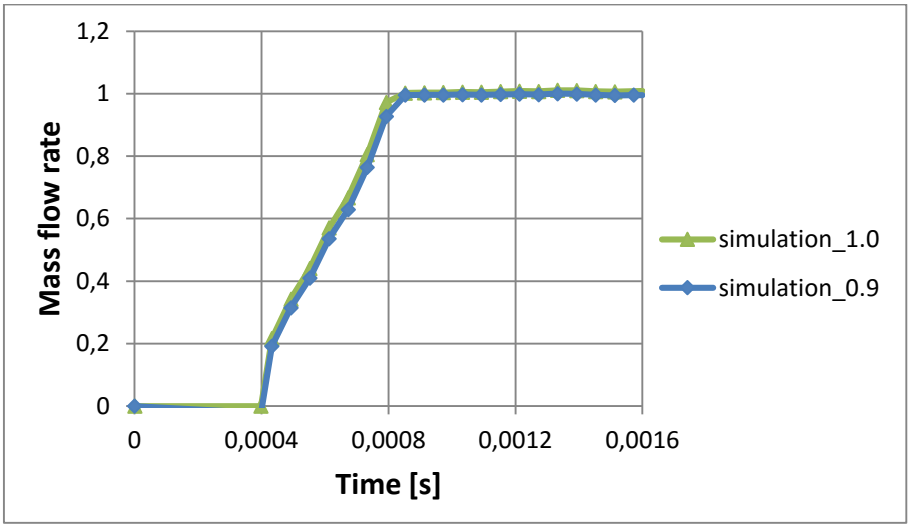

Figure 3.6: Normalized mass flow rate during the pintle opening and at steady state with a base cell size of 0.9 mm and 1 mm

However, as mentioned in literature review, a much smaller mesh is necessary close to the injector to have a good description of the expansion. In order to do so, a fixed embedding can be used close and inside the injector. In particular, three combinations of embedding are compared. These are shown in Figure 3.7. In the first case, only the level 4 is used in the injector region; in the second, the level 5 is implemented. In the third, the

two levels are combined: the level 5 is used inside the injector and the level 4 just downstream of it.

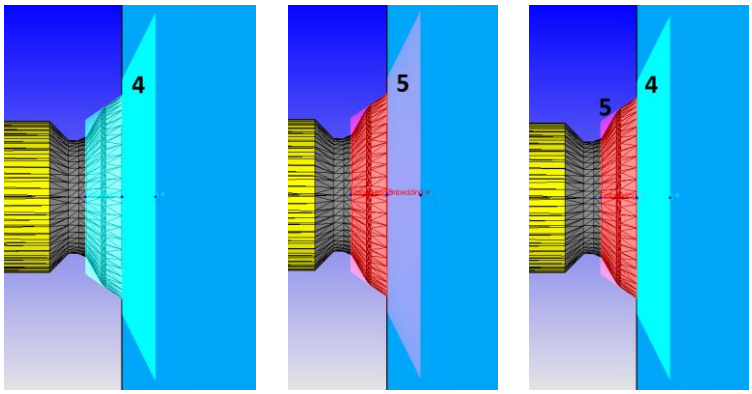

Figure 3.7: Embedding levels comparison. From left to right: level 4, level 5 and combination of them

As a reminder, with the level 5 the base size of the cell is divided by 2^5, with the level 4 it is divided by 2^4. A comparison of the results obtained in the three cases is reported in Figure 3.8 and Figure 3.9. Just for the sake of clarity, in this case also the adaptive mesh refinement is used. The reason of this choice will be explained later.

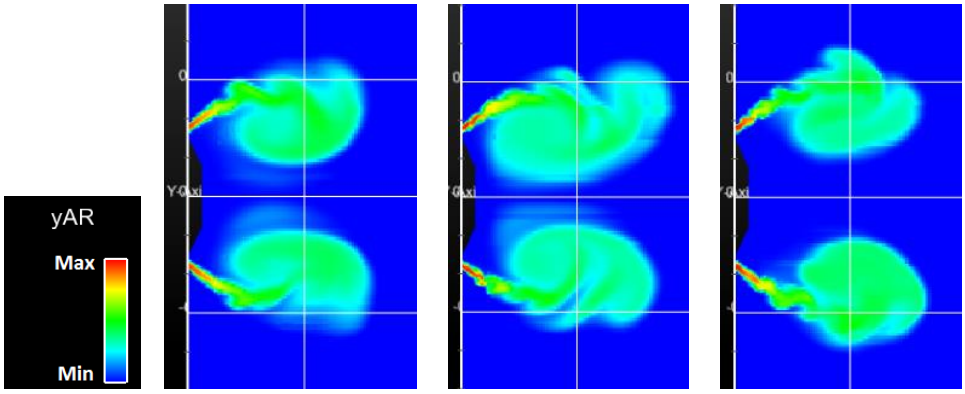

Figure 3.8: Argon mass fraction with three embedding levels. From left to right: level 4, level 5 and combination of them

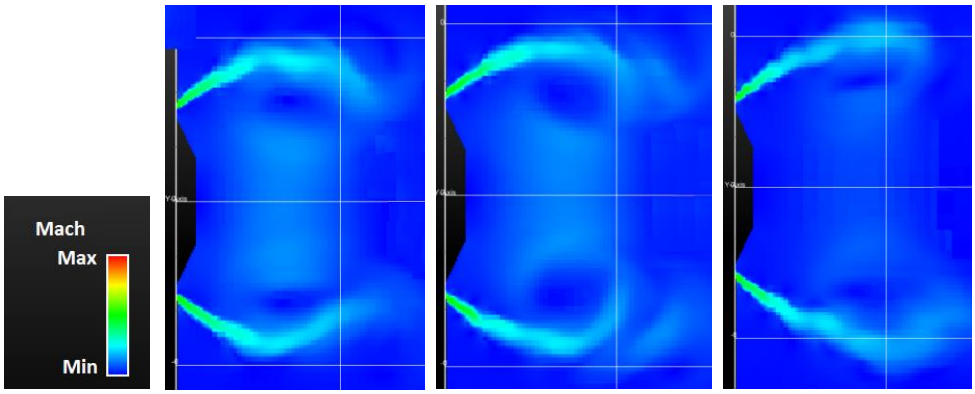

Figure 3.9: Mach number with three embedding levels. From left to right: level 4, level 5 and combination of them

The same comparison is done looking at the mass flow rate (Figure 3.10) and at the penetration (Figure 3.11).

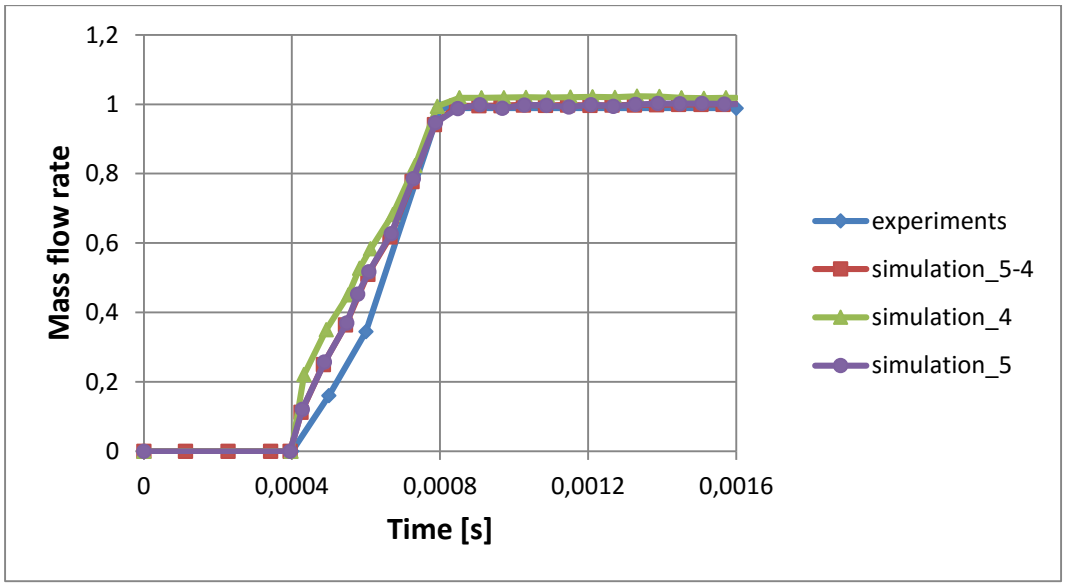

Figure 3.10: Normalized mass flow rate with respect to time for the experimental results and three embedding distributions: Level 4, Level 5 and a combination of them

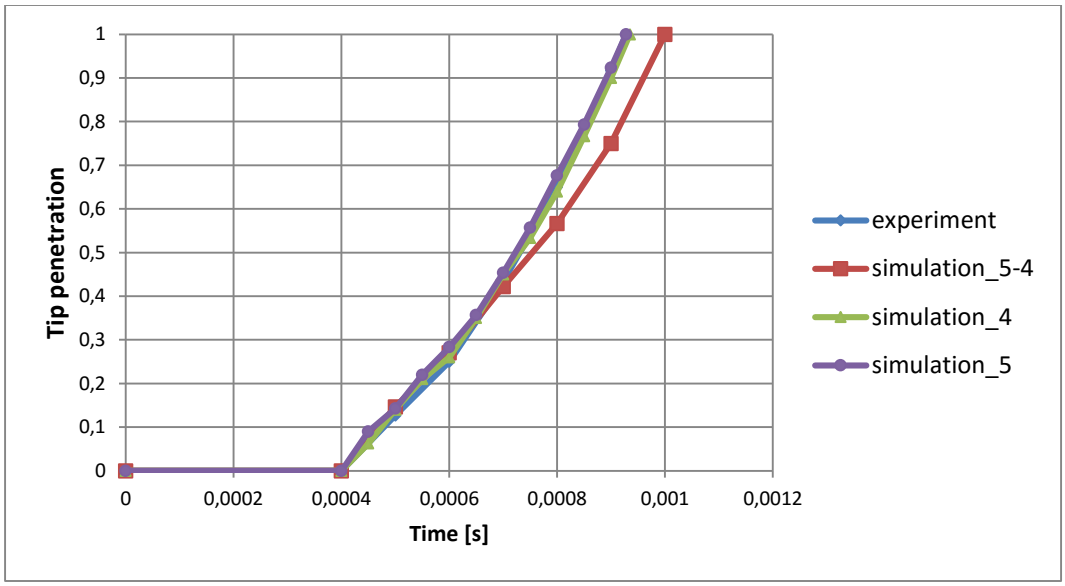

Figure 3.11: Normalized tip penetration with respect to time for the experimental results and three embedding distributions: Level 4, Level 5 and a combination of them

Furthermore, other important characteristics are shown in Table 3.5.

Embedding level	Number of cells	Smallest cell size	Number of cells along the pintle opening	Time to simulate 1 ms
5 - 4	0.73 - 2.1 million	0.03125 mm	10	51 hours
5	2.4 – 3.5 million	0.03125 mm	10	100 hours
4	0.451 – 1.48 million	0.0625 mm	5	17 hours

Table 3.5: Embedding level, number of cells, smallest cell size and time to simulate 1 ms for three embedding distributions: Level 4, Level 5 and a combination of them

In conclusion, looking at the argon mass fraction and at the Mach number, the biggest difference is visible when both levels 5 and 4 are combined. In this case, the flow is converging slower toward the center; this also produces a slower penetration as can be seen in Figure 3.11. Moreover, the level 4 is overestimating the mass flow rate in steady state conditions but the error is very small.

Using the level 5, the best results are obtained but the duration of a simulation is much longer than the other two cases. A combination of the two levels is not suggested due to

the lower penetration. The level 4 is producing good results and the time to run a simulation is much shorter than the other two cases.

Moreover, the adaptive mesh refinement (AMR) with a level three is used to capture better the flow shape in the region far from the injector. The AMR is based on the velocity gradient of the flow and on the concentration gradient of argon/CNG.
Using AMR, the number of cells is not constant during the simulation but this tool allows getting better results because the cell distribution is optimized. Figure 3.12 shows how the cells distribution looks like during the injection.

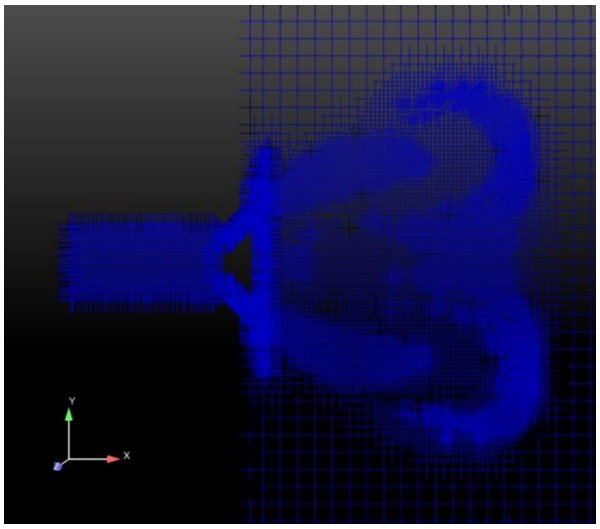

Figure 3.12: Cells distribution using the adaptive mesh refinement

Adding the AMR, the computational time becomes a bit longer. This happens because, even if the overall number of cells can be lower, the mesh grid is ricalculated at each time step to be adequated to the flow shape.
In order to reduce the computational time, the AMR could be also avoided creating a cylindrical fixed embedding at the exit of the nozzle. This approach was used to evaluate the effect of the base cell size described at the beginning of the section.
However, during the analysis of the mixture formation, the gas is moving in the entire chamber and for this reason having the AMR is a big advantage.
Finally, the AMR is used in all phases of this study.

3.2.5. Turbulence model

The choice of the turbulence model in Converge^{TM}, for this kind of application, is mainly between the standard k-ε and the RNG k-ε models.

Considering what is reported in the literature, RNG is more suited for engine application. It produces better results especially looking at the injection and compression process.

For the project, a quick comparison between them is done to see which model is describing better the injection process. After a quick observation of the results, the standard k-ε seems to produce a smoother and more regular jet. On the contrary, the RNG k-ε is able of capturing better the structures of the flow (Figure 3.13).

Moreover, looking at the jet penetration, with the RNG k-ε model the gas is propagating faster in the chamber. Comparing the simulated penetration with the tested one, RNG produces more accurate results.

If the penetration is faster, the jet is also collapsing faster toward the center. Also in this case, looking at the experimental measurements, the RNG is offering better results.

These last considerations, added to what was shown in literature, guides the choice of the turbulence model to be the RNG k-ε model.

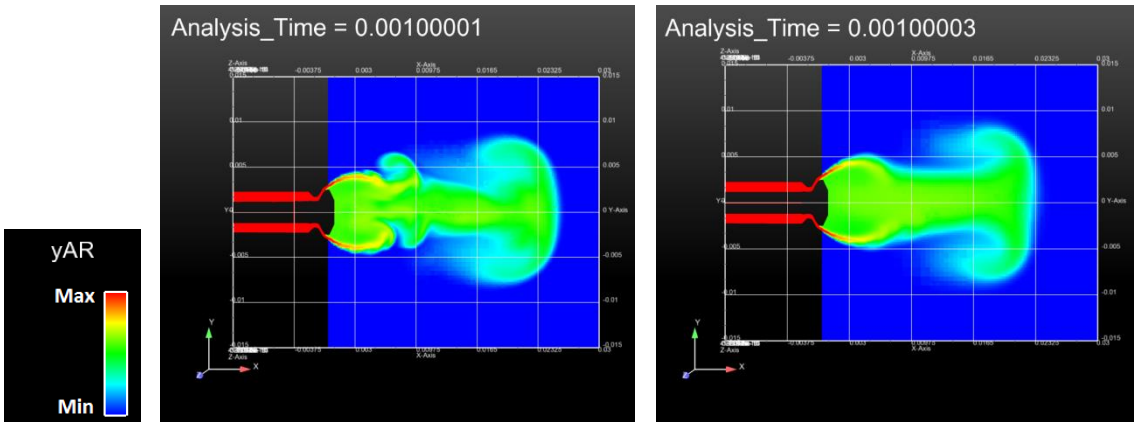

Figure 3.13: Comparison between the results obtained with RNG k-ε (on the left) and with standard k-ε (on the right)

3.2.6. Schmidt number

The Schmidt number is defined as the ratio between the kinematic viscosity and the mass diffusion rate, as shown in equation (3.3). It is used to characterize fluid flows in which there are simultaneous momentum and mass diffusion convection processes.

$$S_c = \frac{\nu}{D} = \frac{\mu}{\rho D} \tag{3.3}$$

For argon, the kinematic viscosity is equal to $1.2434\ 10^{-5} m^2/s$. The mass diffusion rate depends on both the argon and nitrogen properties and it is quite difficult to compute. In this case, it is evaluated using the Gilliland equation (3.4) [29]. This method offers an approximate result with an error generally lower than 20%.

$$D = \frac{0.0043 T^{1.5} \sqrt{\frac{1}{M_{Ar}} + \frac{1}{M_{N2}}}}{P\left({V_{Ar}}^{1/3} + {V_{N2}}^{1/3}\right)^2} \tag{3.4}$$

In this equation, M_{Ar} and M_{N2} are the atomic weight and V_{Ar} and V_{N2} are the molecular volume of argon and nitrogen. Finally, the mass diffusion results equal to $2.09939\ 10^{-5} m^2/s$ and the Schmidt number equal to 0.58.

The same consideration is done using methane and air, their Schmidt number is 0.78.

3.3. Data post-processing

3.3.1. Comparison between simulation results and experimental data

As told before, the described model must be validated with experimental data. They were obtained using the X-ray technique described in the literature review. From that description, it is clear that the data are represented in a plane and so they are 2D.

The model realized with Converge™ is 3D and it is going to provide 3D results. For example, the software can compute the value of all the requested properties in each cell of the domain.

Therefore, the comparison of the experimental 2D results with the simulated 3D is an issue.

For example, with a clip plane, it is possible to show the values of the variables on a precise plane (like in Figure 3.13). However, the values of this plane cannot be compared with the experimental results because the latter are obtained considering the entire control volume and not only one plane.

Moreover, due to the technique used to measure the amount of argon in the chamber during the experiments, the tested results come in the form of projected density and path length. The first one is related to the amount of fuel that the X-ray is encountering going across the chamber and to the surface area of the beam, for this reason it is computed in kg/m^2. The path length is also describing the amount of argon that the beam is encountering but in meters. More in particular, it is equal to the projected density over the density of nitrogen in ambient conditions. ρ_{N2} is assumed to be equal to 1.6 kg/m^3.

Starting from the results of the simulations, the projected density and the path length are computed with the software Ensight. The procedure is described in the next pages.

As can be seen from Figure 3.14, first a grid plane is created on one side of the control volume. Then, from each cell of the grid plane, a grid line goes across the control volume. At this point, three important considerations must be done:

- The grid plane can be established arbitrarily and it is not related to the mesh.
- The same is valid for the grid line.
- The values of the variables in a grid cell, on each grid line, are equal to their values in closest mesh cell. If more mesh cells are contained in a grid cell the average value is computed.

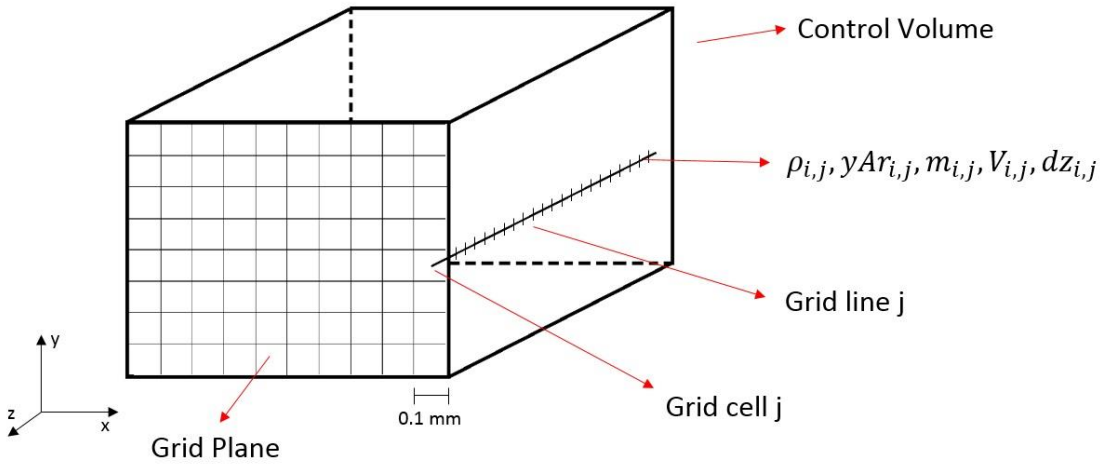

Figure 3.14: Control volume, grid plane and grid line used to compute the projected density and the path length

Since the size of the mesh cells is not constant, the mass of argon in each cell does not depend only on the distribution of the gas but also on the size of the mesh cells. For this reason, these values cannot be used with the grid line and with the grid cells that have a constant size.

For obvious reason, the same issue is not present using density and mass fraction of argon; they are already taking into account the volume of the cells.

After these considerations, the projected density is computed with equation (3.6).

$$m_{Ar\ grid\ i,j} = \rho_{i,j}\ yAr_{i,j}\ V_{grid\ i,j} = \rho_{i,j}\ yAr_{i,j}\ Area_{i,j} dz_{i,j} \qquad (3.5)$$

$$Pd_j = \sum_i \frac{m_{Ar\ grid\ i,j}}{Area_{i,j}} = \sum_i \rho_{i,j}\ yAr_{i,j}\ dz_{i,j} \qquad (3.6)$$

Where: $m_{Ar\ grid\ i,j}$ is the mass of argon in the grid cell "i,j" and Pd_j is the projected density computed on the grid line "j".

The summation obtained in each grid line is stored in the corresponding cell of the grid plane. The grid line is moved along the entire plane in such a way to cover the entire volume.

In the same way, the path length is computed using equation (3.7).

$$Pl_j = \frac{Pd_j}{\rho_{N2}} = \sum_i \frac{\rho_{i,j}\, yAr_{i,j}\, dz_{i,j}}{\rho_{N2}} \tag{3.7}$$

Pl_j is the path length computed in meters.

Even in this case, the result coming from the summation is stored in the corresponding cell of the grid plane. In this way, the 3D results are converted in 2D.

Figure 3.15 can explain better the procedure when applied to a jet. On the left, a scheme of a generic conical jet is shown, the black circle on the right represents the right view of the jet, the red dashed arrow reproduces the grid line, described before, and the grey line represents the grid plane. The path length is computed integrating, as explained before, along the red arrow and storing the result in the grey plane. The red arrow moves on the entire grid plane to cover the entire chamber volume.

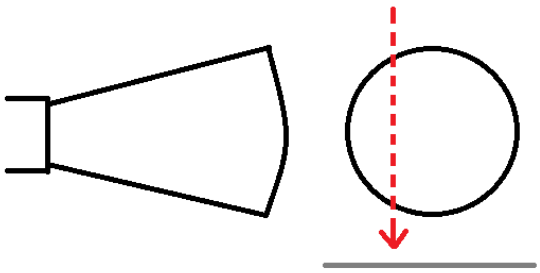

Figure 3.15: Scheme of a jet and of the integration grid line

3.3.2. Evaluation of the mixture quality

From the description just done, it is clear that the path length is adequate to compare the simulations with the experiments but not to study the mixture formation.

For this reason, the latter is evaluated considering the equivalence ratio in each cell. The equivalence ratio is the ratio between the stoichiometric and the actual air fuel ratio. Some intervals for the equivalence ratio are defined, as shown in Table 3.6.

Each cell of the volume is classified considering the listed intervals. At the end, the cells volume of each interval is summed to evaluate the percentage of volume in each condition. The results are summarized in plots.
This procedure is followed for all the cases, listed in Table 3.3, in such a way to evaluate the effect of the mentioned parameters on the mixture quality.

	Fuel mass fraction %	Equivalence ratio	Air fuel ratio
Lean – not flammable	$0 < y_{CH4} < 2.33$	$0 < \phi < 0.409$	$\infty < AFR < 42$
Lean flammable	$2.33 < y_{CH4} < 5.24$	$0.409 < \phi < 0.95$	$42 < AFR < 18.1$
Stoichiometric	$5.24 < y_{CH4} < 5.75$	$0.95 < \phi < 1.05$	$18.1 < AFR < 16.4$
Rich - flammable	$5.75 < y_{CH4} < 8.16$	$1.05 < \phi < 1.527$	$16.4 < AFR < 11.26$
Rich – not flammable	$8.16 < y_{CH4} < 100$	$1.527 < \phi < \infty$	$11.26 < AFR < 0$

Table 3.6: Intervals used to evaluate the mixture quality [30]

With Converge™, the equivalence ratio can be computed only if the combustion model is activated. Since this project is studying only the injection process, it is necessary to find an alternative method to evaluate it. This can be done using the software Ensight with the following commands.

*Lean_not_flammable = Volume*IF_GT(yCH4,0)*IF_LT(yCH4,0.0233)*

Lean_not_sum = udmf(region1,Lean_not_flammable)

The first command is necessary to classify each cell; the second is used to compute the overall volume in each interval. The functions used are:

- *IF_lt(a,b)* that gives 1 if *a<b*
- *IF_GT(a,b)* that gives 1 if *a>b*
- *udmf(a,b)* computes the sum of the variable *b* in the region *a*.

4. RESULTS ON MODEL VALIDATION

This chapter shows the results of the first phase of the work. The obtained values are compared with the experimental data provided by FCA to validate the model.
The validation is divided mainly in two parts: steady state validation and transient validation.

4.1. Structure of the jet

Before starting the model validation, it is worth to make a preliminary description of the jet structure. It is useful to have a better understanding of the next plots which show the path length. The explanation is already based on what was obtained in the simulations.

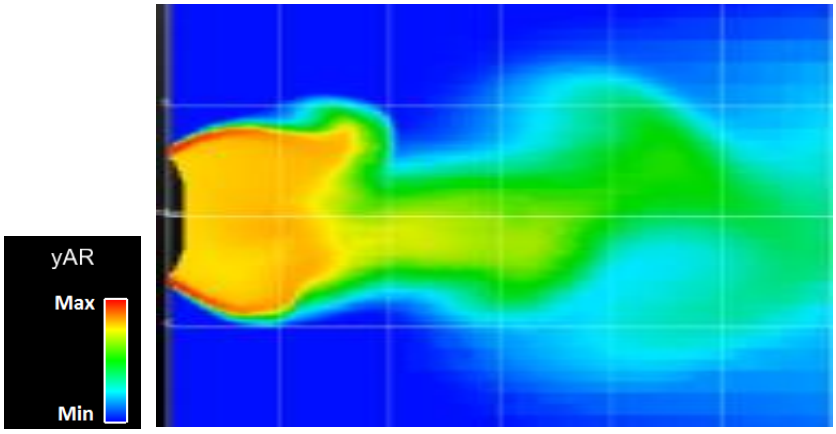

Figure 4.1: Mass fraction of argon in the middle plane of the chamber

Analyzing Figure 4.1, that shows the mass fraction of argon in the middle plane in steady state conditions, some conclusions can be drawn:

- The gas is filling the entire region downstream of the injector, creating a solid jet.
- The injector is creating two tails of gas (red region) from the sides of the pintle.
- Looking at the jet from the right, the two tails are creating a ring with a higher concentration of gas.

4.2. Steady state results

The injection in steady state conditions, so when the pintle is fully open and the flow is completely developed in the chamber, is analyzed looking at the path length described before. It is evaluated along five different lines positioned at a defined distance from the injector. For the reference system chosen, the lines are going to be orthogonal to the x axis and parallel to the y axis. Their positions with respect to the jet are shown in Figure 4.2.

Just for the sake of clarity, the time instant 1.2 ms after the start of the injection is chosen. However, since the process is steady, the time is not a relevant parameter for the results.

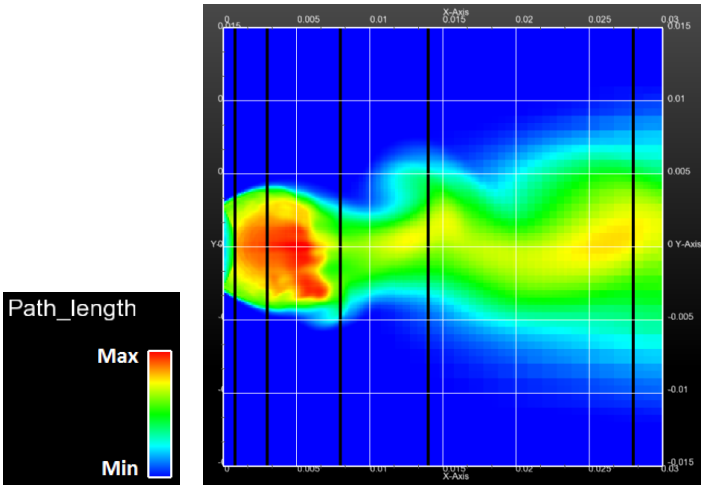

Figure 4.2: Position of the lines used to plot the path length, open chamber

In the first case, in which the chamber is open at the bottom, the lines are positioned at:

- $x = 0.8\,mm$
- $x = 3\,mm$
- $x = 8\,mm$
- $x = 14\,mm$
- $x = 28\,mm$

In the second case, the chamber is closed at the bottom. This wall is 19 mm far from the injector. The lines are positioned at:

- $x = 0.8\ mm$
- $x = 3.5\ mm$
- $x = 8\ mm$
- $x = 14\ mm$
- $x = 19\ mm$

Also in this case, Figure 4.3 shows the position of the lines with respect to the jet. The fifth line is not visible because it is overlapping the wall on the right. These particular values of *x* are chosen considering the values used in the simulations.

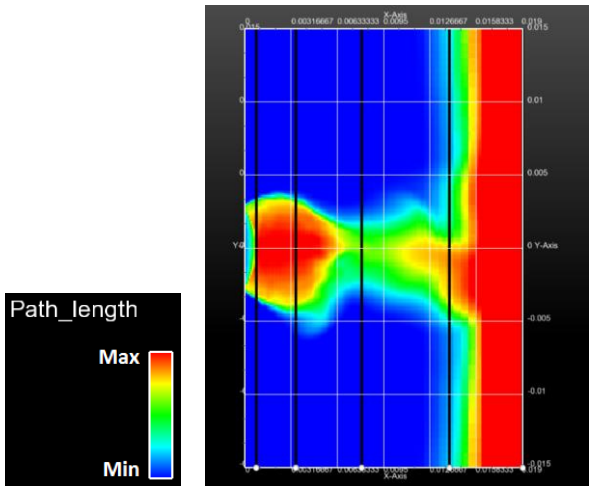

Figure 4.3: Position of the lines used to plot the path length, closed chamber

Before starting the analysis, it is important to clarify that the experimental measurements are obtained averaging a large number of injection events. For this reason, the curves of the path length are always quite smooth and symmetric.

The results coming from the simulations are obtained averaging four time instants in steady state conditions. In some cases, this is not enough to obtain a symmetric and smooth curve. In conclusion, any asymmetry visible in the next plots is only due to a normal oscillation of the flow coming out from the injector.

4.2.1. Model validation

In the next plots, the results obtained in the simulations are compared with the tested values. In this case, the rail pressure is equal to 10 bar and the chamber pressure is equal to 1 bar.

All the results are normalized because they contain confidential information. The first five plots (from Figure 4.4 to Figure 4.8) are showing the open case. All the data are normalized with respect to the maximum value obtained in the simulation at 3 mm from the injector, Figure 4.5.

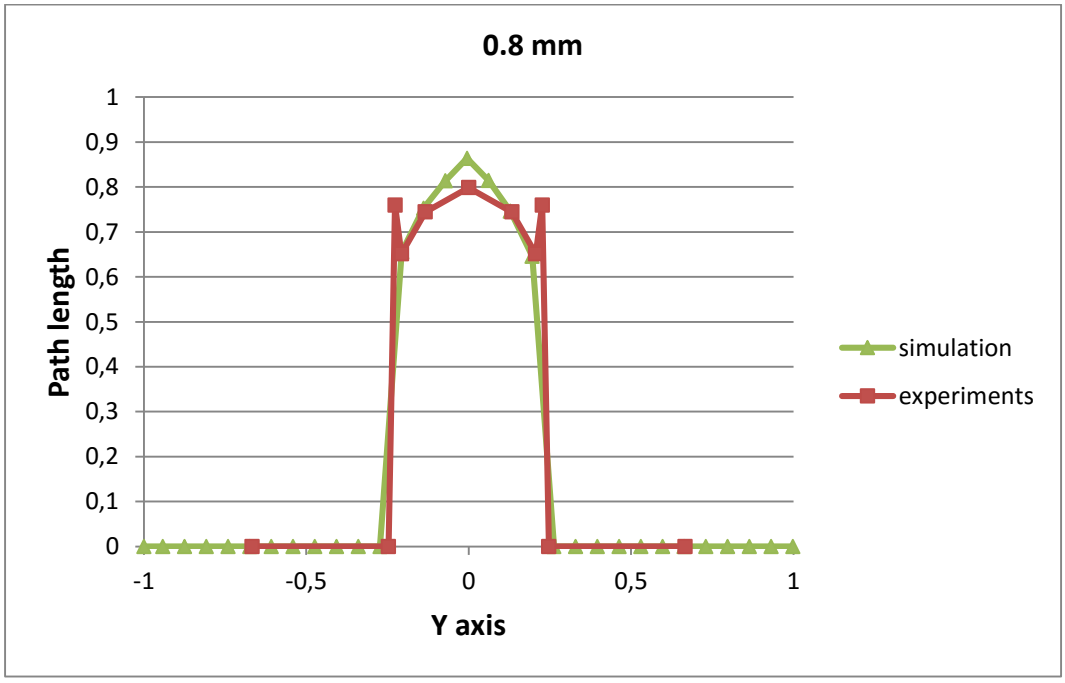

Figure 4.4: Normalized path length for the open case. Simulation and experimental results, 0.8 mm far from the injector, rail pressure 10 bar, chamber pressure 1 bar

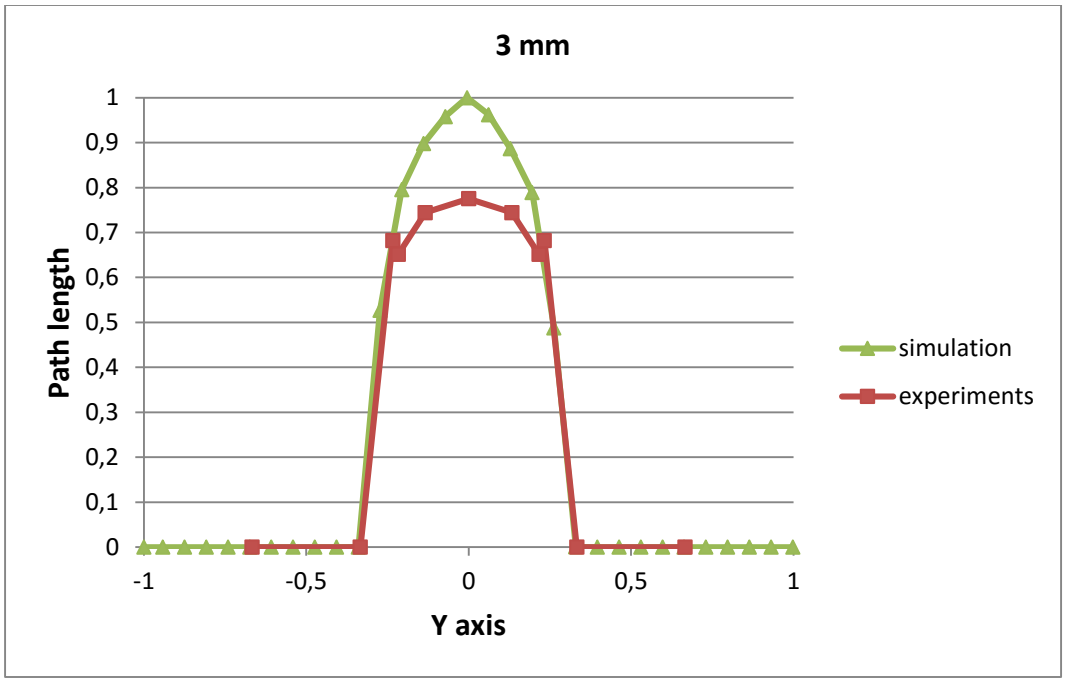

Figure 4.5: Normalized path length for the open case. Simulation and experimental results, 3 mm far from the injector, rail pressure 10 bar, chamber pressure 1 bar

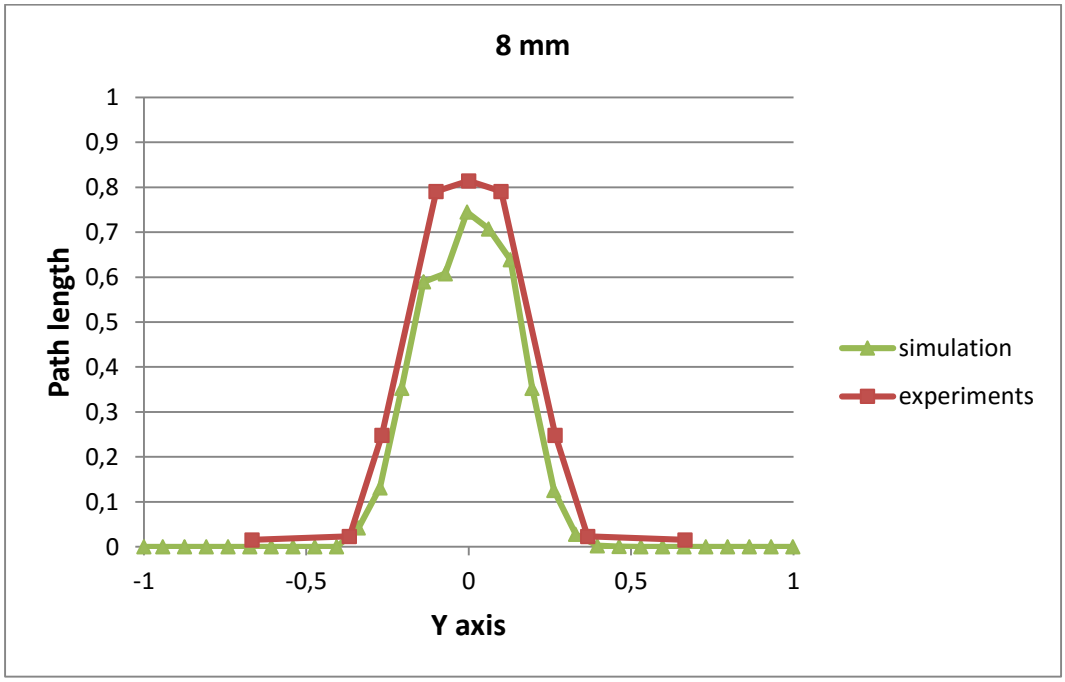

Figure 4.6: Normalized path length for the open case. Simulation and experimental results, 8 mm far from the injector, rail pressure 10 bar, chamber pressure 1 bar

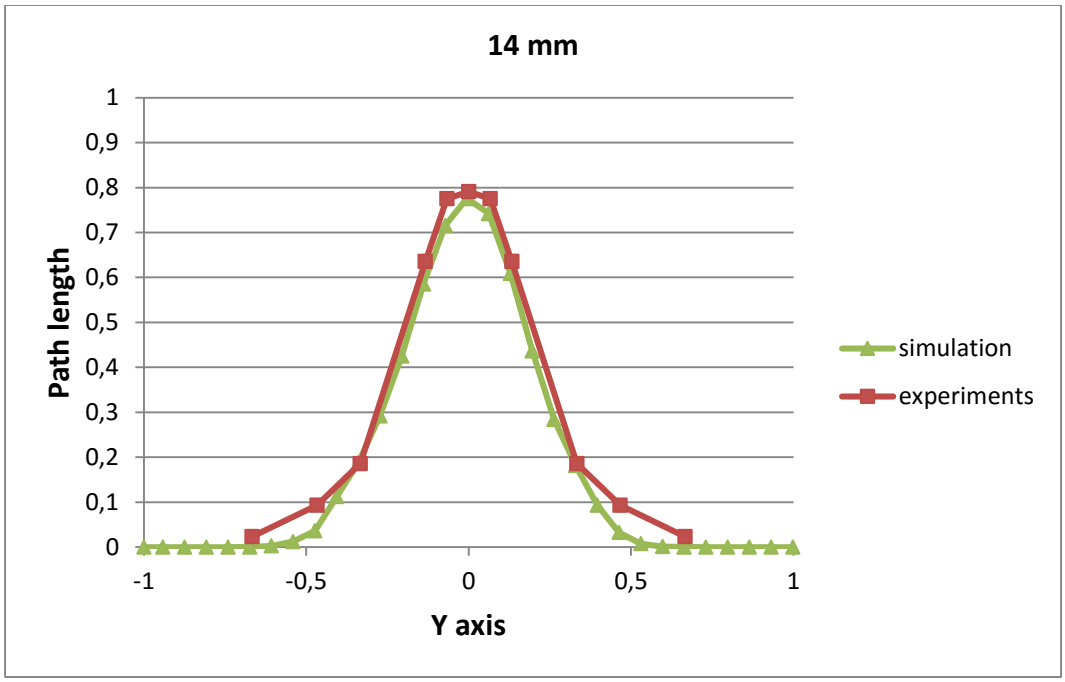

Figure 4.7: Normalized path length for the open case. Simulation and experimental results, 14 mm far from the injector, rail pressure 10 bar, chamber pressure 1 bar

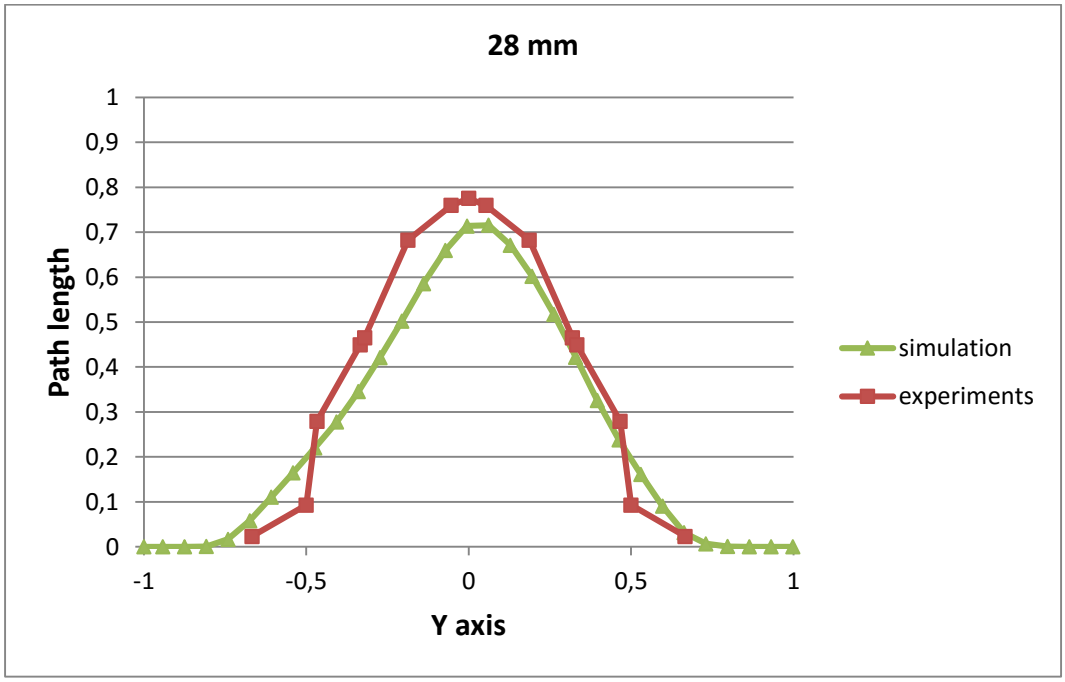

Figure 4.8: Normalized path length for the open case. Simulation and experimental results, 28 mm far from the injector, rail pressure 10 bar, chamber pressure 1 bar

Looking at the showed results and comparing them with the experimental measurements, the model seems working very well. Generally, the peak error is lower than 5% except for the case at 3 mm, Figure 4.5. In this case, the error is close to 20% because the model is over predicting the amount of argon recirculating in this region of the chamber.

In Figure 4.6, the path length obtained in the simulation is not symmetric: the jet is creating large structures and the computed average is not able to compensate them. The experimental path length is always symmetric because obtained from the average of a large number of injection events.

Moreover, looking at Figure 4.5, in the experimental results two small peaks can be observed on the sides of the central peak. In the simulation, this characteristic is not visible. The cause of these two peaks can be found looking at the jet structure shown at the beginning of this chapter and in Figure 4.9 on the left. Along the central integration line, the high concentration zone is encountered twice (a), on the sides this region is encountered once (b) but for a longer path.

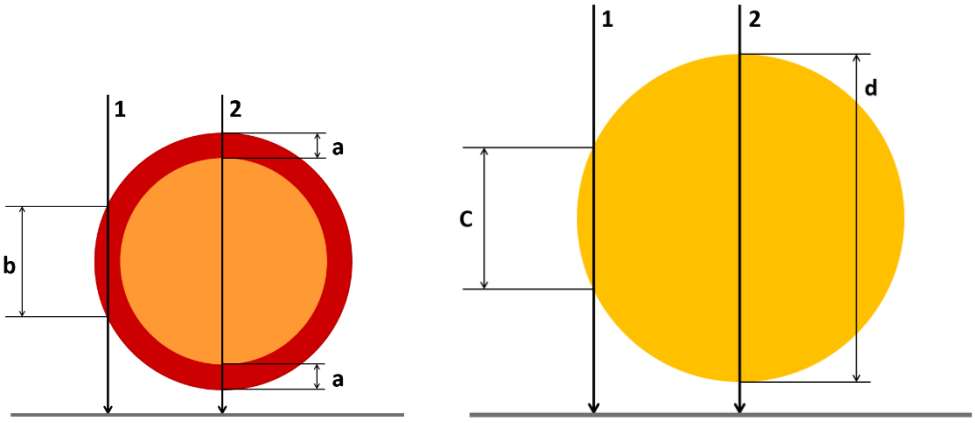

Figure 4.9: Schematic right view of the gas jet in a plane 0.8 mm (on the left) and 8 mm (on the right) far from the injector

Since the path length is obtained integrating along the black arrows, in the simulation the central peak is so high because also the central zone (orange) is full of gas. Instead, from the results obtained in the experimental measurements, it seems that the side peaks are visible because in the core (orange region) a lower amount of gas is present. This is not

occurring farer from the injector (after 8 mm) because the jet becomes solid and full of argon, as shown in Figure 4.9 on the right.

In conclusion, it can be asserted that the difference seen between the results of the simulation and of the experiments is due to an over prediction of the simulated amount of argon in the core region, just downstream from the injector.

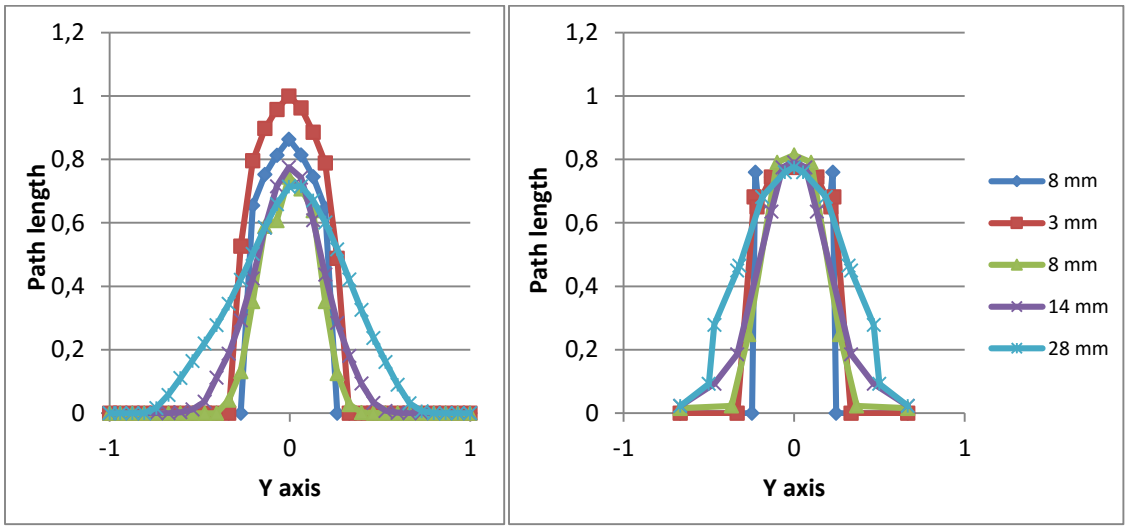

Figure 4.10: Normalized path length for the open case. On the left: simulation results. On the right: results of the experiments

Figure 4.10 shows an overall comparison of the path length between the simulation results (on the left) and the experimental measurements (on the right). In the simulation, the peak is higher close to the injector; in the experiments it is nearly constant at all the distances. In both cases, the width of the jet increases as the distance from the injector increases.

In the following plots the closed case is presented along the lines listed before. All the data are normalized with respect to the maximum value obtained in the simulation at 19 mm from the injector, Figure 4.15.

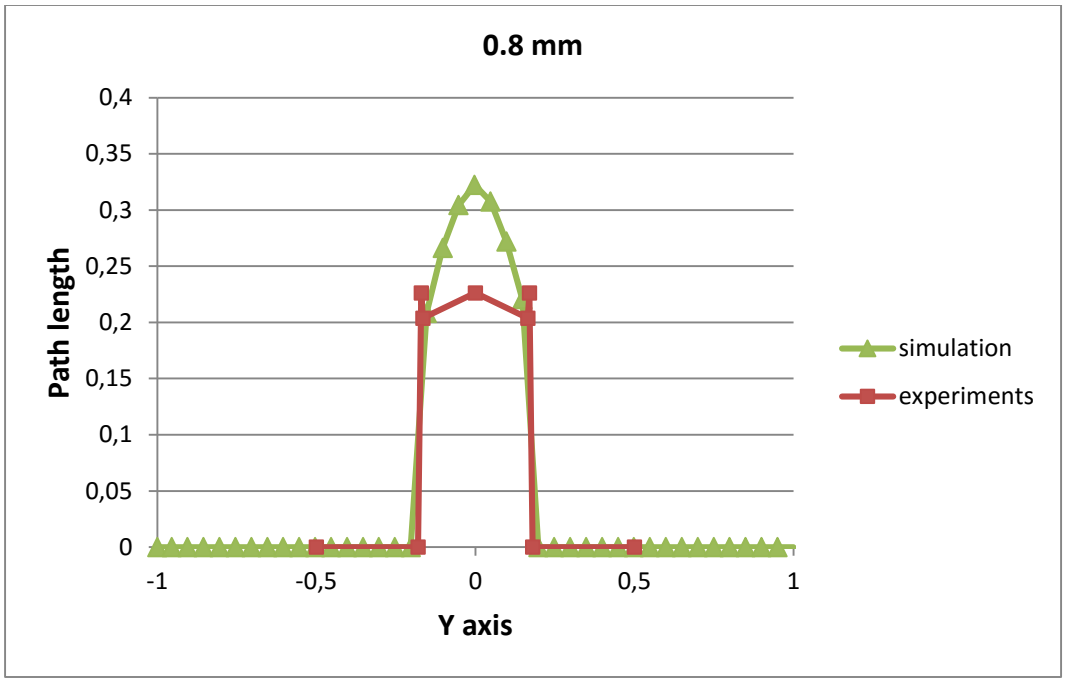

Figure 4.11: Normalized path length for the closed case. Simulation and experimental results, 0.8 mm far from the injector, rail pressure 10 bar, chamber pressure 1 bar

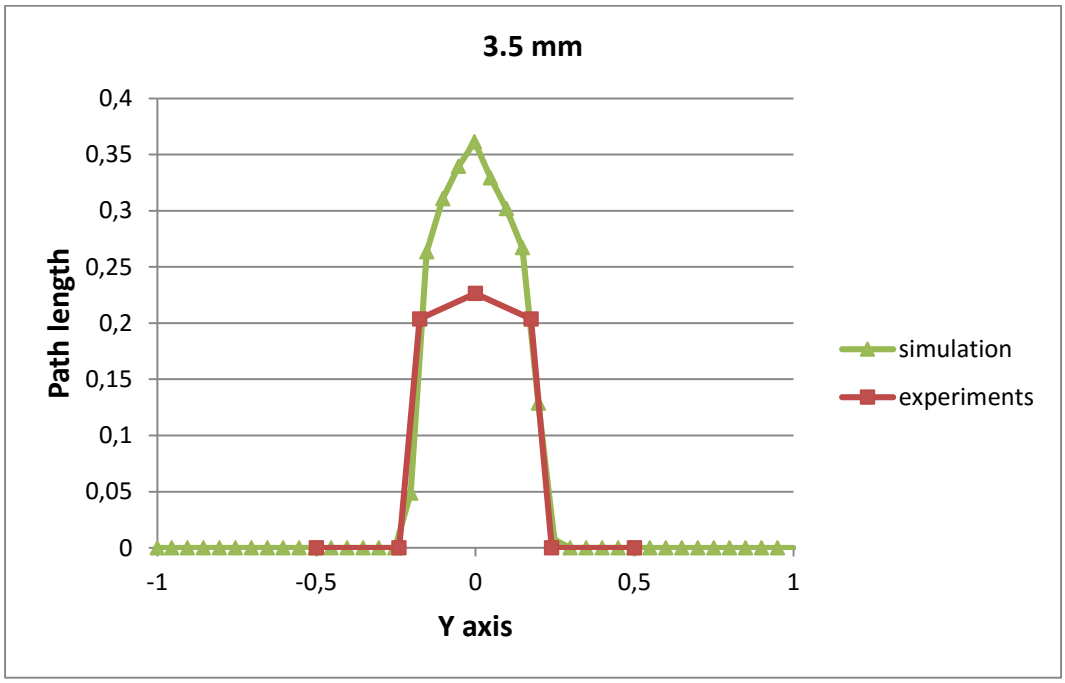

Figure 4.12: Normalized path length for the closed case. Simulation and experimental results, 3.5 mm far from the injector, rail pressure 10 bar, chamber pressure 1 bar

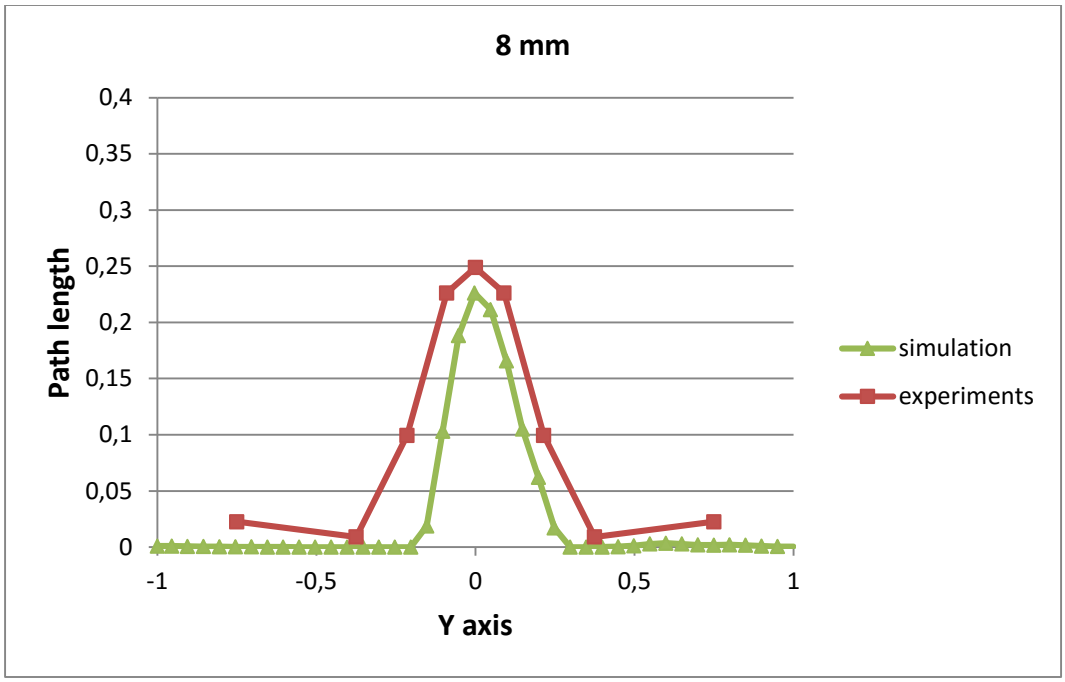

Figure 4.13: Normalized path length for the closed case. Simulation and experimental results, 8 mm far from the injector, rail pressure 10 bar, chamber pressure 1 bar

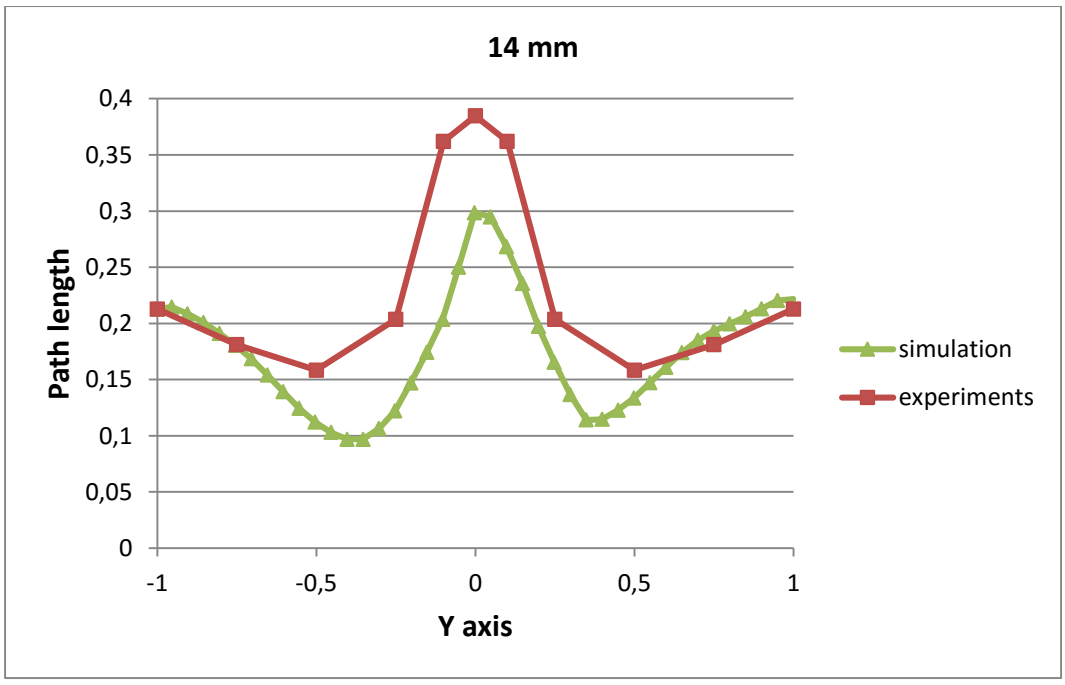

Figure 4.14: Normalized path length for the closed case. Simulation and experimental results, 14 mm far from the injector, rail pressure 10 bar, chamber pressure 1 bar

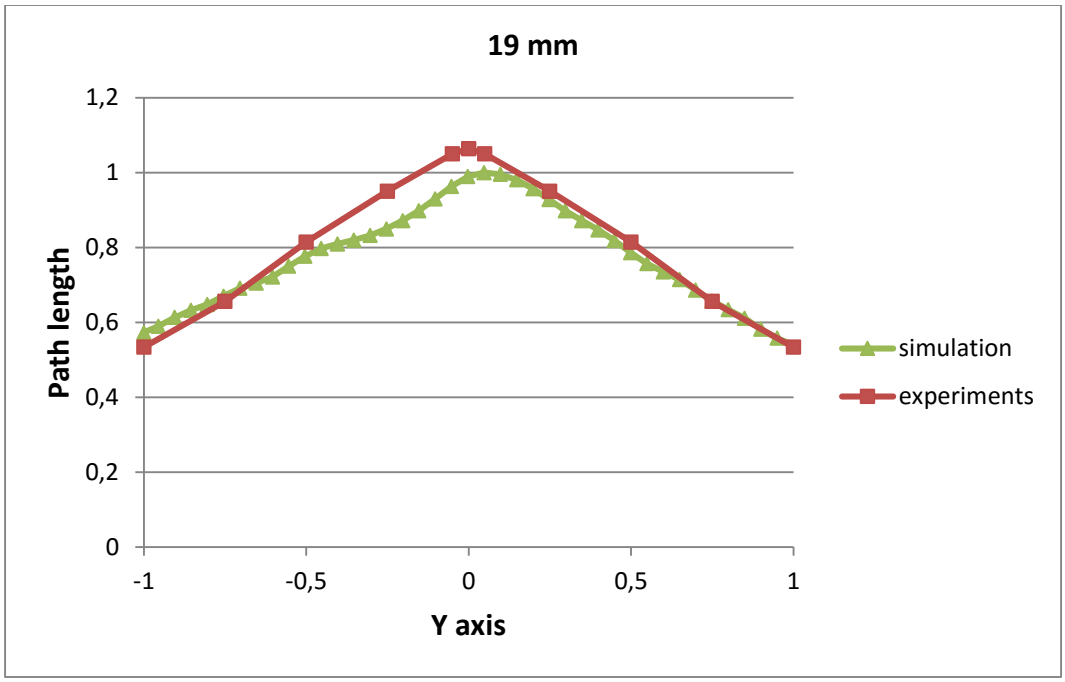

Figure 4.15: Normalized path length for the closed case. Simulation and experimental results, 19 mm far from the injector, rail pressure 10 bar, chamber pressure 1 bar

Looking at the case in which the chamber is closed at the bottom, the model is not describing very well the behavior of the jet in the region just downstream from the injector. More in particular, up to 3.5 mm (Figure 4.11 and Figure 4.12), the amount of argon in the core of the jet is over predicted of a significant amount. However, the width of the jet obtained in the simulations is the same of the experiments.

For the lateral peaks, visible in Figure 4.11, the same considerations done for the open case are valid. Going farer from the injector (Figure 4.13, Figure 4.14, Figure 4.15) the injector is describing much better the shape of the jet. At 8 mm, the width of the flow is a bit under predicted but the peak of the path length is matching well the experimental results. On the contrary, at 14 mm the simulation is getting less argon on the core but there is a good matching on the sides. Finally, at 19 mm, so just close to the wall, the model is approximating very well the amount of argon all over the size of the chamber.

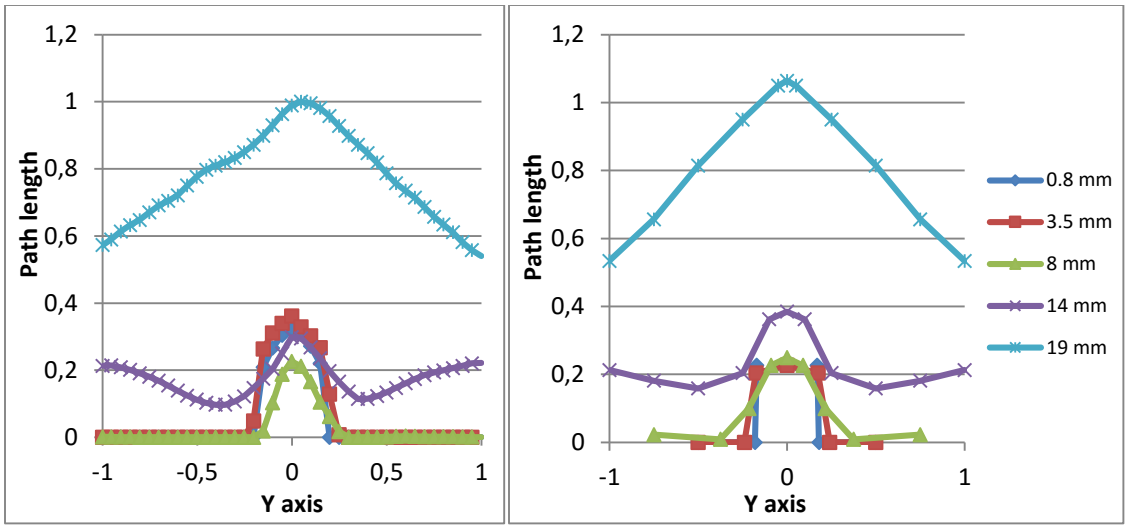

Figure 4.16: Normalized path length for the closed case. On the left: simulation results. On the right: results of the experiments

Figure 4.16 shows an overall comparison of the path length between the simulation results (on the left) and the experimental measurements (on the right), for the closed chamber. From these plots, it can be seen how the amount of argon is much higher close to the wall.

In conclusion, the simulation done with the closed chamber is less precise than the first done with the open chamber. However, since the error is quite large only close to the injector, it can be considered as acceptable.

4.2.2. Other results

In this section, the behavior of the path length is shown for different conditions even if the experimental results are not available. The pressure inside the rail is higher, 15 bar. The value is chosen because it is equal to the maximum working pressure of the injector. The results are compared with the values obtained with a rail pressure of the 10 bar to underline the rail pressure effect on the jet shape. The data are normalized with respect to the same value used in the first open case.

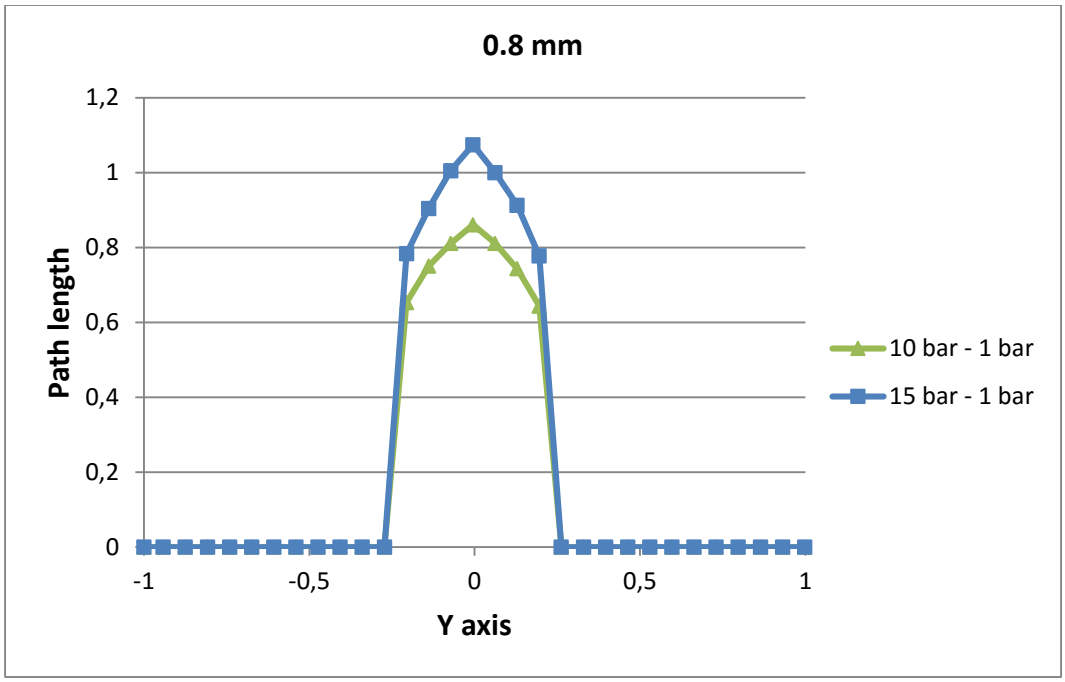

Figure 4.17: Normalized path length for the open case. 0.8 mm far from the injector, chamber pressure 1 bar, rail pressure 10 bar and 15 bar

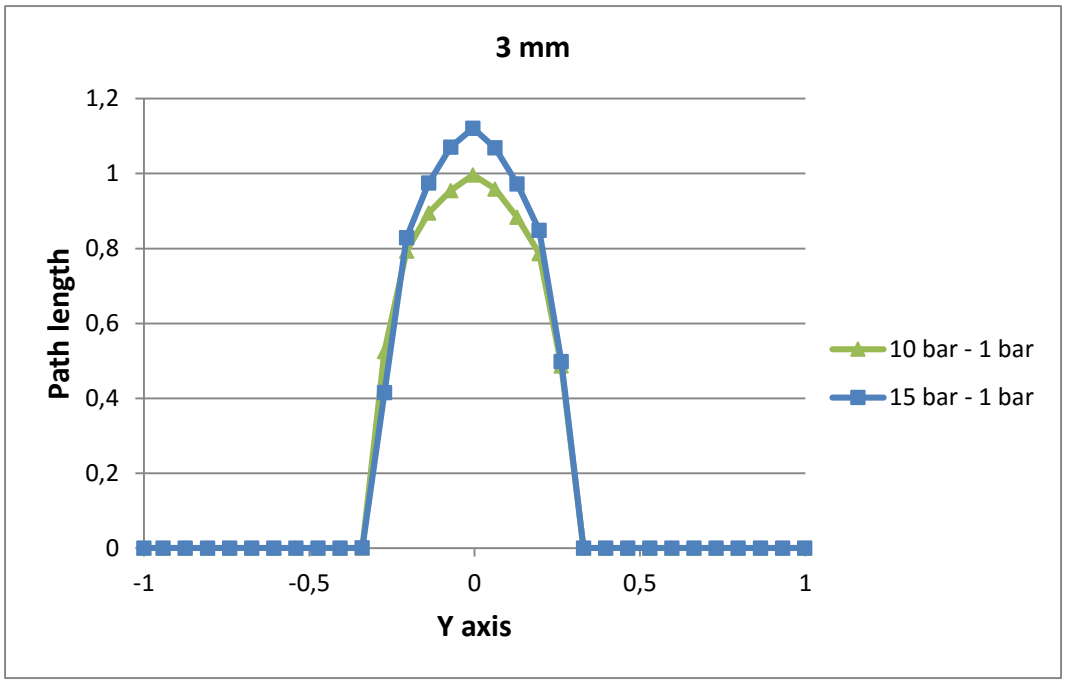

Figure 4.18: Normalized path length for the open case. 3 mm far from the injector, chamber pressure 1 bar, rail pressure 10 bar and 15 bar

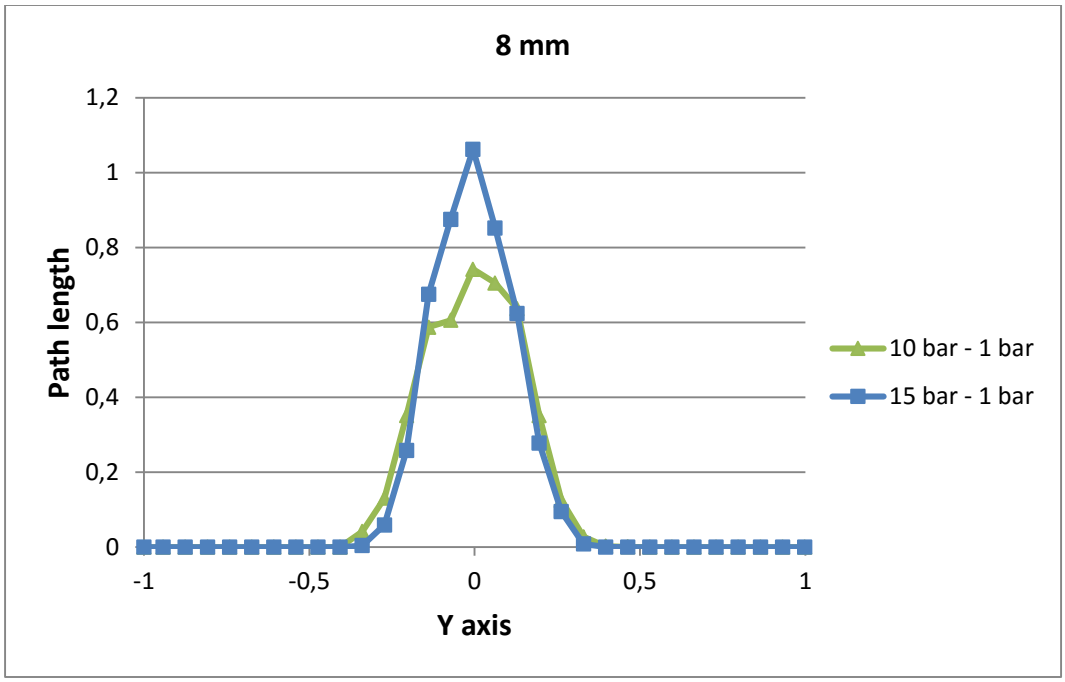

Figure 4.19: Normalized path length for the open case. 8 mm far from the injector, chamber pressure 1 bar, rail pressure 10 bar and 15 bar

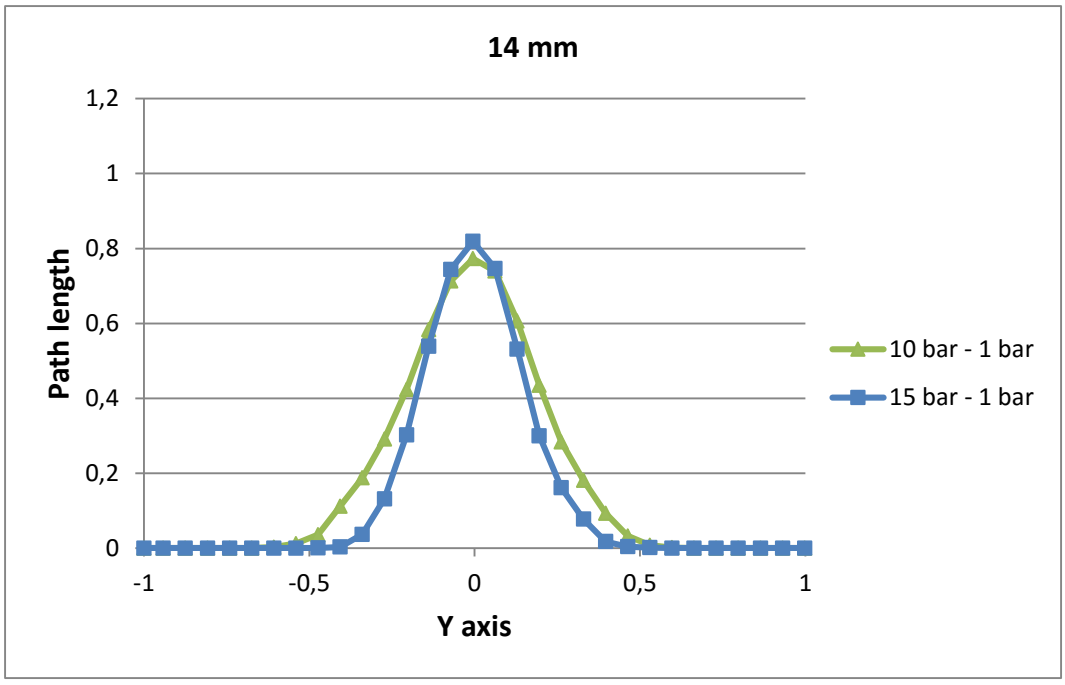

Figure 4.20: Normalized path length for the open case. 14 mm far from the injector, chamber pressure 1 bar, rail pressure 10 bar and 15 bar

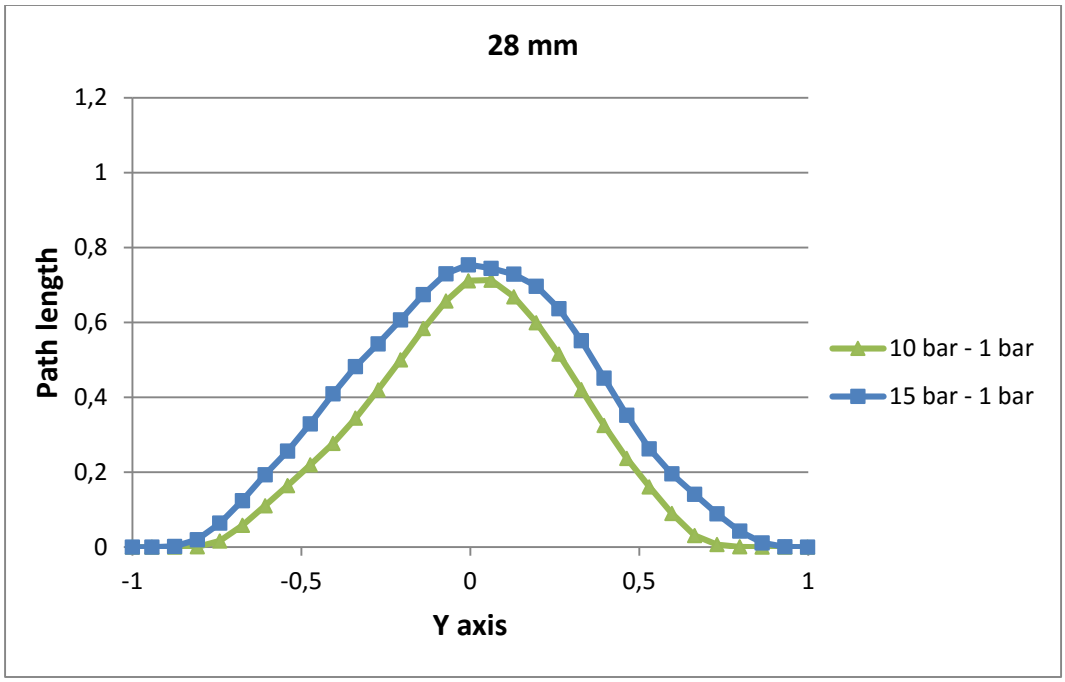

Figure 4.21: Normalized path length for the open case. 28 mm far from the injector, chamber pressure 1 bar, rail pressure 10 bar and 15 bar

From the plots just shown some conclusions can be drawn. The concentration of argon is higher close to the injector when the rail pressure is higher. This is clearly visible up to 8 mm downstream from the injector. It is interesting to notice how the width of the flow doesn't change in these three cases, even if the rail pressure is higher. In the last two cases, 14 mm and 28 mm, this tendency reduces and almost disappears. Moreover, at 14 mm the width of the jet becomes smaller due to a faster collapsing of the flow toward the center. The width increases again at 28 mm due to a higher bouncing effect.

Moreover, also the case in which the pressure in the chamber is equal to 2 bar is shown. In this case, the rail pressure is again equal to 10 bar. The data are normalized with respect to the same value used in the plots just shown.

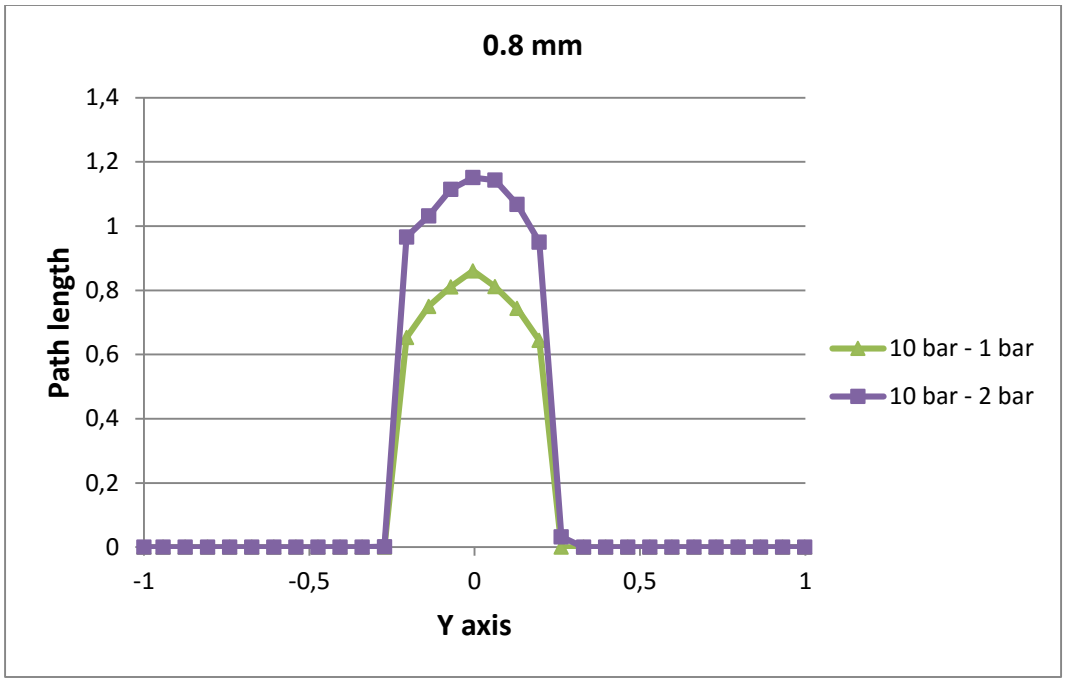

Figure 4.22: Normalized path length for the open case. 0.8 mm far from the injector, rail pressure 10 bar, chamber pressure 1 bar and 2 bar

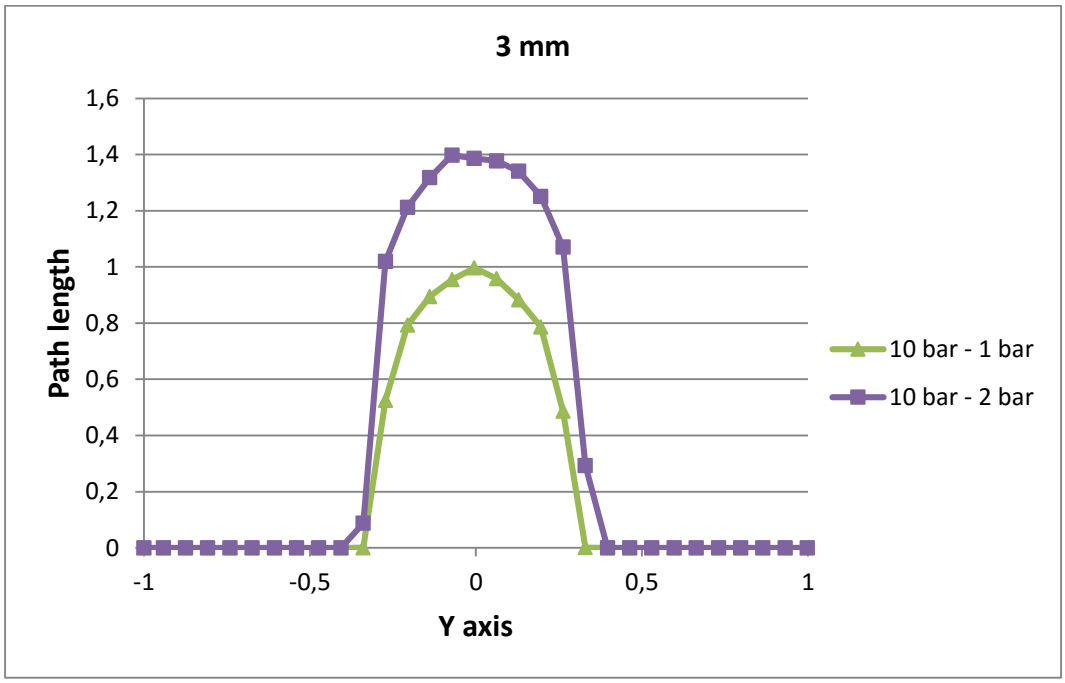

Figure 4.23: Normalized path length for the open case. 3 mm far from the injector, rail pressure 10 bar, chamber pressure 1 bar and 2 bar

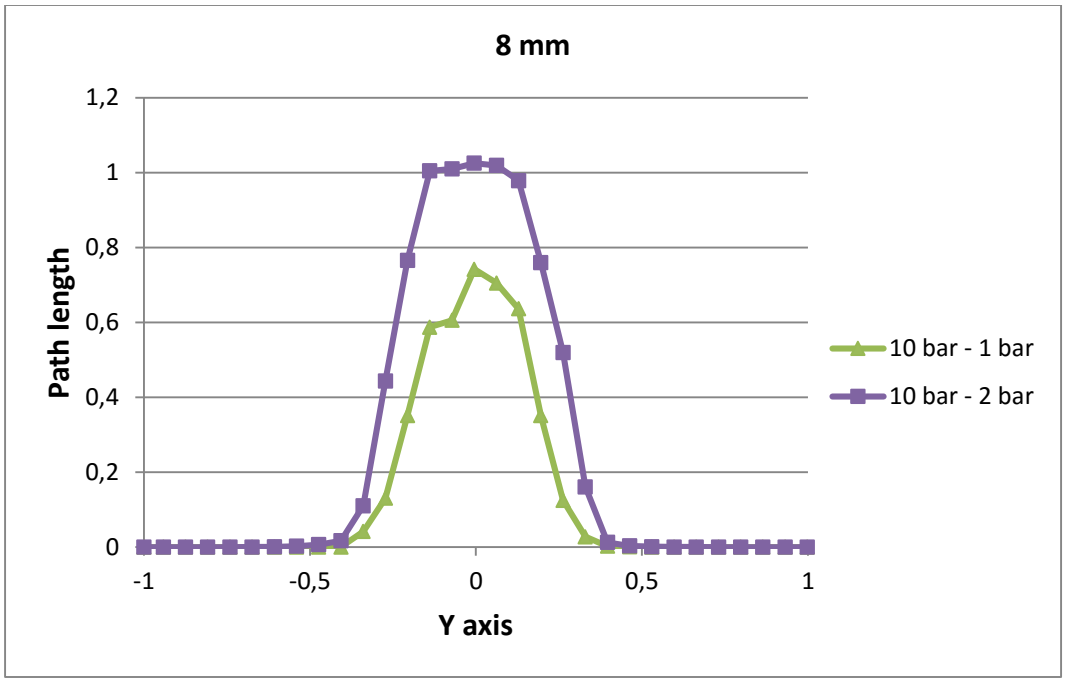

Figure 4.24: Normalized path length for the open case. 8 mm far from the injector, rail pressure 10 bar, chamber pressure 1 bar and 2 bar

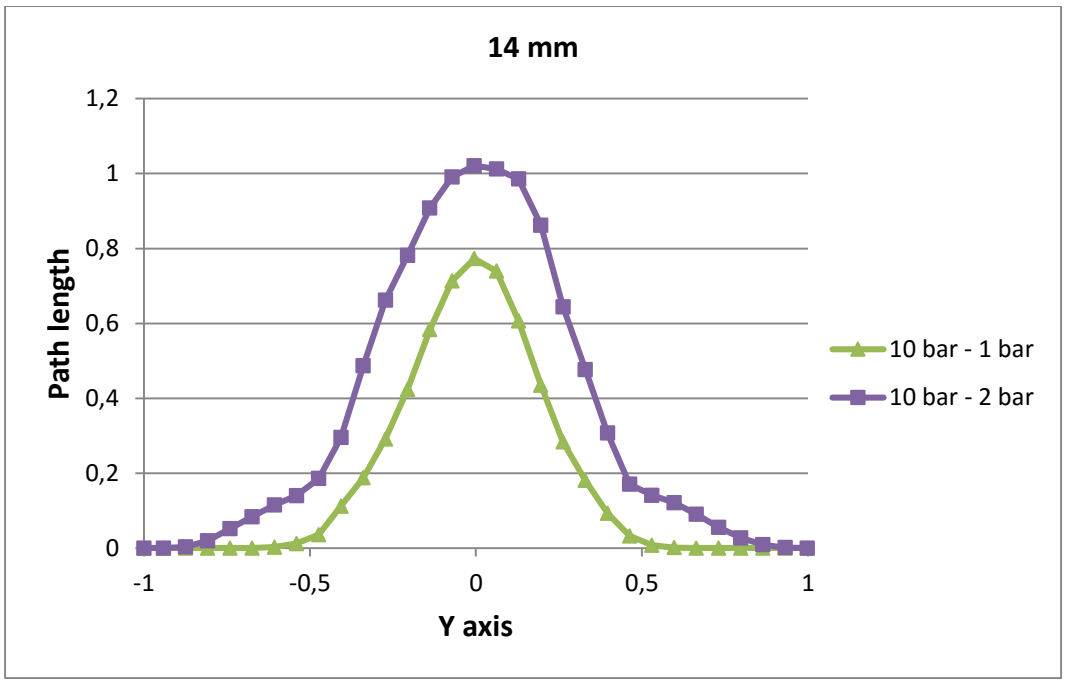

Figure 4.25: Normalized path length for the open case. 14 mm far from the injector, rail pressure 10 bar, chamber pressure 1 bar and 2 bar

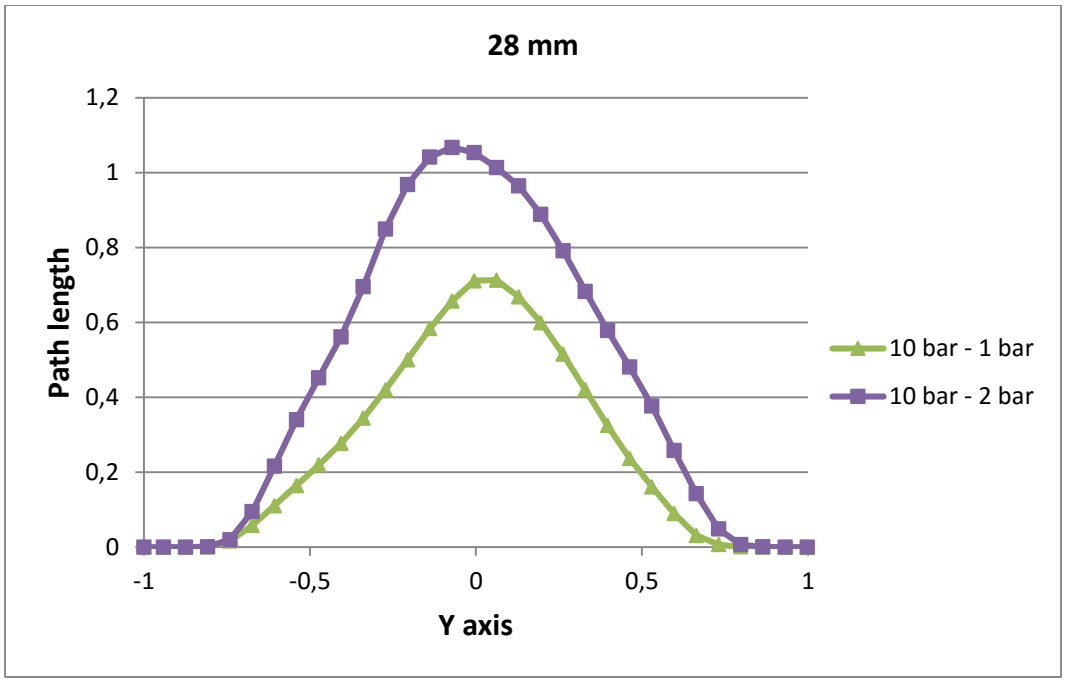

Figure 4.26: Normalized path length for the open case. 28 mm far from the injector, rail pressure 10 bar, chamber pressure 1 bar and 2 bar

From the results shown in these plots, it is possible to see the effect of the chamber pressure on the jet shape. The higher chamber pressure is slowing down the penetration of the injected gas and, as a consequence, along each line the concentration of argon is higher. Just downstream from the injector, Figure 4.22 and Figure 4.23, the width is not changing; the higher amount of argon is caused just by the higher concentration in the core of the jet. This aspect is changing farer from the injector (Figure 4.24, Figure 4.25 and Figure 4.26); the higher chamber pressure is increasing also the jet width. The same effect was also observed in the literature review, in section 2.3.1.

The last case of this section is related again to the closed chamber, so the effect of the impingement against a wall is visible. The rail pressure is increased up to the maximum working value of the injector, 15 bar. The chamber pressure is again equal to 1 bar. The data are normalized with respect to the same maximum value used in the first closed case.

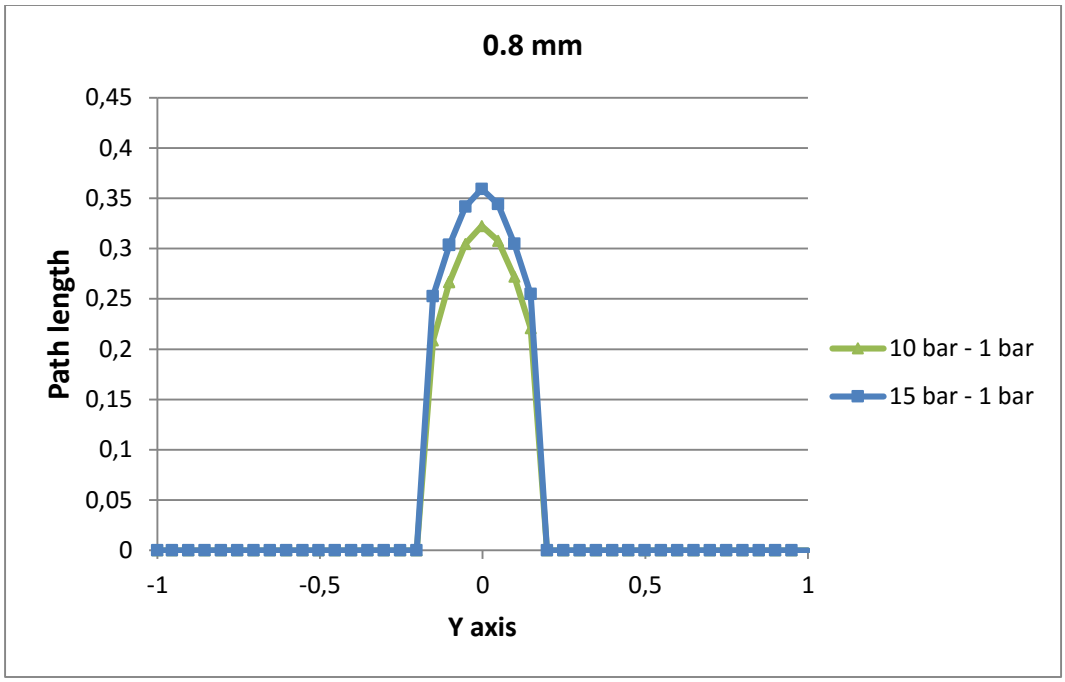

Figure 4.27: Normalized path length for the closed case. 0.8 mm far from the injector, chamber pressure 1 bar, rail pressure 10 bar and 15 bar

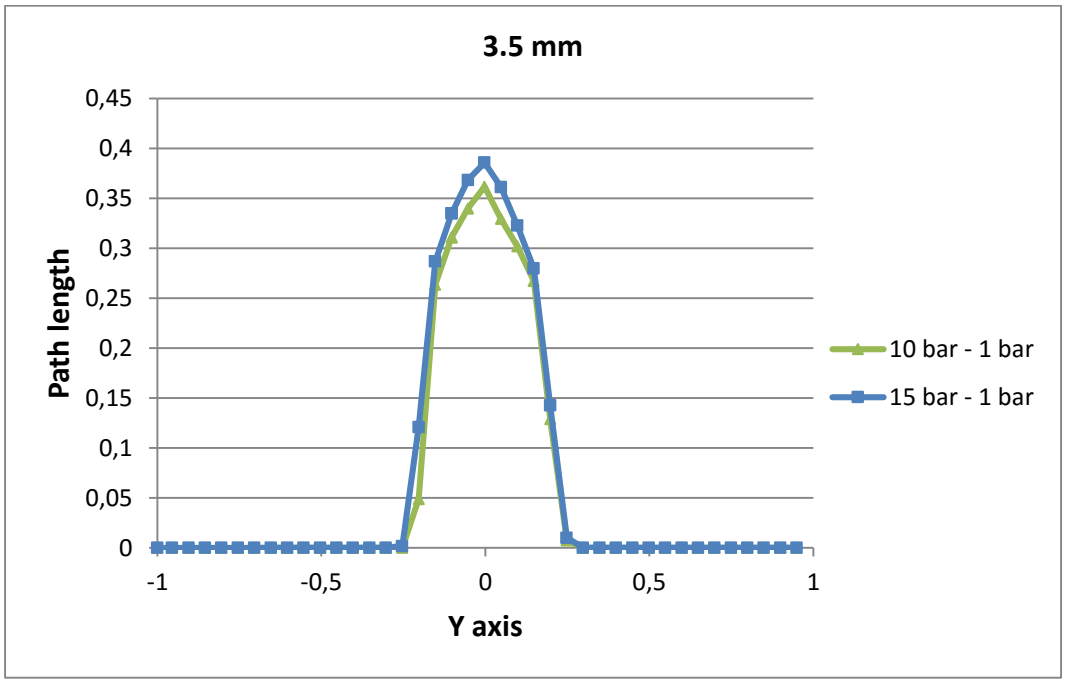

Figure 4.28: Normalized path length for the closed case. 3.5 mm far from the injector, chamber pressure 1 bar, rail pressure 10 bar and 15 bar

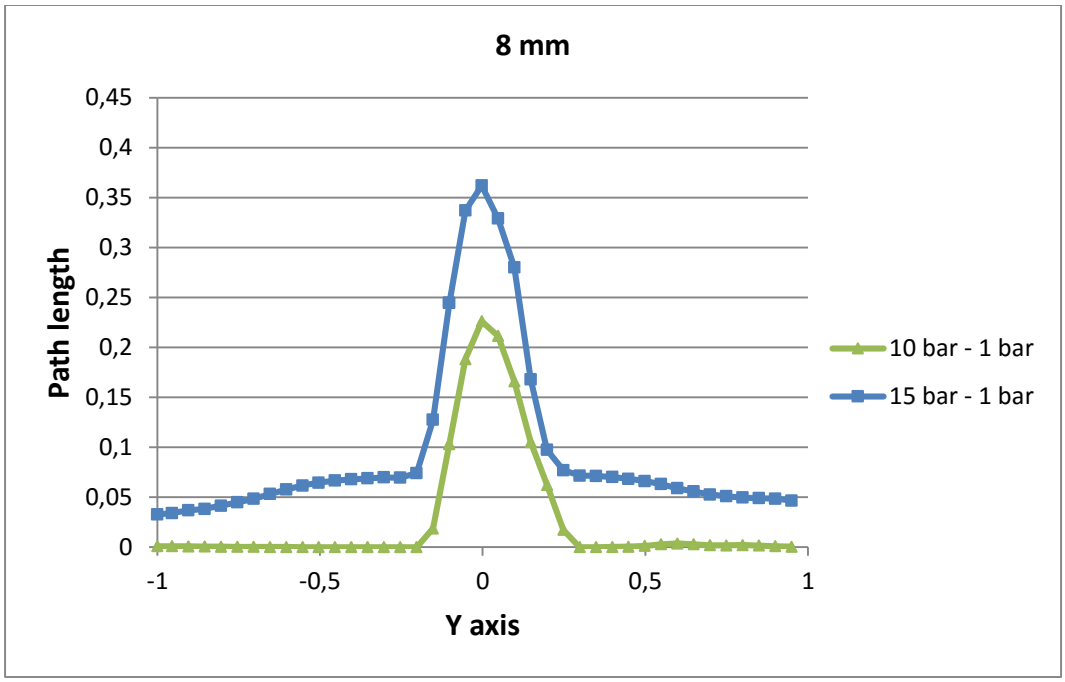

Figure 4.29: Normalized path length for the closed case. 8 mm far from the injector, chamber pressure 1 bar, rail pressure 10 bar and 15 bar

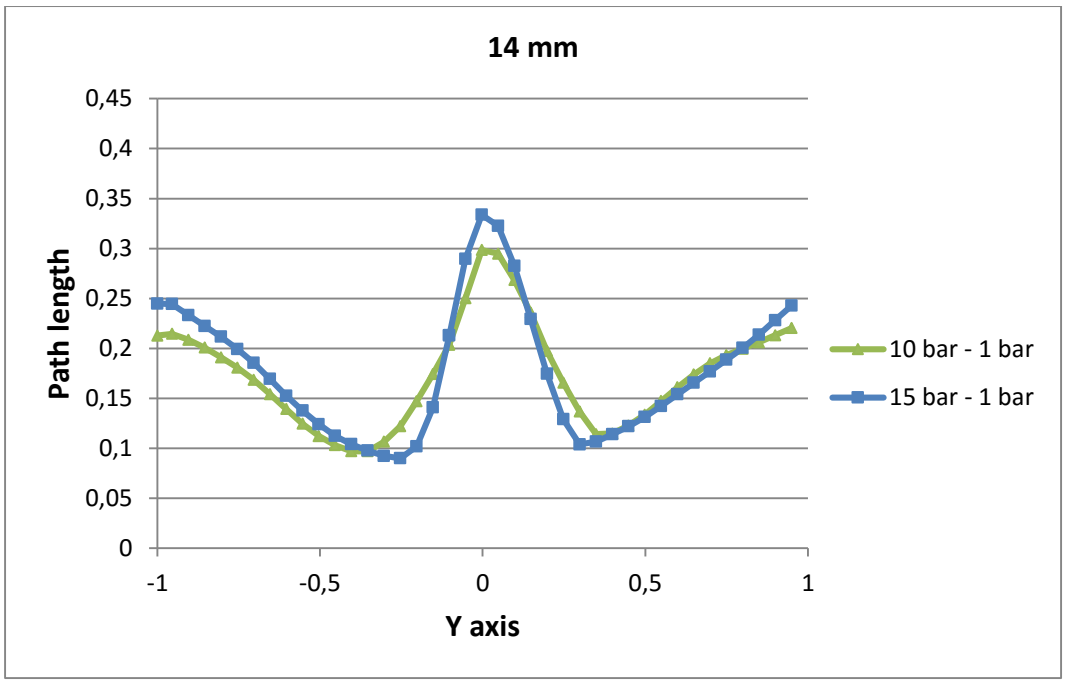

Figure 4.30: Normalized path length for the closed case. 14 mm far from the injector, chamber pressure 1 bar, rail pressure 10 bar and 15 bar

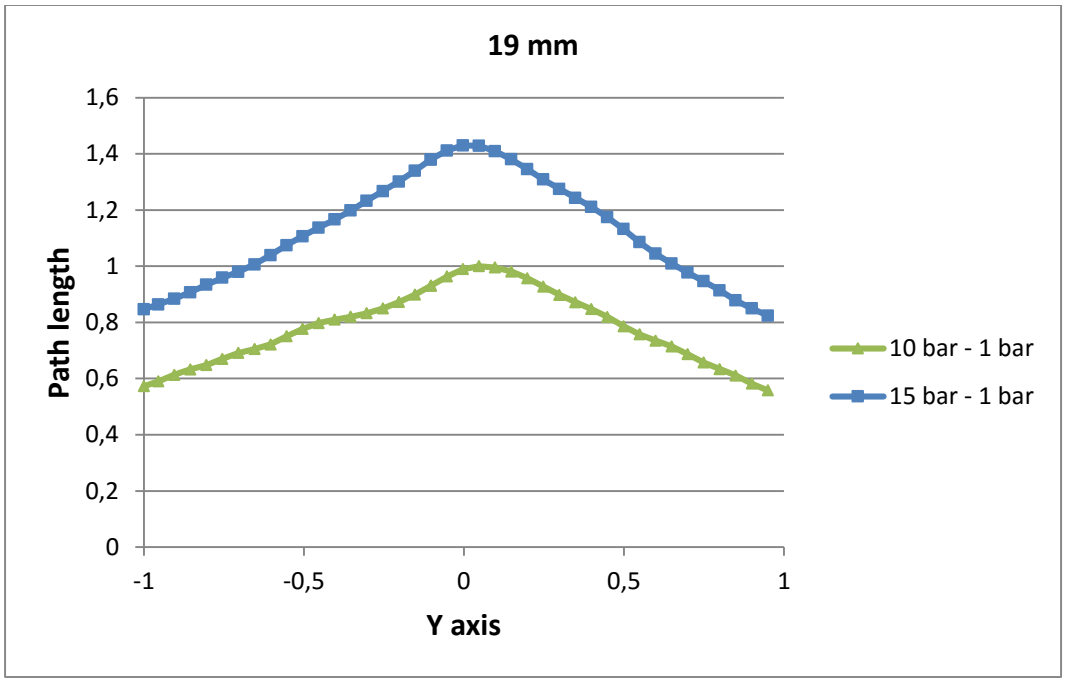

Figure 4.31: Normalized path length for the closed case. 19 mm far from the injector, chamber pressure 1 bar, rail pressure 10 bar and 15 bar

Looking at the results just shown, some considerations can be done. When the pressure is higher, a bigger concentration of argon can be observed in the core in the first three plots (Figure 4.27, Figure 4.28 and Figure 4.29). It is in line with what was observed in the open case.

In the third plot, Figure 4.29, a higher concentration of argon is present also on the sides of the chamber; the effect of the impact against the frontal wall is already visible. With a lower pressure, this effect cannot be seen at this distance from the wall. This also means that if the pressure is higher, and so if the velocity of the flow is higher, the impact against a wall has a larger effect.

In the fourth plot, Figure 4.30, the effect of the higher pressure is quite small; in the core there is a slightly higher concentration of argon, the jet is a bit narrower.

In the last plot, Figure 4.31, the concentration of argon is higher all over the chamber, since the gas is pushed more against the wall.

4.3. Transient results

In this section, the results obtained during the transient phase are analyzed. The transient period includes the opening of the pintle and the penetration time of the jet tip in the chamber. Two important parameters are shown in this part: the mass flow rate and the penetration with respect to time. Moreover, in order to validate the model, the data are compared with the experimental values. For the validation, the results are obtained with a rail pressure of 10 bar and a chamber pressure of 1 bar.

4.3.1. Model validation

The first parameter analyzed in this section, related to the transient period, is the penetration with respect to time. The results coming from the simulation are compared with the experimental data. They are shown in Figure 4.32.

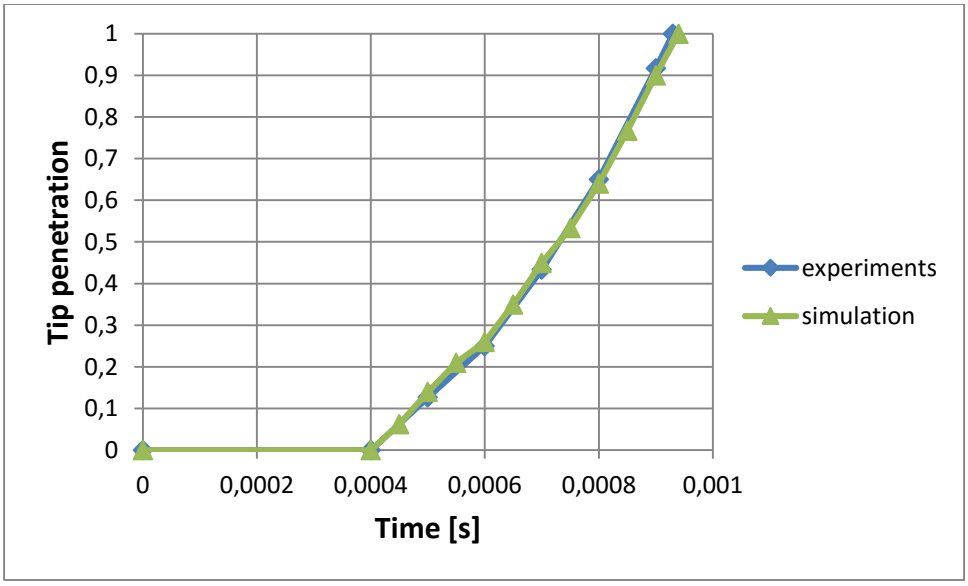

Figure 4.32: Normalized tip penetration obtained in the simulation and in the experiments

The results obtained in the simulation, for the penetration, are matching well the experimental measurements.

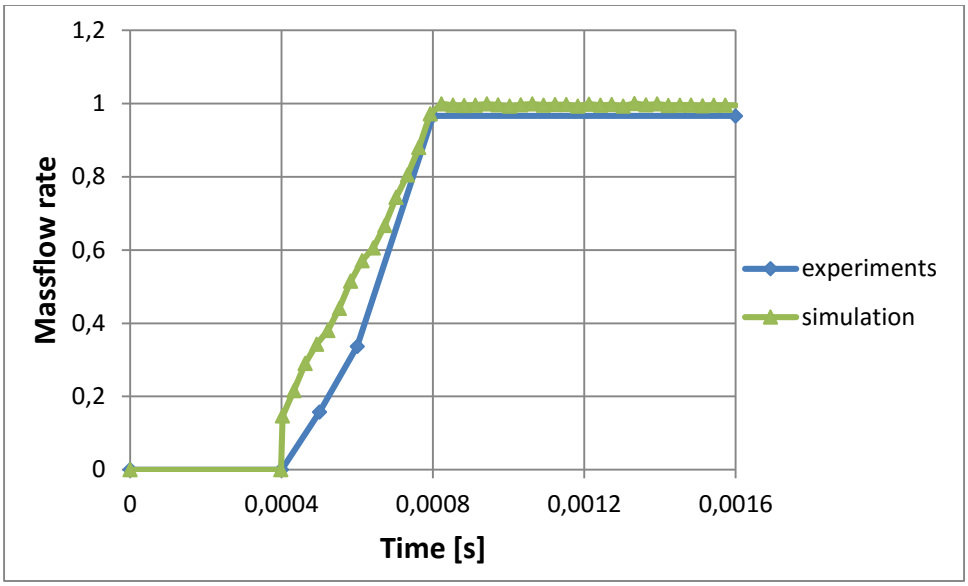

Figure 4.33: Normalized mass flow rate obtained in the simulation and in the experiments

Figure 4.33 shows the mass flow rate with respect to time during the pintle opening and in steady state conditions.

As can be seen looking at the computed mass flow rate, a step appears as soon as the pintle opens. This behavior makes the mass flow rate higher than the tested one.

The step is present because, in Converge^{TM}, two surfaces can never be attached one to each other but at least one cell must be present between them.

This type of gap, between two surfaces, is defined as minimum lift. When the opening starts, this single cell is opened instantaneously creating a sudden increase of the mass flow rate. As the pintle starts moving the computed mass flow rate becomes always closer to the measured one.

At steady state, the mass flow rate is a bit higher than the tested one due a mesh effect. As explained before, the inlet pressure of the model was tuned to get the same measured mass flow rate. This tuning was done with a higher embedding level close to the injector (the level 5 was used). After the evaluation of the mesh effect, it was decided that the level 4 is introducing an acceptable error. This error, close to 3%, is visible in Figure 4.33.

4.3.2. Other results

In this section, the behavior of the penetration and of the mass flow rate is shown for different conditions. First, the pressure inside the rail is increased up to 15 bar, then the chamber pressure is increased to 2 bar reducing again the rail pressure to 10 bar. A higher chamber pressure is considered because, in real engines, the injection may happen also at the beginning of the compression stroke when the pressure becomes higher than 1 bar.

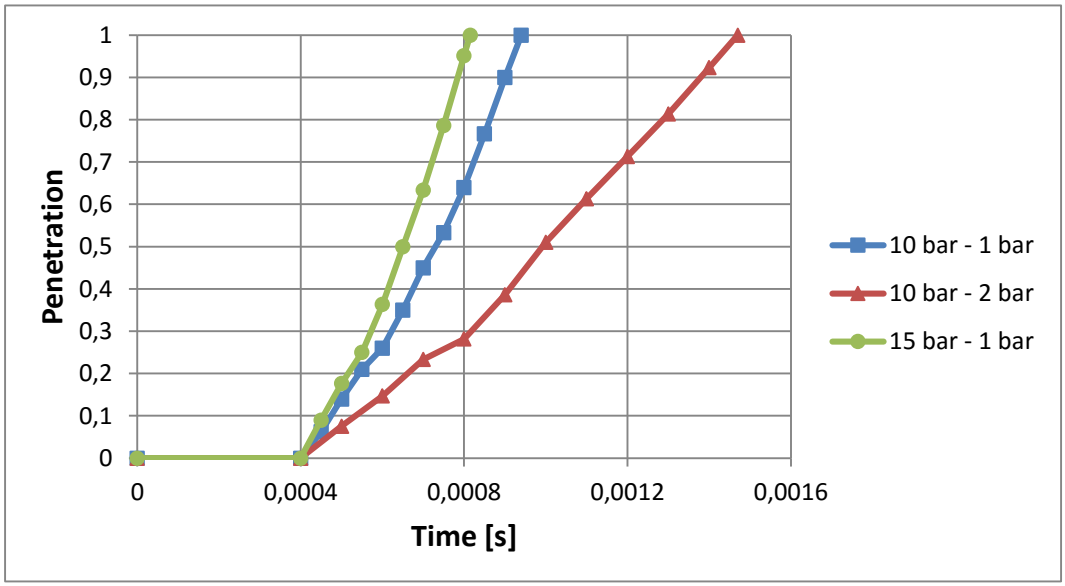

Figure 4.34: Normalized tip penetration with respect to time. Three open cases: rail pressure 10 bar, rail pressure 15 bar and chamber pressure 2 bar

Figure 4.34 shows the normalized tip penetration for the mentioned cases. When the rail pressure is higher, the penetration is higher too. When the chamber pressure increases, the penetration becomes slower (as seen in literature). It is also important to underline that the different penetrations are not related to the difference between the specific values used for the rail and the chamber pressure. When the penetration is slower, the difference between the rail and the chamber pressure is equal to 8 bar. When it is faster the difference is 14 bar, in the central case it is 9 bar.

The change in the slope, visible in the diagram, occurs when the jet collapses toward the center.

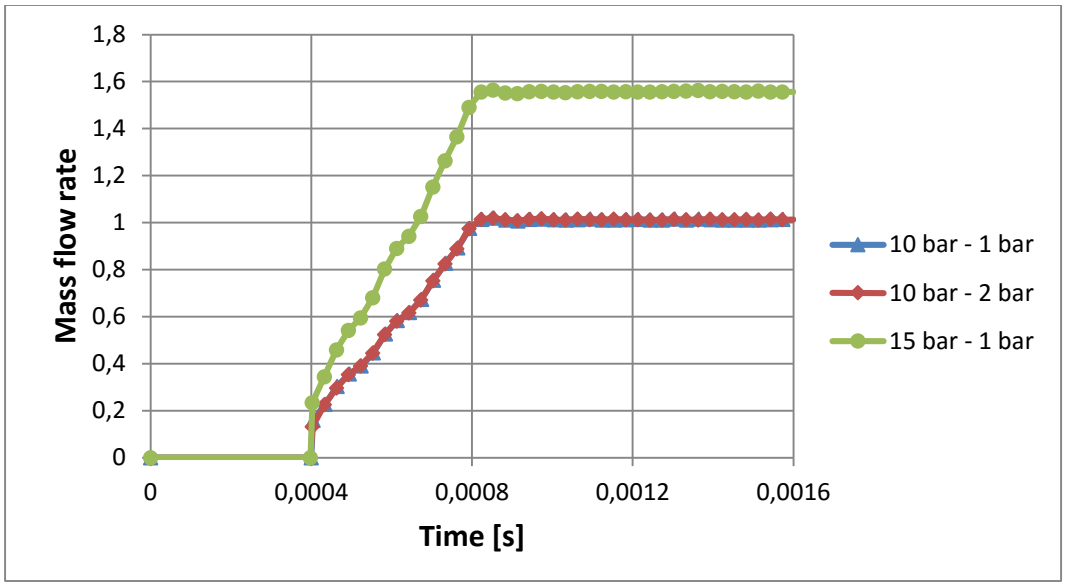

Figure 4.35: Normalized mass flow rate with respect to time. Three open cases: rail pressure 10 bar, rail pressure 15 bar and chamber pressure 2 bar

Figure 4.35 shows the normalized mass flow rate for the mentioned cases. As seen in literature, with a chocked flow, the mass flow rate is strictly related to the pressure upstream from the injector. When the pressure is higher, the mass flow rate becomes higher too.

Moreover, the downstream pressure (i.e. the chamber pressure) has no effect on the mass flow rate. In real engines it means that, with a higher rail pressure, the requested amount of fuel can be injected in a shorter period. This is important especially at high engine speed, because the time available is shorter, and at high load, because the amount of fuel that must be injected is higher.

Moreover, considering the chamber pressure, it is important to notice that it has no effect on the mass flow rate. It means that, if the injection occurs during the compression, its duration must not be modified.

5. RESULTS ON MIXTURE FORMATION

As explained before, the second part of this work is related to the mixture formation. More in particular, the effect of some parameters on the time to form a good mixture is analyzed. In order to do so, some cases are chosen.

During this phase of the research, methane is injected instead of argon. As explained before, the chamber is closed and a precise amount of fuel is injected to obtain an overall stoichiometric mixture. In order inject the right amount of fuel, the mass flow rate during the opening, the closing and in steady state condition is evaluated. The final shape of the normalized mass flow rate is plotted in Figure 5.1. It is also compared with the mass flow rate obtained using argon. In both cases, the rail pressure is equal to 10 bar and the chamber pressure is equal to 1 bar.

The mass flow rate of methane, in steady state conditions, is about 40% lower than the value obtained using argon, with the same conditions.

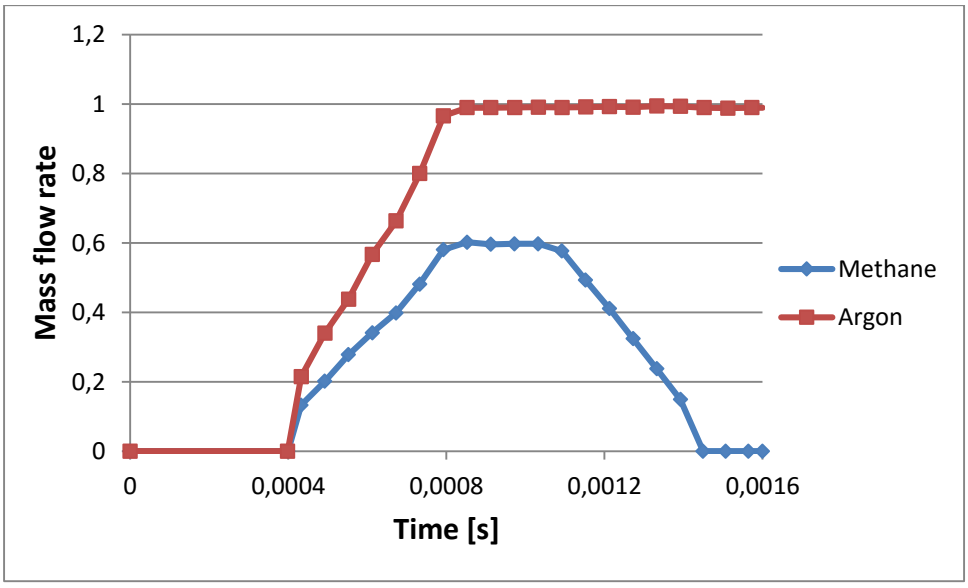

Figure 5.1: Normalized mass flow rate with respect to time using methane and argon with a rail pressure of 10 bar and a chamber pressure of 1 bar. With methane, the complete injection is shown, also considering the closing period

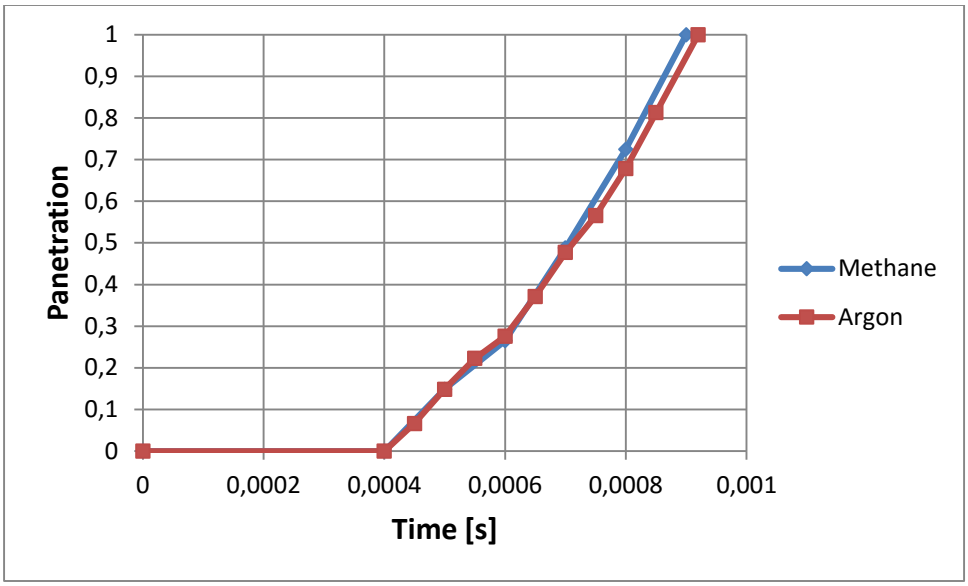

Figure 5.2: Normalized penetration with respect to time using methane and argon with a rail pressure of 10 bar and a chamber pressure of 1 bar

In Figure 5.2, the penetration obtained with the two gases is compared. The difference is very small: only at the end of the path methane is slightly faster.

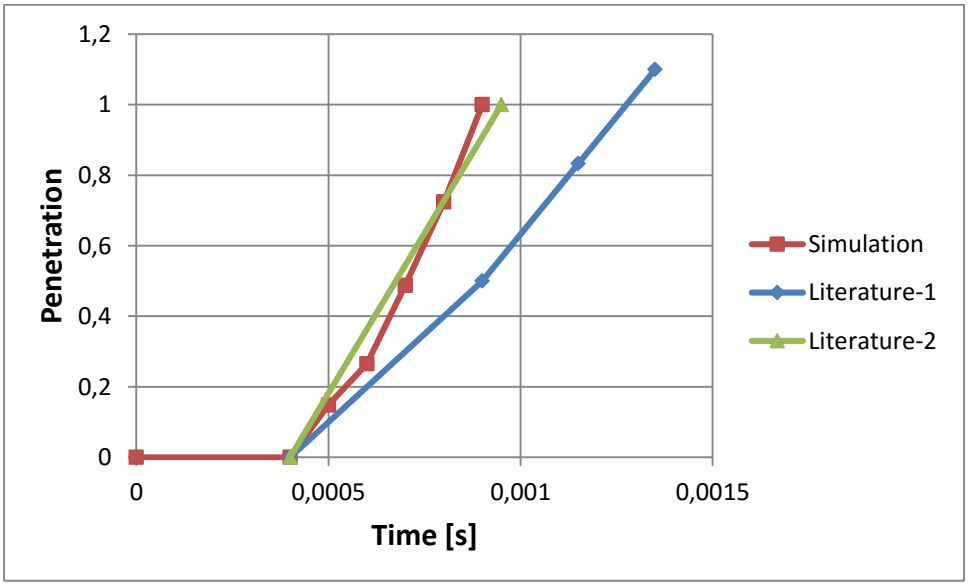

Figure 5.3: Normalized penetration with respect to time using methane with a rail pressure of 10 bar and a chamber pressure of 1 bar. The result of the simulation is compared with two cases found in literature, [8] [18]

In Figure 5.3, the result of the simulation obtained using methane is compared with two cases found in literature ([8] and [18] respectively). In the first research the penetration is much slower; this could be related to the utilization of a different injector. In the second case, the result is very close to the values obtained in the simulation. However, this comparison cannot be used to validate the model because, also in this case, the injector used is different.

5.1. Turbulence effect on the mixture formation

In this first analysis, the injector is in central position and the effect of the turbulent kinetic energy on the mixture formation is evaluated. The results obtained with a calm chamber, in which the initial turbulent kinetic energy is equal to 1 m^2/s^2, are compared with the results obtained imposing two higher turbulence intensities as initial condition. The procedure was explained better in the Chapter 3. Just to remember to the reader, in one case the turbulent kinetic energy is equal to 73.5 m^2/s^2 and in the other it is equal to 216 m^2/s^2. In the next plot the flammability is studied in these three conditions.

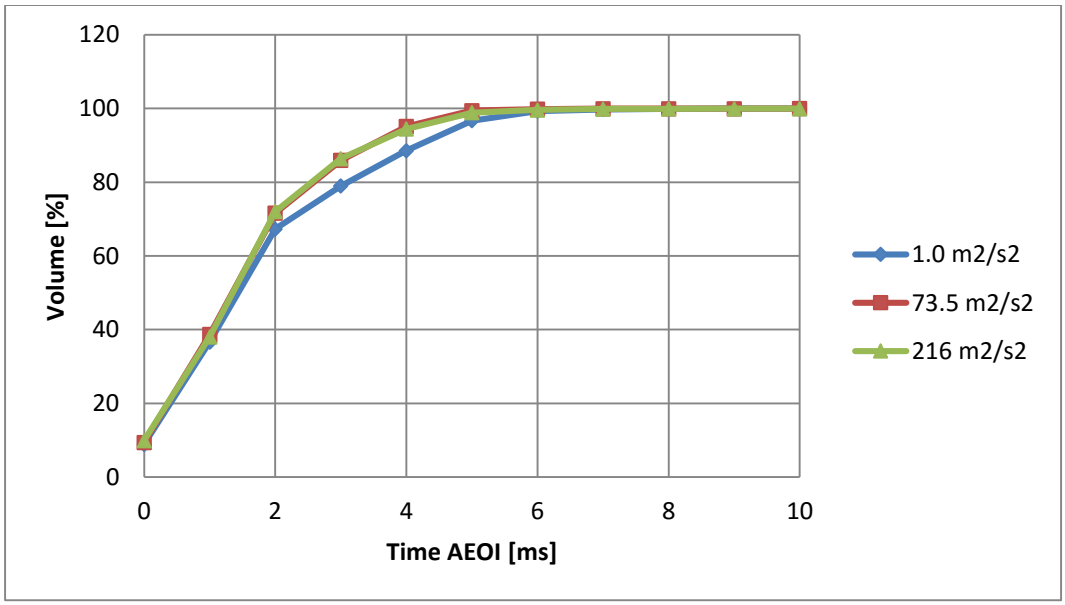

Figure 5.4: Volume in flammable condition with respect to time AEOI. Central injector with a calm chamber and two turbulent chambers

Looking at Figure 5.4, it is clear that a turbulent chamber helps to create a faster mixture. However, increasing the turbulent kinetic energy from 73.5 m^2/s^2 to 216 m^2/s^2 the result does not change. In the best case, the mixture is completely flammable 5 ms after the end of the injection.

For example, considering a real engine running at 3000 rpm, 5 ms means 90 CA deg. Even if the injection finishes 120 CA deg BTDC, the mixture can be burnt 30 CA deg BTDC. It is an acceptable value because, generally, the spark occurs after this point.

After this first analysis, it is worth to go into more details. In Figure 5.5, the rich flammable cases and the lean flammable cases are shown.

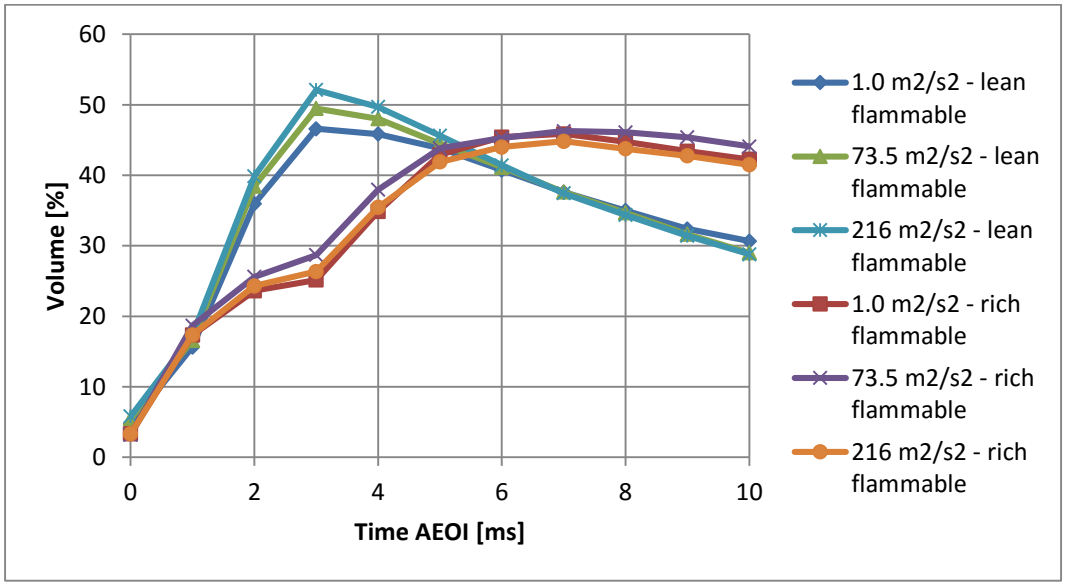

Figure 5.5: Volume in lean flammable and rich flammable conditions with respect to time AEOI. Central injector with a calm chamber and two turbulent chambers

The optimum condition would be the one in which, at the beginning, the two flammable volumes increase as fast as possible to reduce faster the nonflammable regions, then they should reduce as fast as possible to increase the stoichiometric volume.

Looking at the lean case, the highest turbulence is giving the best results, as expected. Considering the rich zone, the medium turbulence is mixing better at the beginning, but then the rich flammable volume is decreasing too slowly.

In conclusion, the highest turbulence is giving the best results.

The next plot, last of this section, is showing again the effect of the turbulence on the mixture formation but considering only the stoichiometric portion of the chamber.

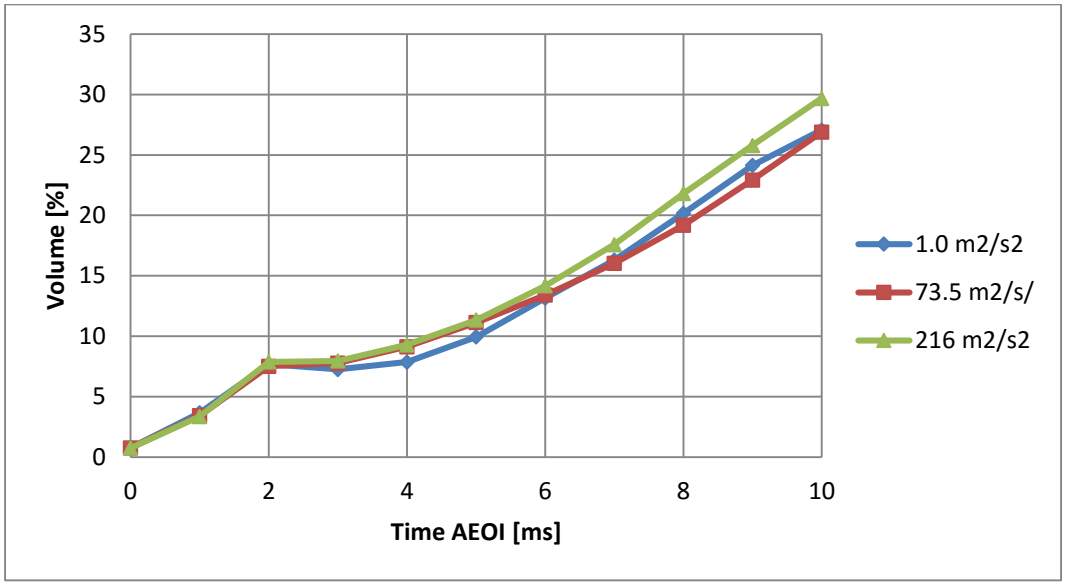

Figure 5.6: Volume in stoichiometric condition with respect to time AEOI. Central injector with a calm chamber and two turbulent chambers

Figure 5.6 shows how the percentage of volume in stoichiometric conditions changes with respect to time. Three values for the turbulence kinetic energy are considered. Looking at the plot, in the first 2 ms there is not any difference between the three cases. Between 2 ms and 6 ms, with a turbulent chamber, the volume increases a bit faster. At the end, only the highest turbulence is producing an improvement with respect to the calm chamber.

5.2. Off-center injector and turbulence effect on the mixture formation

In this section, the effect of the injector position on the mixture formation is shown. When the injector is moved to one side of the chamber, the wall has an effect on the shape of the jet, this is called Coandă effect. In order to have a clear idea of this effect,

Figure 5.7 is showing the mass fraction distribution in the middle plane during the injection of methane, 0.4 ms after the start of the injection.

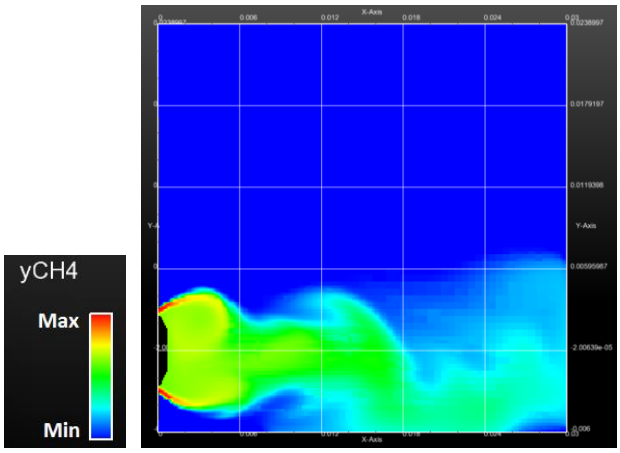

Figure 5.7: Methane mass fraction distribution during its injection with an off-center injector

As can be clearly seen, the wall attracts the jet, as shown in the literature review. The center of the injector is 6 mm far from the side wall. In order to explain better this effect, Figure 5.8 shows the shape of the jet with the injector mounted in central position.

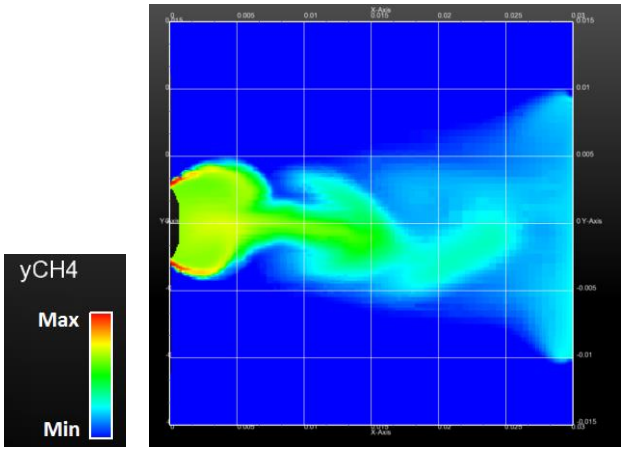

Figure 5.8: Methane mass fraction distribution during its injection with a side injector

After this first consideration, the effect on the mixture formation is analyzed.

First, the effect of the turbulence with the injector mounted in off-center position is shown. This analysis is useful to see the joined effects of the turbulence and of the

injector position on the mixture formation. Also in this case, the calm chamber is compared with the ones in which the initial turbulent kinetic energy is equal to 73.5 m^2/s^2 and 216 m^2/s^2.

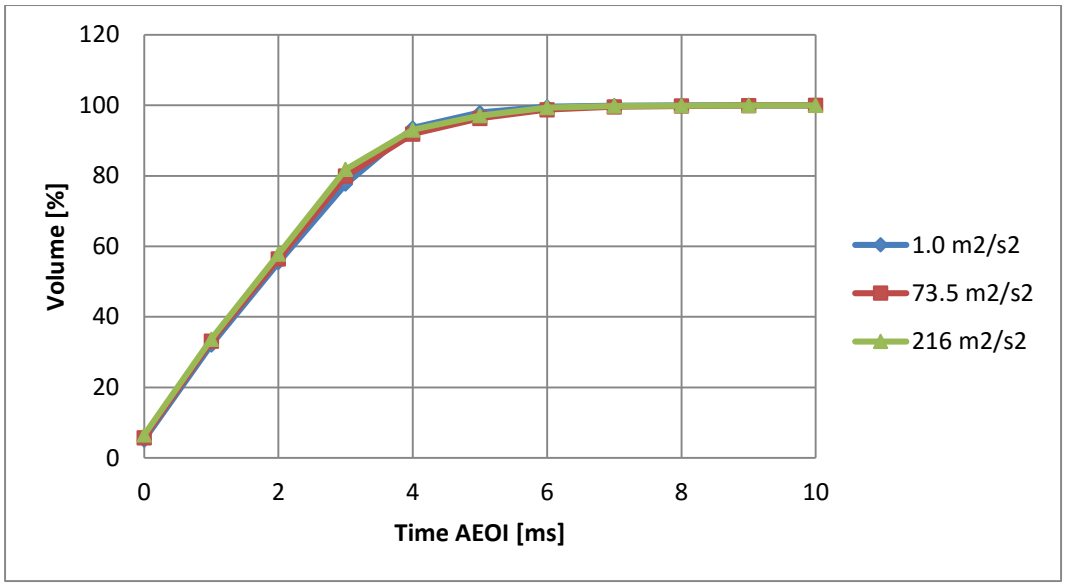

Figure 5.9: Volume in flammable condition with respect to time AEOI. Off-center injector with a calm chamber and two turbulent chambers

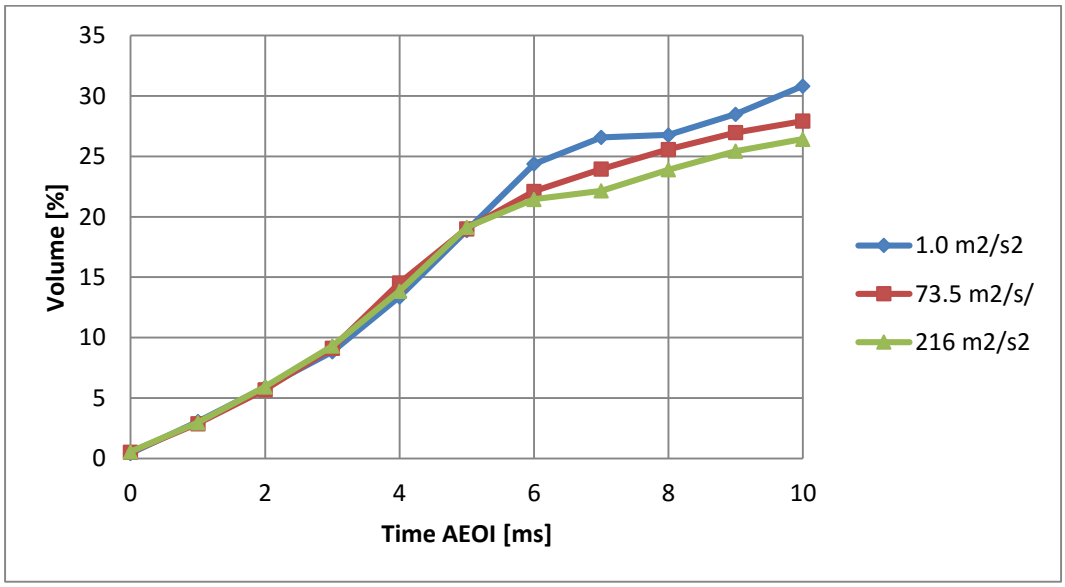

Figure 5.10: Volume in stoichiometric condition with respect to time AEOI. Off-center injector with a calm chamber and two turbulent chambers

Looking at the time necessary for the mixture to become flammable (Figure 5.9), the imposed initial turbulence is not having significant effects with an off-center injector. The reason is that, when the turbulent kinetic energy is higher, it is also dissipating faster on the walls of the chamber.

Observing the percentage of volume in stoichiometric conditions (Figure 5.10), in the first half of the process the turbulence is not having any effect.

At the end, the calm chamber is generating a higher percentage of volume in stoichiometric conditions. At a first sight, this could seem misleading, but it must be kept in mind that at this point the turbulence is nearly dissipated. Moreover, to explain the results obtained, a better analysis is done looking at the velocity of the flow.

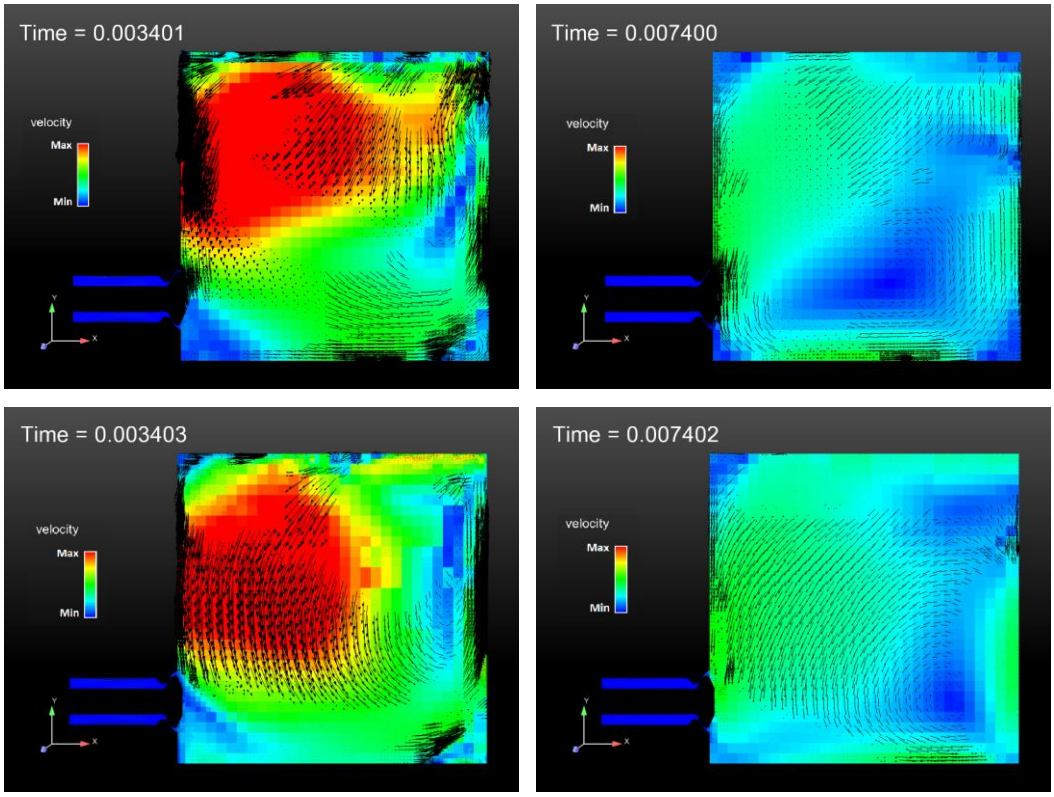

Figure 5.11: Velocity distribution and vector arrows of the flow in the chamber. On top: two cases in which the chamber is turbulent at the beginning of the process. Below: two cases in which the chamber is calm. On the left: time instant 2 ms AEOI. On the right: time instant 6 ms AEOI

In Figure 5.11, the colors show the magnitude of the flow velocity, the vector arrows in black are showing the component of the velocity in the considered plane.

From these images it is clear how, when the turbulence in the chamber is higher, the flow is moving in a more chaotic way and the kinetic energy is also dissipating faster. When the chamber at the beginning of the process is calm, the flow is developing in a tidier way and it is dissipating slower. This is evident especially comparing the two figures on the right. They are showing the time instant corresponding to 6 ms AEOI. This is the time in which the percentage of volume in stoichiometric condition starts to be higher in the calm chamber.

Looking at the colors distribution, in the turbulent chamber the blue region is larger. It means that the flow velocity and so also the mixing process are slower. This can explain the reason because of which, at the end of the process, in the calm chamber the percentage of volume in stoichiometric conditions is higher.

At this point, the results are compared with the values obtained with a central injector.

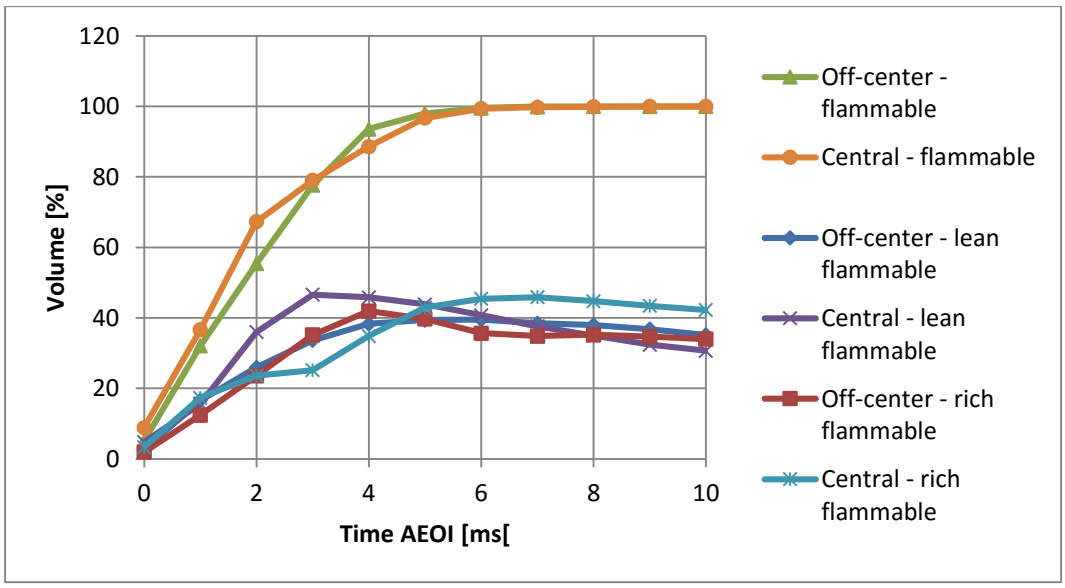

Figure 5.12: Volume in lean flammable, rich flammable and overall flammable conditions with respect to time AEOI. Central and off-center injector cases with a calm chamber

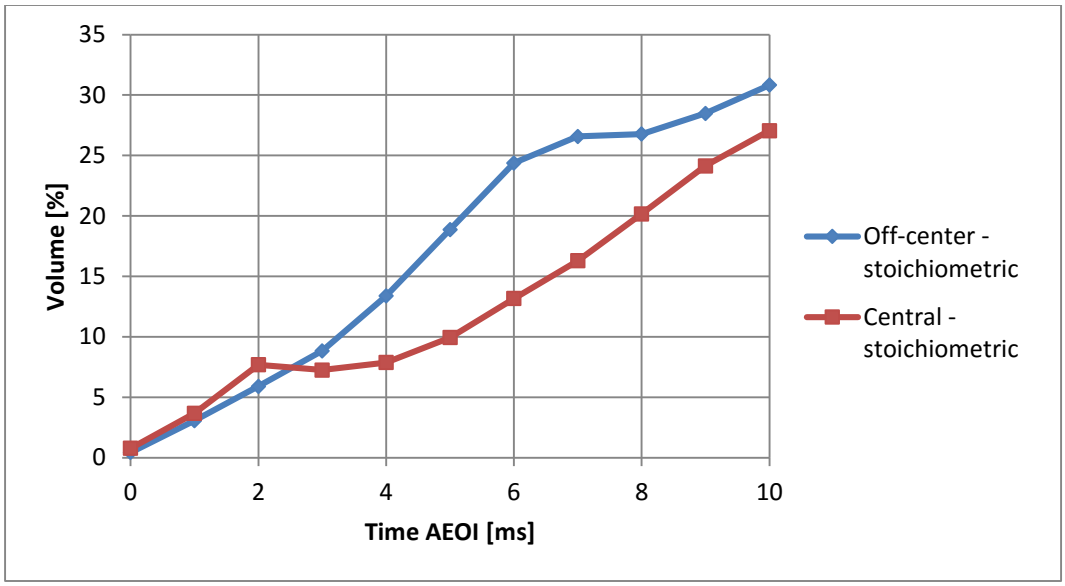

Figure 5.13: Volume in stoichiometric condition with respect to time AEOI. Central and off-center injector cases with a calm chamber

When the chamber is calm, the off-center injector creates a better mixture. Analyzing the results more in details, in the first period the flammable volume (Figure 5.12) is growing faster with the central injector. After 3 ms, the off-center injector is giving better results. At the end, the overall time for the mixture to become flammable is nearly the same in the two cases.

Looking at the percentage of volume in stoichiometric conditions (Figure 5.13), the results are quite different with the two injectors. Up to 2 ms, the central injector is working a bit better. However, after this short period, the off-center injector behaves much better because the percentage of volume in stoichiometric is bigger. When a larger amount of the volume is well mixed (stoichiometric conditions) the combustion can be developed better and so the engine performances are better too. This last consideration allows to say that the off-center injector in working better.

However, in the case just analyzed, the chamber was calm. During the intake in a real engine, the turbulent kinetic energy is quite high. When the intake valves close and the piston starts compressing the gas, the turbulence starts dissipating. For this reason, as it was done before, in the next cases a higher value for the turbulent kinetic energy is imposed as initial condition. The first value chosen is 73.5 m^2/s^2.

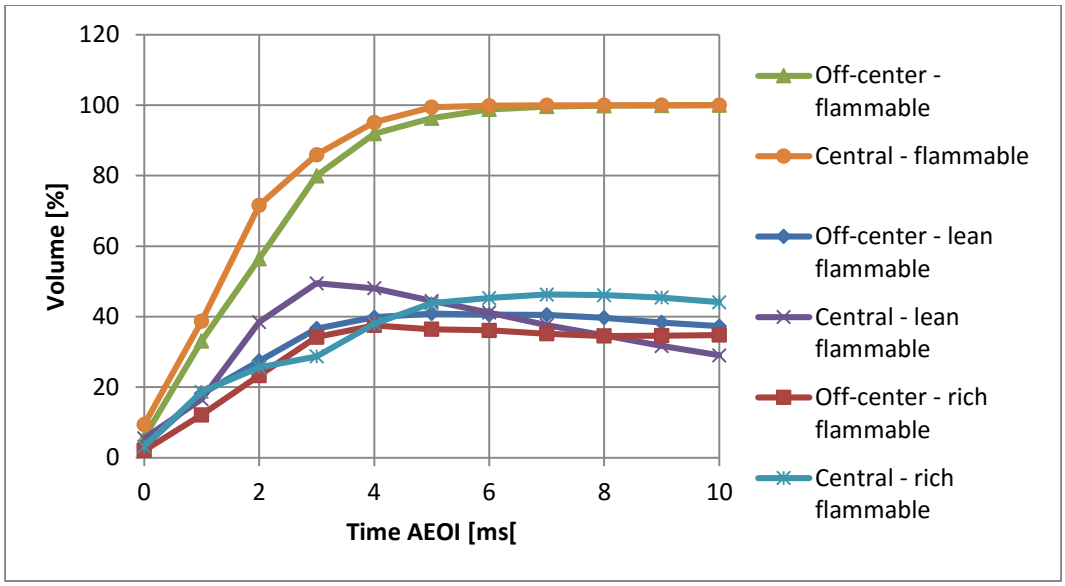

Figure 5.14: Volume in lean flammable, rich flammable and overall flammable conditions with respect to time AEOI. Central and off-center injector cases with the initial turbulent kinetic energy of the chamber equal to 73.5 m2/s2

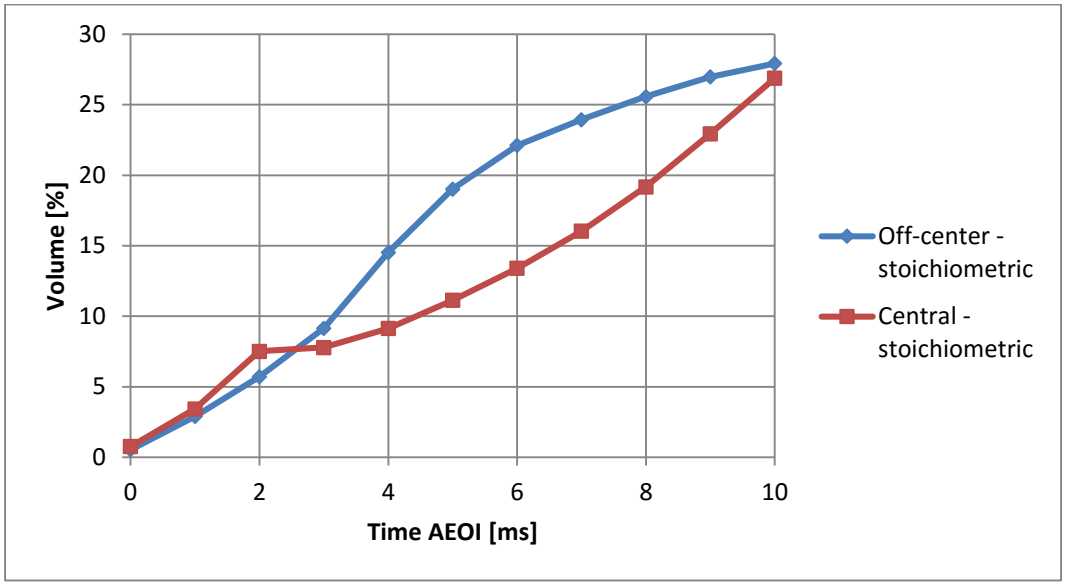

Figure 5.15: Volume in stoichiometric condition with respect to time AEOI. Central and off-center injector cases with the initial turbulent kinetic energy of the chamber equal to 73.5 m2/s2

In these conditions, the gap between the two injectors is reduced. In the analysis done before with the central injector, the initial turbulence was increasing the mixing

performance. On the contrary, this was not true for the off-center injector. For this reason, looking at the time to form a completely flammable mixture, the central injector is now behaving better than the off-center one.

In the stoichiometric case, the same observations done for the calm chamber are valid but, in the last period, the off-center injector behaves worse than before. The final percentage of volume in stoichiometric condition is almost the same with the two injectors.

In conclusion, looking at the combination of the positive and negative aspects, the off-center injector is still working better than the central one.

Finally, the case in which the initial turbulent kinetic energy is equal to 226 m^2/s^2 is considered. The results obtained with a central injector are compared with the ones obtained with an off-center injector.

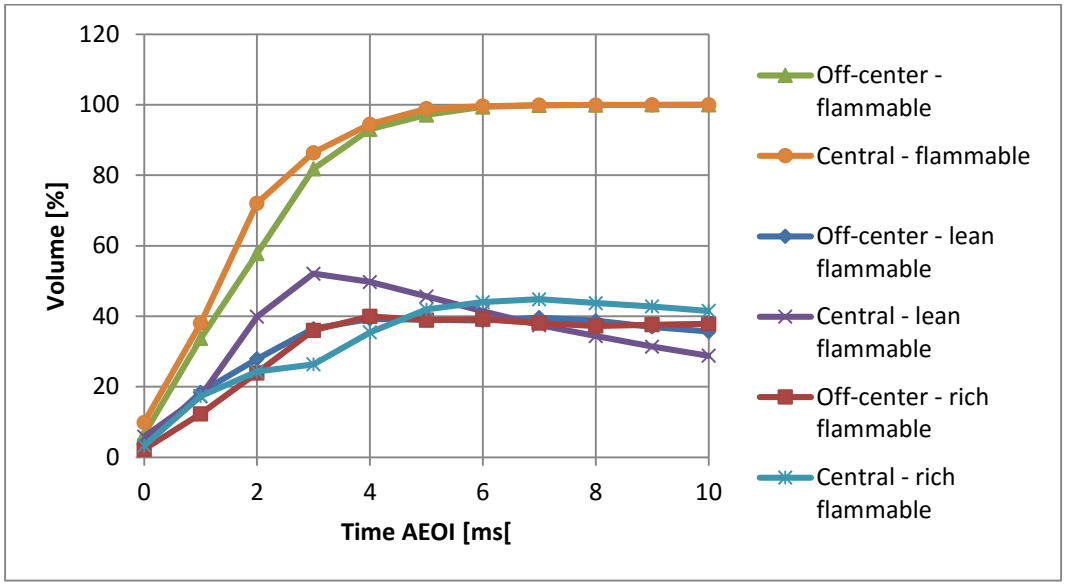

Figure 5.16: Volume in lean flammable, rich flammable and overall flammable conditions with respect to time AEOI. Central and off-center injector cases with the initial turbulent kinetic energy of the chamber equal to 216 m2/s2

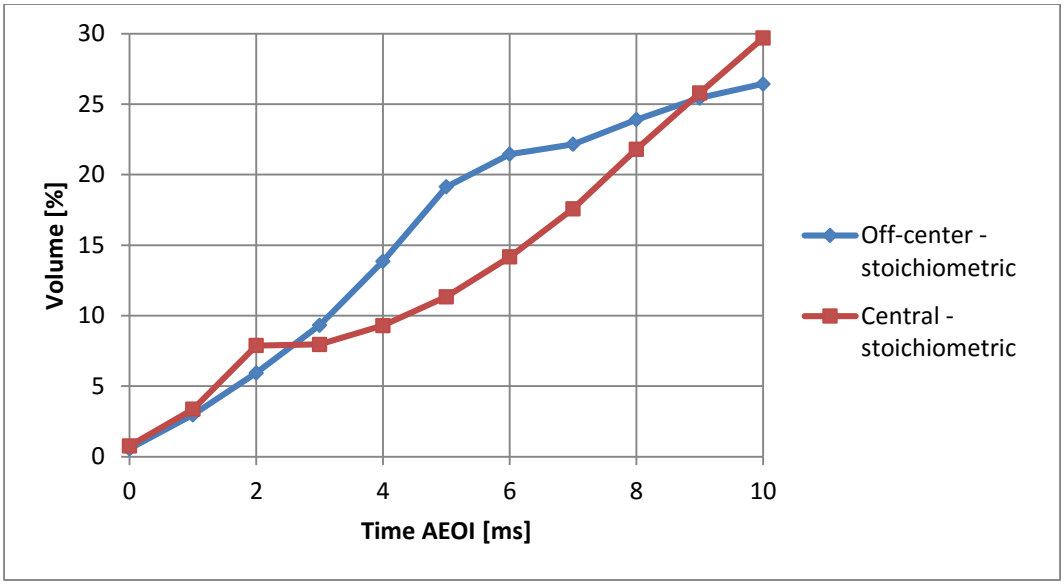

Figure 5.17: Volume in stoichiometric condition with respect to time AEOI. Central and off-center injector cases with the initial turbulent kinetic energy of the chamber equal to 216 m2/s2

In this final case, with a higher initial turbulent kinetic energy, the comparison is a bit more challenging than before. Even if the overall trend is the same of the previous case, if the mixing time is longer than 9 ms, the central injector is creating a bigger stoichiometric mixture. This happens because, if the chamber is turbulent, the off-center injector is behaving worse at the end of the process. The reason has already been explained before.

It must be kept in mind that the geometry of this model is much simpler than a real engine combustion chamber. Just thinking to the size and to the movement of a real piston, the differences are enormous.

Even though, just to have an idea of the order of magnitude of the time available to create the mixture, an example can be done.

With an engine running at 3000 or 4000 RPM, depending on the strategy adopted, the portion of crank angle available to create the mixture is generally longer than 150 CA deg. This interval is covered in 8 ms or 6 ms, respectively. When the engine runs slower, the time available to cover the same crank angle portion is longer but, in some cases, to increase the volumetric efficiency, the injection is delayed and so the mixing time can be again in this interval. In conclusion, since the time available to create a mixture is

between 5 ms and 8 ms, with both injectors the mixture is completely flammable but, with an off-center injector, the amount of volume in stoichiometric condition is bigger.
According to this consideration, the off-center injector behaves again better than the central one. It is important to underline that the extension of this consideration to an engine case could be not valid due to the simplicity of the geometry used in this work.

In conclusion, some considerations can be drawn from the results presented in the chapter. In order for the considered chamber to become homogeneous, so with a good stoichiometric mixture, at least 30 ms are necessary in the best condition. With an engine running at 3000 RPM, this time is covered in 540 CA deg. The aforementioned interval corresponds to one and half revolutions, so three quarter of a complete thermodynamic cycle.
With a port fuel injection, this value is acceptable because the injection and the mixing can start even before the intake valves opening. With a direct injection engine, it is necessary to complete the injection and the mixing in less than 360 CA deg. For this reason, 540 CA deg is way too long with respect to an acceptable crank angle interval. However, in these considerations, it must be remembered the limits related to the geometry used: it is very different with respect to a real engine.
It must be also considered that, in a real engine, the movement of the piston and the velocity of the air entering through the intake valves help to create a better mixture. The assumptions taken in this work, considering the zero mean velocity of the flow, the turbulent kinetic energy, the turbulence length scale (and as a consequence the dissipation rate), simplify even more the model. On the other side, a normal chamber is generally eighteen times larger than the chamber used and so, most likely, the time to create the mixture is even longer.

In conclusion, it can be asserted that the results obtained confirm the difficulties of creating a good mixture using CNG.

6. CONCLUSIONS AND RECOMMENDATIONS

In this project a 3D CFD model of an injector for a DI CNG engine was developed. The aforementioned model was validated thanks to the experimental data obtained by FCA using the DI CNG injector. The geometry of the nozzle used was the same as the real one and it was provided again by FCA. To develop the CFD model, parameters such as mesh topology and boundary conditions were analyzed. The effect of these parameters on the jet characteristics was also considered.

The first simulations were carried out using an instantaneous opening of the injector. This was done to tune the inlet pressure in such a way to obtain a mass flow rate in the simulation that was identical to the tested mass flow rate. However, to also obtain a good match of the tip penetration in the chamber, it was necessary to simulate the pintle opening. The results obtained for the penetration in the simulation had good correlation with the tested data.

The shape of the flow in steady state conditions was also analyzed. This comparison was done using the data obtained with an X-ray radiography technique. It was able to measure the amount of argon in the chamber and provide the results in the form of a path length. At the beginning, a study of how to obtain a path length from a 3D simulation was performed. A procedure was found using the software Ensight: it is described at the end of Chapter 3. The computed path length was compared to the tested values for two separate cases. The first was done with an open chamber, while in the second case, a wall was positioned 19 mm far from the injector to simulate the impact of the flow against a barrier. At the end, the matching of the path length was quite good in almost all the conditions and for this reason the model was considered as validated.

Using the obtained model, the effect of the rail pressure and the chamber pressure on the path length was analyzed to see how the flow shape changes with respect to these parameters. With this study, interesting results were obtained. When both the rail pressure and chamber pressure are higher, it was noticed that after 14 mm of flow travel,

the jet width increases considerably. Just downstream of the nozzle, in the 14 mm gap, the width of the flow stays constant, despite the increase of gas present.

The last part of the project was related to the study of the mixture formation with a small constant volume chamber. In particular, a precise analysis of the effect of some parameters, such as the turbulence in the chamber, was performed. The unique element of this project, with respect to what was found in literature, is the analysis of the injector position effect on the mixture formation. In conclusion, it was observed that:

- With a gaseous fuel like methane or CNG, the turbulence has a limited effect on the mixture formation. This is in-line with what was observed in literature.

- The time necessary to ensure the mixture is completely flammable was quite short. In the best case, 4 ms was enough to have a sufficient mixture; in the worst case 7 ms was required. These values cannot be really compared to a real engine due to the big differences in geometry. However, to gain a better understanding, for an engine running at 3000 RPM the 4 ms and 7 ms time intervals would result in a period equivalent to 90 CA deg. and 126 CA deg., respectively. These values are more than acceptable for an engine, unless it is running in stratified conditions.

- The position of the injector with respect to the side walls was affecting the mixing duration. If the flow in the chamber is static during the entire mixing process, the off-center injector results in a better mixture with respect to the central one, especially when considering the volume under stoichiometric conditions. When an initial turbulence is imposed in the chamber the gap between the off-center injector and the central injector decreases. If the time available to mix the methane and air is very long (at least 9 ms), the central injector provides a better mixture. If the time available is between 5 ms and 8 ms, then the off-center injector is better.

The analysis of the mixture formation was a good starting point to understand the most important concepts related to this issue. The biggest limit of this analysis was related to the geometry of the chamber used. Since it is so different from a real

combustion chamber, it does not allow doing a good correlation with a real-life case. The logical next step could be the application of the injector model to the geometry of a real engine. The results obtained with a real engine can give a much better estimation of the mixing property of methane or CNG. The same consideration is valid for the comparison of a central injection with a lateral injector.

Looking at the injector model, the first point that could be improved is the mass flow rate. The error obtained in steady state conditions was dependent on the mesh size. The model was considered acceptable for now as a finer mesh would result in increased computation time. This error due to mesh size was greater during the transient period of the simulation. To reduce this error in the transient period, a much finer mesh would be required in the injector region, applied in such a way to reduce the minimum lift. This will naturally again increase the computation time. Since the pintle opening duration is very short, the over-estimation of the amount of fuel injected does not contribute greatly to the error, and therefore can be considered as acceptable.

Validation of the simulation can be further improved. The data provided was based on a single rail and chamber pressure. The influence of pressure changes on the parameters such mass flow rate, penetration, and path length was studied in this project with the simulation, but could not be validated with experimental data. This type of comparison may prove interesting to understand the accuracy of the model under real operating conditions.

REFERENCES

[1] B. Leard and V. McConnell, "New Markets for Pollution and Energy Efficiency," *Resources for the Future,* vol. 1, pp. 1 - 37, 2015.

[2] M. Baratta, A. E. Catania and F. C. Pesce, "Multidimensional modelling of natural gas jet and mixture formation in direct injection spark ignition engines - development and validation of a virtual injector model," *Journal of Fluids Engineering,* vol. 133, pp. 1 - 14, 2011.

[3] A. Hajialimohammadi, A. Abdullah, M. AghaMirsalim and I. Chitsaz, "Experimental and numerical investigation on the macroscopic characteristics of the jet discharging from gaseous direct injector," *Journal of Mechanical Science and Technology,* vol. 28, pp. 773 - 781, 2014.

[4] H. L. Husted, G. Karl, S. Schilling and C. Weber, "Direct injection of CNG for driving performance with low CO2," *Aachen Colloquium Automobile and Engine Technology,* vol. 23, pp. 1 - 22, 2014.

[5] "Chemical Composition of Natural Gas," Union Gas - A Spectra Energy, 2015. [Online]. Available: https://www.uniongas.com/about-us/about-natural-gas/Chemical-Composition-of-Natural-Gas. [Accessed 10 05 2015].

[6] M. Baratta and N. Rapetto, "Fluid-dynamic and numerical aspects in the simulation of direct CNG injection in spark-ignition engines," *Computers and Fluids,* vol. 103, pp. 215 - 233, 2014.

[7] A. N. Laboratory, "The Greenhouse Gases, Regulated Emissions, and Energy Use In Transportation Model," GREET 1.8d.1, 26 August 2010. [Online]. Available: https://greet.es.anl.gov/. [Accessed 20 06 2015].

[8] "Periodic Table," Royal Society of Chemistry, [Online]. Available: http://www.rsc.org/periodic-table/element/18/argon. [Accessed 19 04 2015].

[9] O. Singh, Applied Thermodynamics, Kanpur, India: New Age International Publishers, 2009.

[10] H. Schlichting, Boundary Layer Theory, New York: McGraw-Hill Inc., 1968.

[11] "Honda Finally Adds Direct Injection to Its V6 and Four-Cylinder Engines," Car and Driver, 29 11 2011. [Online]. Available: http://blog.caranddriver.com/honda-finally-adds-direct-injection-to-its-v6-and-four-cylinder-engines/. [Accessed 28 05 2015].

[12] M. Arai, K. Amagai and T. Ebara, "Attitude control of a diesel spray under the Coanda effect," *SAE Technical Paper,* vol. 1, pp. 1 - 10, 1994.

[13] W. H. Kurniawan, S. Abdullah, K. Sopian, Z. M. Nopiah and A. Shamsudeen, "CFD investigation of fluid flow and turbulence field characteristics in a four-stroke," *The Institution of Engineers,* vol. 69, no. 1, pp. 1 - 12, 2007.

[14] "The Egineering ToolBox," [Online]. Available: http://www.engineeringtoolbox.com/specific-heat-capacity-gases-d_159.html. [Accessed 02 04 2015].

[15] C. Powell, R. Scarcelli and T. Wallner, "Efficiency-Optimized Dual Fuel Engine with In-Cylinder Gasoline/CNG Blending," Argonne National Laboratory, February 16, 2015.

[16] S. W. Lee, D.-S. Baik, T. Rogers and T. Peterson, "Characteristics of CNG fuel engine," *Advanced Science and Technology Letters,* vol. 33, pp. 29 - 32, 2013.

[17] A. Atthasit, "Slideshare," 2010. [Online]. Available: http://www.slideshare.net/AnurakAtthasit/aircraft-propulsion-fuel-injection. [Accessed 10 06 2015].

[18] C. Xia, The Behaviour of a Gaseous Transient Jet in a Direct Injection Turbulence Chamber, University of Windsor: PhD Thesis, 2006.

[19] M. Baratta, N. Rapetto and E. Spessa, "Numerical and experimental analysis of mixture formation and performance in direct injection CNG engine," *SAE International,* pp. 1 - 22, 2012.

[20] R. M. Barron, "Introduction to CFD," in *Lecture Notes for Mechanical Engineering*, Windsor, Canada, University of Windsor, 2014.

[21] A. Bakker, "Applied Computational Fluid Dynamics," in *Solution Methods - Lecture 5*, Fluent Inc., 2002.

[22] J. Peiro and S. Sherwin, "Finit Difference, Finite Element and Finite Volume Methods for Partial Differential Equations," in *Handbook of Materials Modeling*, Imperial College, London, UK, Springer, 2005, pp. 1 - 35.

[23] M. Hubbard, Finite Volume Schemes: A Tutorial, University of Leeds, UK.

[24] K. J. Richards, P. K. Senecal and E. Pomraning, *Converge 1.4.1 - User Guide and Reference,* Middleton, WI: Convergent Science Inc., 2012.

[25] G.-H. Kim, A. Kirkpatrick and C. Mitchell, "Computational modeling of natural gas injection in a large bore engine," *Journal of Fluids Engineering,* vol. 126, 2004.

[26] Z. Han and R. Reitz, "Turbulence modeling for internal combustion engine using RNG k-ε models," *Combustion Science and Technology,* vol. 106, pp. 267 - 295, 1995.

[27] C. Powell and G. Singh, Fuel injection and spray research using X-Ray diagnostics, Crystal City, VA: Argonne National Laboratory, 2012.

[28] J. Geiswillery, E. Robertz, L. Huré, C. Cachoncinlle, R. Viladrosa and J. M. Pouvesle, "Flash x-ray radiography of argon jets," *Meas. Sci. Technol.,* pp. 1537 - 1542, 16 June 1998.

[29] A. Suryanarayana, Mass Transfer Operations, New Delhi: New age international publishers, 2002.

[30] H. F. Coward and G. W. Jones, *Limits of flammability of gases and vapors,* Washington DC: US Government printing office, 1952.

[31] P. G. Tucker and Z. Pan, "A Cartesian cut cell method for incompressible viscous flow," *Applied Mathematical Modelling,* vol. 24, pp. 591 - 606, 2000.

[32] S.-I. Sohn and J. Y. Shin, "A second order upwind method for linear hyperbolic systems," *Commun. Korean Math. Soc. 17,* pp. 103 - 120, 2002.

[33] J.-H. Kim, H.-D. Kim, S. Matsuo and T. Setoguchi, "Study for the Gas Flow through a Critical Nozzle," *J. of Thermal Science,* vol. 12, 2003.

[34] Y. Liu, J. Yeom and S. Chung, "A study of spray development and combustion propagation processes of spark-ignited direct injection (SIDI) compressed natural gas (CNG)," *Elsevier Journal / Mathematical and Computer Modelling,* vol. 57, pp. 228 - 244, 2013.

[35] S. S. Thipse, S. B. Sonawane, A. F. D. Souza, S. D. Rairikar, K. K. Kavathekar and N. V. Marathe, "Injection strategies, optimization and simulation techniques," *SAE International,* vol. 26, pp. 1 - 12, 2015.

[36] Y. Ali, A. Shamsudeen, S. Abdullah and W. M. F. Wan Mahmood, "Development of CNG direct injection (CNGDI) clean fuel," *The 4th International Meeting of Advances in Thermofluids,* pp. 541 - 550, 2012.

[37] T. J. Craft, L. J. W. Graham and B. E. Launder, "Impinging jet studies for turubulence model assessment - II. An examination of the performance of four turbulence model," *Heat Mass Transfer,* vol. 36, pp. 2685 - 2697, 1993.

[38] J. M. Meyers, "ME 239: Rocket Propulsion," in *Nozzle Thermodynamics and Isentropic Flow Relations*, Burlington, University of Vermont.

[39] R. Scarcelli, W. Thomas , M. Nicholas, V. Salazar and S. Kaiser, "Mixture formation in direct injection hydrogen engines: CFD and optical analysis of single- and multi-hole nozzles," *SAE International,* pp. 1 - 15, 2011.

[40] X. S. Zeng, *Modeling Injection and Ignition in Direct Injection Engines,* Toronto: Phd Thesis - University of Toronto, 2008.

[41] R. Scarcelli, "Challenges and Opportunities for the Use of Natural Gas in the Light-Duty Automotive Field," in *Natural Gas as a Transportation Fuel: A Panel Discussion*, 2012.

[42] M. B. Çelik and B. Özdalyan, *Gasoline direct injection,* Karabuk: Intech Open, 2010.

[43] A. L. Martelli and P. T. Lacava, *Injection Timing Evalutaion of a Compressed Natural Gas Direct Injection Engine,* Divisão de Engenharia Aeronáutica, Instituto Tecnológico de Aeronáutica, 2010.

[44] H. Babazadeh, D. S. Nobes and K. Charles Robert, "Active and passive flow control on a precessing jet," *Experiments in Fluids,* vol. 56, no. 1, pp. 1 - 10, 2015.

[45] E. Sonnendrucker, Numerical methods for hyperbolic systems, Munchen: Max-Planck-Institut fur Plasmaphysik, 2013.

VITA AUCTORIS

NAME:	Biagio Logaldo
PLACE OF BIRTH:	Maratea, PZ, Italy
YEAR OF BIRTH:	1991
EDUCATION:	Liceo Scientifico De Lorenzo, Lagonegro, PZ, Italy, 2005 - 2010
	Politecnico di Torino, B.Sc., Torino, TO, Italy, 2010 - 2013
	Politecnico di Torino, M.Sc., Torino, TO, Italy, 2013 - 2015
	University of Windsor, M.Sc., Windsor, ON, Canada, 2014 - 2015